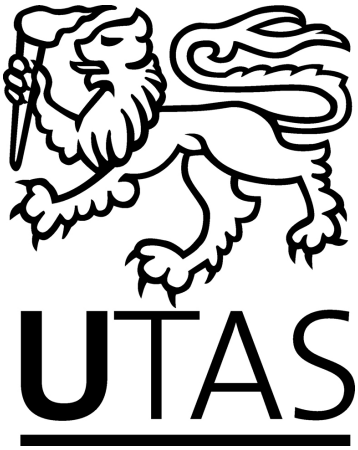

University of Tasmania
School of Mathematics and Physics

Southern Hemisphere Gamma-Ray Blazars

Jay M. Blanchard

October 2013

Supervisors:
Dr. Jim Lovell
Dr. Roopesh Ojha
Dr. Phil Edwards
Prof. John Dickey

Submitted in fulfilment of the requirements for the Degree of
Doctor of Philosophy

Declaration of Originality

This thesis contains no material which has been accepted for a degree or diploma by the University or any other institution, except by way of background information and duly acknowledged in the thesis, and to the best of my knowledge and belief no material previously published or written by another person except where due acknowledgement is made in the text of the thesis, nor does the thesis contain any material that infringes copyright.

Signed: 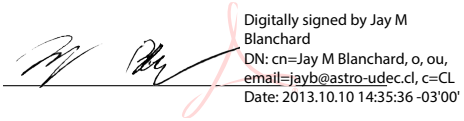

Date: 10/10/2013

Authority of Access

The publishers of the papers comprising Chapter 2 hold the copyright for that content, and access to the material should be sought from the respective journals. The remaining non published content of the thesis may be made available for loan and limited copying and communication in accordance with the Copyright Act 1968.

Signed: 

Date: 10/10/2013

Statement of Co-Authorship

The following people contributed to the publication of work undertaken as part of this thesis:

Chapter 2: *High resolution rapid response observations of compact radio sources with the Ceduna Hobart Interferometer (CHI)*

Authors:
Candidate: **Blanchard, J.M.,** *School of Maths and Physics, University of Tasmania*
Author 1: **Lovell, J.E.J.,** *University of Tasmania*
Author 2: **Ojha, R.,** *NASA, Goddard Space Flight Center*
Author 3: **Kadler, M.,** *Universität Würzburg*
Author 4: **Dickey, J.M.,** *University of Tasmania*
Author 5: **Edwards, P.G.,** *CSIRO Astronomy and Space Science*

Candidate was the primary author and with Author 1 and Author 2 contributed to the idea, its formalisation, development and refinement. Writing was done primarily by the Candidate, with some paragraphs by Author 2. Author 3 contributed to the idea and provided feedback. Author 4 and Author 5 provided feedback.

Candidate (75%), Author 1 (10%), Author 2 (10%), Remaining Co-Authors (5%).

Signed: _____ _____

Dr. Jim Lovell
Supervisor
School of Maths and Physics
University of Tasmania

Prof. John Dickey
Head of School
School of Maths and Physics
University of Tasmania

Date: _____

Abstract

The detection of high energy gamma-ray emission from AGN has resulted in several emission mechanisms and emission sites being proposed. One such emission mechanism relies on the inverse Compton effect. In this effect low energy photons are upscattered to high energies due to collisions with high energy electrons. This would suggest a possible link between radio synchrotron emission (providing high energy electrons) and the observed gamma-ray emission. Previous work in the field has suggested such a link, however the details of the interaction are not fully understood. Statistical studies on a sample of AGN have shown a delay due to optical depth effects of the order of 1.2 months in the source frame, with the gamma-ray emission leading. In this thesis studies of individual sources are presented, for which flaring events have been observed, and it is found that while optical depth can explain the time lag between flaring at different frequencies in some cases, it can not be the sole mechanism causing such a delay. Different emission sites for the radio and gamma-ray flares are proposed, to account for the properties observed. A new instrument, the single baseline interferometer CHI which can be used to quickly ascertain the compact radio flux of a gamma-ray flaring AGN is also introduced.

Acknowledgements

This thesis would not have been possible without the following people. You are all awesome! I'm sure I've forgotten people so many many thanks to the lot of you!

Firstly my supervisors: **Jim Lovell** Thank you so much for taking me on as a student, figuring out where this project would end up with me, and getting corrections to me in record time! Also for putting up with me breaking your telescopes all the time... **Roopesh Ojha**, many thanks are also due for all the help you have given me, pulling me into TANAMI, late night skype chats from the other side of the world, showing me around Greenbelt, getting me to go to Germany for 5 months and everything else. **Phil Edwards**, thanks for all the times you've sent me interesting papers to read, the discussions about everything radio, always clearing a space on your desk for me when I come to visit ATNF and information dump at you and more. **John Dickey**, for always having an open door and discussing problems. You have all been amazing and I couldn't have done this without you!

I also need to thank **Joern Wilms**, **Matthias Kadler** and the rest of the Bamburg, Erlangen, and Wuerzburg crew for giving me the chance to come work in Germany for 5 months. I had a great time and learnt a lot!

Thanks are also due **Justin Finke** and **Mike Dutka** for all their help on SED modelling and gamma-ray reduction respectively. Mike, thanks also for driving me around Greenbelt and all your patient explanations of gamma-ray reduction, SWIFT stuff and so on!

Karen Bradford, you are a logistical marvel and always helpful and fun to chat to. This thesis would not exist without your help!

Stas Shabala and **Jamie McCallum** My thanks go out to you two for always being around to help troubleshoot telescopes, answer random questions, and speculate about the weird flare seen in source x.

My officemate **Anita Titmarsh**, thanks for decorating my office in thesis finishing colours! Then there's putting up with me for... 8 and a bit years. Also to **Chris Jordan** for being my replacement... and being a great housemate the last few weeks of my thesis writing.

To the little PhD crowd next door **Vasaant, Dave, Courtney and Paul** (in room order) for the many discussions about stuff, and major board staring sessions.

To all my friends, who've been supportive of me during the thesising, many thanks go out to you all.

Minnie Mao, for being an amazing housemate and friend and for sharing Tassie with me. I had an awesome time exploring with you! There's still so much to see...

Lastly I have to thank my family, Mum, Dad, Sis, I love you all. Thanks for all the support you've given me throughout my studies, and sorry for the times I was grumpy at you.

Contents

Chapter 1

AGN - A Review

1.1 Discovery

Radio astronomy began as a study of static affecting trans-Atlantic radio communications. Jansky (1932) used a rotatable antenna operating at a wavelength of 14.6 m to identify the direction of incoming static. He discovered three main sources, local thunderstoms, distant thunderstorms and a steady hiss which he could not initially locate. He then discovered the location of the maxima of the emission changed gradually over the course of a year and concluded an extraterrestrial origin of the Milky Way (Jansky 1933).

His work was expanded on by Grote Reber, who built a 9.5 m (31 foot) radio dish, steerable on the north-south axis to Declinations between -32.5 and 90 degrees, using the Earth's rotation and a chart recorder to measure the intensity of 'cosmic static' in a band of sky at a set Declination (Reber 1944). Reber detected emission from the Sun, the center of the Milky Way (Sagittarius), as well as several local maxima, including one in the constellation of Cygnus (Reber 1944). This was the first detection of an extragalactic radio source, Cygnus A, although the extragalactic nature of source would not become apparent until much later.

In 1953, the position of the radio source Cygnus A was measured with the unprecedented accuracy of 1 arcminute in Right Ascension and 40 arcminutes in Declination using the Cambridge interferometer, consisting of two 3.7 m and two 1.4 m dishes (Smith 1951). This was accurate enough to identify an optical counterpart from a Palomar 200-inch plate (Baade and Minkowski 1954). They correctly associated the radio source with an 'extragalactic nebula' in Cygnus (which had no optical name at the time), which they deduced to be two galaxies in collision, and calculated the total energy emitted to be 5.6×10^{42} ergs s^{-1}, proposing that the source of the radio energy may be the kinetic energy of the colliding 'nebulae'. This was followed by the association of 3C295 to a distant cluster of galaxies by Minkowski (1960), as well as the cross identification of 3C48 to a magnitude 16 'star' in 1960 (Bolton 1990). Bolton and his colleagues had obtained a spectrum for 3C48 and fitted a broad line and a forbidden transition with a redshift of ~ 0.37 in 1957. However, due to a three angstrom uncertainty in the rest wavelength fit they did not publish their conclusions

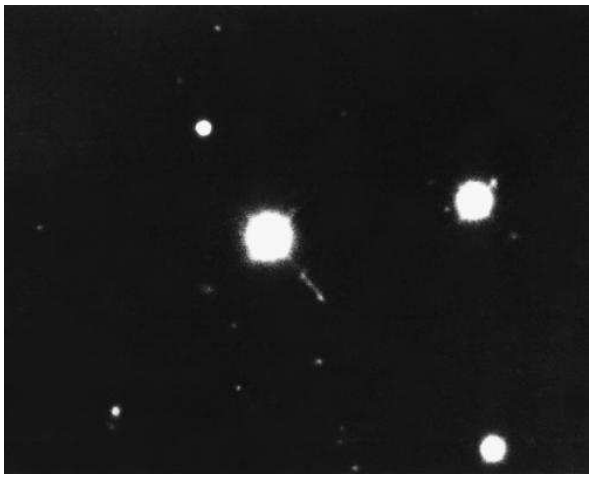

Figure 1.1 Optical image of 3C273 and its jet, associated by Hazard et al. (1963) to the quasar. Image credit: AURO/NOAO/NSF. Taken with the 4 metre telescope at the Kitt Peak National Observatory.

until three years later (Greenstein 1963).

Hazard et al. (1963) used the Parkes Radio Telescope to accurately measure the position of 3C273 during an occultation by the moon in 1962. This position was then used by Maarten Schmidt and Bev Oke to identify an optical counterpart (Schmidt 1963) finding a blue star and a 'faint wisp, or jet' (Figure 1.1). Spectral studies of the 'star' however revealed broad emission lines consistent with known transitions at a redshift of ~ 0.158, placing it well outside the galaxy.

The 'star-like' appearance of these objects lead to their names, Quasi-Stellar Objects (QSOs) and Quasi-Stellar radio sources (quasars) for the radio quiet and radio loud sources respectively. These names are now often used interchangeably.

1.2 Optical Spectra

As mentioned above, it was spectral observations at optical wavelengths that provided the first important clues towards the nature of these sources. Quasars in general show very bright emission features and a low intensity continuum (Figure 1.2). When initially observed, these lines did not match any known at the time, causing confusion. Initial claims of a possible high redshift explanation were not generally accepted. Some of the lines observed had only previously been seen in hot nebulae, which would be too diffuse to generate the required power observed from these objects (Greenstein and Schmidt 1964).

Another major problem at the time was that no known emission mechanism could account for the energies required, assuming the redshift observed was due to cosmological distance. One alternate theory was that these objects had been ejected at high speeds from nearby galaxies (Arp 1987), however this had problems of its own, for example, no blue-shifted

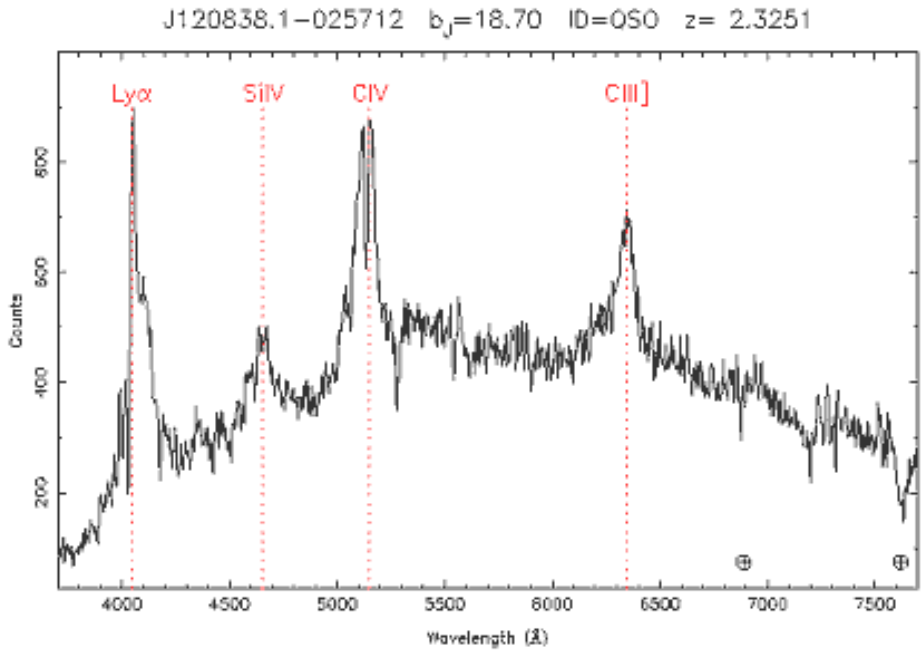

Figure 1.2 A typical quasar optical spectrum showing several bright emission lines consistent with a redshift of 2.3251. Note the approximately factor of four increase in intensity of the emission lines above the continuum. Credit 2dF survey (Colless et al. 2001).

quasars were found.

Furthermore, some of the emission lines seen in quasars are fairly broad, indicating a high velocity dispersion of the emitting gas. Along with these, narrow forbidden lines were also observed, suggesting a complex source structure. Narrow forbidden lines require low velocity low density material and thus a large emitting region whereas broad lines require a high velocity small emitting region.

1.3 AGN and Seyferts

Seyfert galaxies had been discovered prior to quasars and share many of their features, including broad emission lines, some narrow lines and a very bright core. Around 7% of Seyfert galaxies are radio loud compared to 12% of quasars (Komossa et al. 2006). They were discovered before quasars as they are local galaxies, close enough for the optical galaxy to be resolved.

Seyfert galaxies were initially split into two types, depending on the presence of both narrow and broad lines (Type 1), or only narrow lines (Type 2). It is now believed that they are likely to be the same object, with the broad line regions obscured depending on the orientation of the galaxy along the line of sight (see Figure 1.3). As in quasars, the majority of the emission from Seyferts is generated in the small inner core, called an Active Galactic Nucleus (AGN). Seyferts are now thought to be the low luminosity, local equivalent

to quasars.

1.4 Blazars

Blazars are a subset of quasars that are radio-loud with some particular characteristics. Rapid variability is a main feature of these objects, occurring on all timescales and at all frequencies. The optical and radio emissions are also often highly polarised, and in some cases there is a distinct lack of spectral features normally expected from quasars. Blazars are further split into several sub groups, as described below.

1.4.1 BL Lacertae Objects

The original BL Lac object, BL Lacertae, was discovered by Hoffmeister (1929) and was initially mis-identified as a highly variable star. It was later found to have associated radio emission, that was also highly variable in nature (Schmitt 1968). BL Lac objects are mostly devoid of the usual quasar emission lines, making redshift measurements difficult. They are thought to be oriented in such a way that the relativistic jet lies nearly along the line of sight. The synchrotron emission from the jet is Doppler boosted to such a high intensity that it swamps the emission features (and continuum emission) normally observed. The continuum spectra of BL Lac objects usually extend far into the X-ray band, and often all the way into gamma-rays. Variability at gamma-ray wavelengths has been observed on timescales of less than a day (Buckley et al. 1996) and so, if the assumption regarding the orientation of these objects is correct, and they are indeed in other respects very similar to other quasars, the variability can be used to limit the size of the emission region. As any changes in intensity must occur roughly within the time taken to cross the emission region the size of the core can be constrained to $\lesssim$ 1pc, see also Kataoka et al. (2001) for a full explanation.

1.4.2 Other Types

Flat-Spectrum Radio Quasars (FSRQs) may well be referred to as the 'standard type' of blazar, being radio loud with a core dominated flat radio spectrum and optical emission lines. Other types of blazars share many similarities with BL Lac objects and include Optically Violent Variables (OVVs) and High Polarisation Quasars (HPQs).

1.4.3 Blazar features

The optical emission seen originating from blazars differs from that in most quasars. It is highly polarised, the percentage of polarisation can be of order 20% as compared to 2-3% for quasars (Visvanathan and Wills 1998), and is not well modelled by a blackbody disk model. Instead the emission often forms a curve that can be fit by a synchrotron model all the way from radio through to X-ray (Landt et al. 2008). This is consistent with the observed polarisation levels as synchrotron radiation is often associated with highly polarised emission.

These observations fit well with the idea of a jet lying close to the line of sight of the observer, as the Doppler beamed synchrotron emission would be likely to dominate. It is interesting that a large amount of blazars also emit gamma rays (Nolan et al. 2012), this emission is likely from the inverse Compton effect, and possibly Self-Comptonisation (explanation follows). In this case, if the gamma-rays are produced internal to the jet, the amount of gamma-ray radiation would depend on the orientation of the jet with respect to the line of sight and thus would be expected to vary with blazar type. In such a case the radio emission (from synchrotron) and the gamma-ray emission (indirectly related to the synchrotron) would be linked.

1.5 Unified Model

Seyferts, Quasars, Blazars and BL Lac objects all seem to be very closely related, and are in fact likely to be variations of the same thing. A model has hence been proposed detailing the components required to unify these different phenomena (Urry and Padovani 1995). Quasars have been discovered at very high redshifts (Ghisellini et al. 2011) and so their intrinsic luminosities must also be very high (up to 10^4 times that of an average galaxy!). Yet, based on the variability of the sources (particularly BL Lac objects) all the energy required to produce such high luminosities must be generated within a region not much larger than a parsec. Quasars often (but notably not always) show strong emission features which are likely to be dependent on orientation.

The unified model has several major features (Figure 1.3):

1.5.1 Black Hole

A central supermassive black hole is needed to fuel the AGN. There is as yet simply no alternate mechanism for producing radiation at the energies observed from these objects (assuming they are indeed at the distances their redshifts suggest). The black hole has been shown in some cases to have a mass greater than 10^9 solar masses (Gebhardt and Thomas 2009). It has been suggested that all galaxies likely possess a black hole in their core, whether they have an AGN or not (Urry and Padovani 1995). Alternate evidence for the existence of black holes also exists. Research into the orbit of stars around the cores of our own galaxy and those close to us suggest the presence of a gravity well requiring a black hole (Eckart and Genzel 1997; Ghez et al. 2000). Studies of watermasers in NGC4258 (M106) (Miyoshi et al. 1995; Argon et al. 2007) found a body of gas rotating near the centre of the galaxy. This gas has a volume averaged density 40 times greater than that of any previously proposed black hole candidate. Assuming a rotational velocity of the gas due solely to the gravitational effect of a central body, this rotation implies an object with 3.6×10^7 solar masses within a region of radius less than 0.13 pc. More recent work by Humphrey et al. (2008), used the Chandra X-ray telescope to study the temperature of the interstellar medium in the giant

elliptical galaxy NGC 4069. They found a temperature peak within the central 200 pc and demonstrated that this requires a black hole of mass $3.35^{+0.67}_{-0.95} \times 10^9$ solar masses.

1.5.2 Accretion Disk

An accretion disk explains many of the features observed in these objects, in particular it is the origin of the thermal emission. Modelling of infalling matter into a black hole also suggests the likely formation of a disk, and such a disk is required in jet formation theory. As angular momentum must be conserved for the accretion disk as a whole and matter infalling towards the black hole loses angular momentum there must be some mechanism for its transfer from matter spiralling inward to matter further out. Shakura and Sunyaev (1973) proposed a model in which turbulence enhanced viscosity provides this momentum transfer. More recent work (Balbus and Hawley 1991) shows an instability to axisymmetric disturbances in the presence of magnetic fields embedded in these disks, which would also explain the momentum transfer required. The turbulance and change in gravitational potential energy of infalling material is enough to heat the disk such that it can emit thermal radiation with energies all the way up to the X-ray part of the spectrum.

1.5.3 A Broad Line Region (BLR)

Reverbration mapping studies (Wanders et al. 1997) suggest the broad line region extends several hundred light days from the core of the quasar. These studies exploit the nature of the absorption/emission mechanism of gas to determine the location of a BLR. By monitoring the UV and optical emission lines, and the source intensity with high time resolution, it is possible to identify the site and geometry of the BLR. Consider a source brightening instantaneously. This is immediately observed in total intensity measurements of the source. The emission line strength will only increase after a time delay τ, due to the distance of the absorbing (and then reemitting) BLR. See Peterson (1993) for an in depth review. This region must contain high velocity gas producing the Doppler broadened emission lines seen in many quasars.

1.5.4 A Narrow Line Region (NLR)

The narrow line region is suspected to lie much further out than the BLR (see Figure 1.3), and may be associated with the host galaxy itself.

In order to explain the difference between Type 1 and Type 2 Seyferts the presence of a 'dusty torus' surrounding the BLR is inferred. This torus, when combined with orientation effects, blocks the BLR in Type 2 Seyferts. There is some independent evidence for this (Antonucci 1993), consisting of excess dust emission in Type 2 Seyferts.

1.5.5 A Jet

Jets have been observed in some quasars, and are frequently associated with blazars and Seyferts. These jets have been observed from radio all the way through to X-ray frequencies, and are thought to emerge perpendicular to the accretion disk, before stretching out into radio lobes. Jets explain the variability observed in BL Lac objects and blazars, and are required by the unified model to explain the difference between some quasar types (as well as to quench the strong spectral features usually seen in quasars). See Urry and Padovani (1995) for more information.

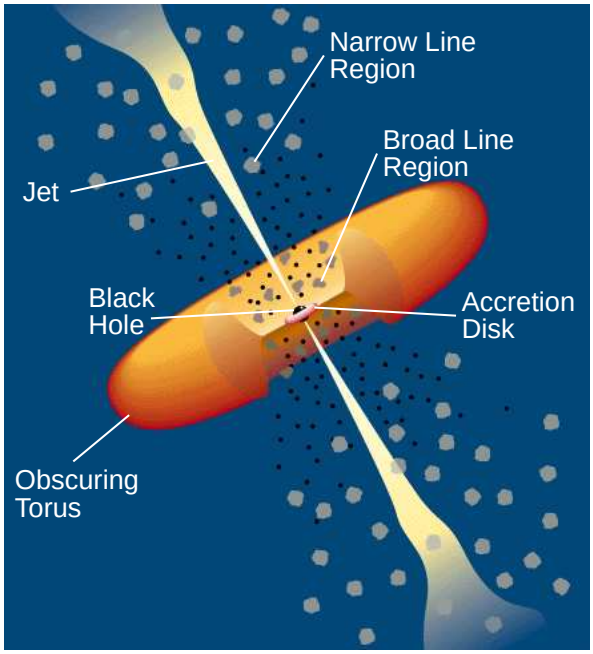

Figure 1.3 The unified model. The type of source, and spectral features observed depends on the line of view of the observer. An observer looking straight down the jet will identify a blazar, whereas an observer seeing the AGN side on will identify a more standard radio galaxy. Image credit Urry and Padovani (1995).

1.6 Spectral Energy Distribution

The radiation being emitted from quasars has been observed from radio wavelengths all the way to TeV Gamma-Rays (e.g. Figure 1.4), and usually peaks in the UV part of the spectrum. The UV peak is due to thermal emission from the accretion disk surrounding the black hole. This explains the general blue colour of 3C273 and other early detections. Quasars are on average bluer than stars and this was utilised as an identification criterion, leading to several large, optically selected surveys including the Palomar Bright Quasar Sample (Schmidt and Green 1983) and the Bright Quasar Survey (Hewett et al. 1995). These surveys used the blue dominance and the characteristically strong emission lines of quasars for identification

and as such were insensitive to BL Lac objects, which are often red with featureless optical spectra (Miller et al. 1978). AGN are typically separated into two groups, radio-loud and radio-quiet, based on the relative intensity of the radio part of their broadband emission (Figure 1.4 illustrates this). Physically the difference lies in the presence of a strong (often kpc scale) collimated jet for radio-loud sources or the lack, or small, faint, parsec scale nature, of the jet in the radio-quiet case.

1.7 Emission Mechanisms

The energies required to account for the radiation observed from quasars necessitated new emission models. It was only with the advent of accretion disk models in the 1970s that emission mechanisms consistent with the proposed redshifts of quasars could be considered (Shakura and Sunyaev 1973). The basic idea is summarised here, for a full review see Abramowicz and Fragile (2013). At the core of the host galaxy is the AGN, consisting of a supermassive black hole, that is accreting dust, gas, and the occasional star via an accretion disk. The black hole itself can be of the order of 10^9 solar masses (Rees 1984). The accretion disk is formed due to conservation of angular momentum as the in-falling matter spirals towards the black hole.

Due to friction, the disk of matter is heated to extremely high temperatures ($\sim 10^5$K Bonning et al. 2007), producing thermal emission which contributes to the continuum seen in the quasar spectrum (mostly in the infrared, optical, and UV). Even taking into account the large distances of quasars, the fact that the majority remain unresolved in optical telescopes indicates a small angular size, which constrains the physical size of the emitting region to a few kpc.

1.7.1 Radio

The majority of the radio emission seen from radio loud quasars is thought to emanate from a jet. Jets are mostly observed in the radio part of the spectrum (partly due to resolution effects), although some jets emit all the way from radio through to TeV Gamma-ray energies. The exact method of jet formation is still poorly understood. The generally held theory (Shields 1978) involves magnetic field lines embedded in the accretion disk. The magnetic fields are likely formed due to ionized particles from the accretion disk in-falling towards the black hole. The magnetic field lines form a helical spiral due to the rotation of the disk. Charged particles spiralling up the magnetic field lines hence emit synchrotron radiation, forming a jet perpendicular to the accretion disk.

Synchrotron Emission

The characteristic frequency of radiation emitted in cyclotron radiation (the non-relativistic case of synchrotron radiation) is the gyrofrequency. That is the frequency at which a charged

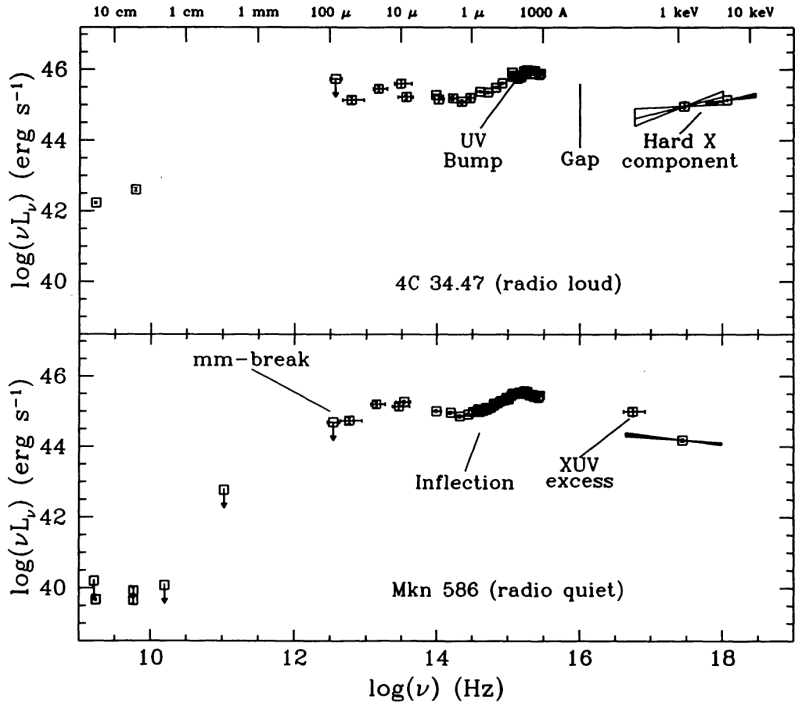

Figure 1.4 Quasar spectra for 4C 34.47 (top) and Mrk 586 (bottom). 4C 34.47 is radio loud, and Mrk 586 is radio quiet. Note the UV excess (Elvis et al. 1994).

particle rotates around the magnetic field direction. However when the particle attains relativistic velocities further effects have to be taken into account. Firstly, the emission becomes highly boosted along the direction of travel. As such the emission observed is dominated by pulses when the charged particle is travelling closest to the line of sight of the observer, affecting the characteristic frequency. Higher order harmonics also become more important due to Doppler Boosting.

Electrons of energy E moving in a magnetic field B at pitch angle θ will emit the majority of energy at characteristic frequency ν_c:

$$\nu_c \sim 0.016 B \sin(\theta) E^2 \tag{1.1}$$

Where v_c is in GHz, B is in micro G and E in GeV. Summing the contributions of each electron gives the standard power law spectrum observed from many AGN, $S_\nu \propto \nu^\alpha$ (where S_ν is the flux density at frequency ν). The extremely beamed nature of this emission for blazars causes the observed properties to vary greatly based purely on the geometry of the system.

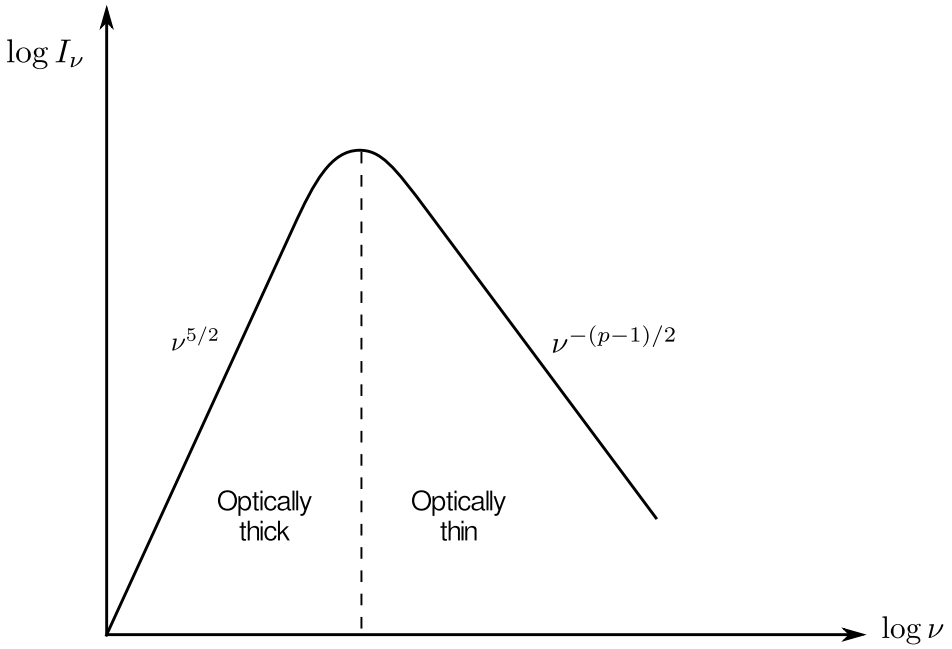

Figure 1.5 The spectrum produced by synchrotron emission and synchrotron self-absorption (Rybicki and Lightman 1979).

Synchrotron Self-Absorption

For sources with brightness temperature $T_B > m_e c^2/k \approx 10^{10} K$ synchrotron self-absorption will be evident in the observed spectrum. Synchrotron self-absorption is the process during which synchrotron electrons absorb (and then subsquently re-emit) the photons they are producing. For electrons with a power-law distribution the optically thick spectrum (the part at which self-absorption takes place) becomes $S_\nu \propto \nu^{5/2}$ (Rybicki and Lightman 1979). The resultant spectrum is shown in Figure 1.5.

Bremstrahlung and Free-Free Emission/Absorption

Bremstrahlung is a thermal process, that is it depends on the temperature of the medium. In an ionised plasma, charged particles can undergo collisions with atoms. In such a collision, the particle (usually an electron) can either be captured or decelerated by the collision, losing kinetic energy in the form of a photon with energy equal to the change in kinetic energy of the electron. If the electron is not captured in the process it is termed 'free-free emission'. An electron undergoing a collision can also gain energy by absorbing a photon. This is 'free-free absorption'. An electron will have kinetic energy $\frac{1}{2} m_e v^2$ which is approximately equal to kT. The length of interaction is proportional to $v^{-1} \propto T^{-1/2}$. Thus the absorption coefficient for an interaction is proportional to $Z^2 v^{-3}$ where Z is the charge number of the ion. If ρ is the density of particles then the number of interactions will be proportional to $\rho T^{-1/2}$. Thus the absorption coefficient will be:

$$\kappa \propto Z^2 \rho T^{-1/2} v^{-3} \tag{1.2}$$

Since $v \propto T$ and integrating over frequency gives Kramers' Opacity Law (Abhyankar 2002):

$$\kappa_{ff} \propto \rho T^{-7/2} \tag{1.3}$$

1.7.2 Inverse Compton Effect

The X-ray and gamma ray radiation observed from some quasars is likely produced via the inverse Compton effect. In this effect, a relatively low energy population of photons is boosted to higher energies via collisions with high energy electrons. For an isotropic distribution of photons, the power emitted is given by:

$$P_{comp} = \frac{4}{3} \sigma c U_{rad} \gamma^2 \beta^2 \tag{1.4}$$

where U_{rad} is the energy density of the photon field.

Comparing this with the power emitted by synchrotron emission:

$$P_{synch} = \frac{4}{3} \sigma c U_B \gamma^2 \beta^2 \tag{1.5}$$

where U_B is the energy density of the magnetic field, gives the ratio:

$$\frac{P_{comp}}{P_{synch}} = \frac{U_{rad}}{U_B} \tag{1.6}$$

So the relative emission due to synchrotron and Compton processses is only dependent on the magnetic field energy density and the photon field energy density (Peacock 1999).

Inverse Compton Limit

If the photons being upscattered are produced by synchrotron emission from the same electrons that are then causing the scattering, the process is termed Synchrotron Self Comptonisation. This self-Comptonisation produces photons, affecting the energy density U_{rad}. This results in 'cooling' of the relativistic electron population and, since the process is a strong function of the brightness temperature of the source, creates an upper limit of brightness temperature $T_B \sim 10^{12} K$. This is known as the 'Inverse Compton Limit' (Kellermann and Pauliny-Toth 1969). Further work on the matter by Readhead (1994) showed that the actual observed cutoff occurs much earlier, near the 'equipartition brightness temperature $T_B \sim 10^{11}$.

Source Populations

The origin of the photon and electron populations in a blazar is not yet fully clear. The low energy photon population could be produced internal to the jet (synchrotron self compton-isation) or externally (from the regions of gas producing the emission features, or from the thermal accretion disk). The high energy electron population is likely that produced by the jet, suggesting a possible link between radio and gamma ray radiation observed from these objects.

1.7.3 Superluminal Motion

Superluminal motion is an apparent transverse velocity of a jet component greater than the speed of light c. Superluminal motion arises due to a geometrical effect in which the jet from an AGN lies close to the line of sight. Consider a stationary component, the 'core' and a component moving outward along the jet at velocity v, see Figure 1.6 panel (a). In time τ the component has moved a distance $v\tau$, but appears to have moved a transverse distance $v\tau \sin(\theta)$. Due to the finite speed of light c this occurs in the observers frame in time $\frac{\tau}{c}(c - v\cos(\theta))$, so the apparent transverse velocity becomes:

$$v_{app} = \frac{v\tau sin(\theta)}{\frac{\tau}{c}(c - v\cos(\theta))}$$

Which for $\beta = v/c$ becomes (Kellermann and Owen 1988):

$$v_{app} = \frac{vsin(\theta)}{(1 - \beta\cos(\theta))} \tag{1.7}$$

This equation has a maximum at $v_m \sim c$, for Lorentz factor $\gamma = (1-\beta)^{-1/2}$, which occurs at $\theta = \sin^{-1}(1/\gamma)$.

The Doppler shift is given by:

$$\delta = \frac{1}{\gamma(1 - \beta\cos(\theta))}$$

or, corrected for redshift z:

$$\frac{(z-1)}{\gamma(1 - \beta\cos(\theta))}$$

and the radiation is Doppler boosted by an amount $[\gamma^{(\alpha-3)}(1-\beta\cos(\theta))]^{(\alpha-3)}$ (Kellermann and Owen 1988), where $\alpha = 1/\gamma$.

A nice example of superluminal motion is 3C279, as shown by Wehrle et al. (2001) and reproduced here in Figure 1.6 panel (b), which shown superluminal motion of several components, with apparent jet speeds of 4.8 to 7.5 c.

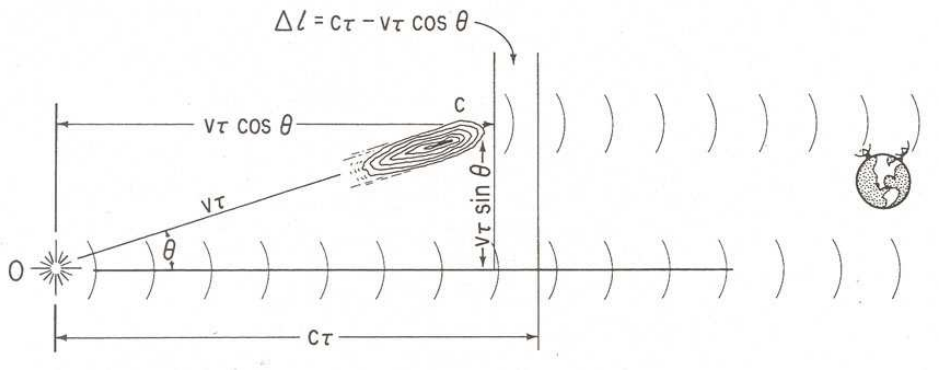

(a)

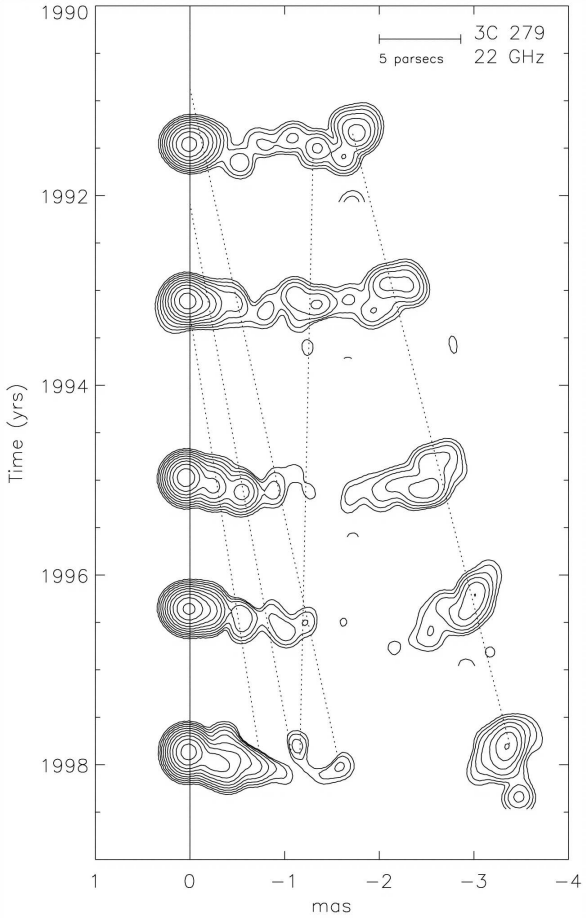

(b)

Figure 1.6 (a) Apparent superluminal motion of a component moving nearly along the line of sight to the observer, at speed v. Figure from Kellermann and Owen (1988). (b) Superluminal motion in several components of 3C279, with an apparent jet speed of 4.8 to 7.5 c. Image from Wehrle et al. (2001).

1.8 Radio - Gamma-Ray Connection

As mentioned, a proposed model for the gamma-ray emission observed from these objects is the upscattering of photons via the inverse Compton effect (Maraschi et al. 1992). This involves collisions between low energy photons and highly relativistic electrons resulting in the photons gaining energy.

In quasars the electron population involved is thought to be that in the jet. The low energy photons could either be those produced by synchrotron emission from the interaction between the electrons and the magnetic field of the jet (Bloom and Marscher 1996), or be produced external to the jet itself (Maraschi et al. 1992) or both. Either way, (but especially if the former is the case) the radio synchrotron emission and the gamma ray inverse Compton emission would be closely related.

It is remarkable that the radio and gamma-ray emission is related, despite being at opposite ends of the spectrum. If this link were better understood it would allow the full resources available at radio frequencies to promote an understanding of the physical processes occurring. Radio astronomy has a large advantage in terms of high angular resolution as well as sensitivity and oversubscription rate (there are simply more radio observatories) over gamma-ray studies.

1.8.1 EGRET Era

Examining the variability of blazars at both radio and gamma-ray frequencies provides information on the nature of this link, and hence the emission mechanisms of the gamma-ray radiation.

The Energetic Gamma Ray Experiment Telescope (EGRET) was an instrument onboard the Compton Gamma Ray Observatory which operated between 1991 and 2000. This was the first instrument that could detect high energy (20 MeV to 30 GeV) gamma-rays with good positional accuracy for individual photons of ~ 0.5 degree at 5 GeV, allowing for localisation of bright sources to around half a degree and thus more reliable source identification at other wavelengths. The primary purpose of EGRET was to perform an all sky survey. This was completed in 1999 and released as the third EGRET catalogue (Hartman et al. 1999). EGRET identified 271 sources, including one solar flare, 5 pulsars, the radio galaxy Centaurus A and 66 blazars.

EGRET was not however designed with these sources in mind, unlike *Fermi* it was a pointed instrument and not suited to monitoring a large number of sources with high time resolution, and as such no monitoring program was envisaged. As most of the analysis methods used to investigate the possible relationship between radio and gamma-ray emission require well sampled lightcurves over flaring periods in the source this made it difficult to investigate this property of blazars. Some flares were observed with EGRET however, and inferences based on the detection strength and the type of radio source could be made.

As EGRET started detecting radio sources at gamma-ray frequencies it was soon apparent that the majority of these sources were flat spectrum, blazars, BL Lac objects, optically violent variables, or superluminal sources, most of which were found to have redshifts greater than one (Fichtel et al. 1994). Further investigation showed that for several of these sources, radio, optical and X-ray activity was higher than normal within several months of the EGRET observations (Hartman et al. 1992, 1993; Hunter et al. 1993).

Reich et al. (1993) then presented radio light curves from the Effelsberg 100 m and the IRAM 30 m telescopes for 12 of the extragalactic sources detected by EGRET. Recognising the tendency of blazars to show gamma-ray emission, they initiated a monitoring program of all flat spectrum sources with flux densities greater than 1 Jy (at 6 cm) that would be in the field of view of EGRET. They found that all extragalactic sources detected at gamma-rays were variable, radio loud, and compact. Six exhibited superluminal motion, and most appeared to show variability at gamma-ray frequencies as well. They argued that the EGRET detections were likely to be at the peak of the sources gamma-ray intensity, and thus their radio monitoring showed that sources were likely to flare in the radio within several months after a gamma-ray flare. They also noted that the radio flares occured first at higher frequencies. These observations implied gamma-ray production occurred in the jet and suggested highly beamed sources.

Valtaoja and Terasranta (1995) followed this with Metsahovi monitoring of around one hundred of the brightest (northern) AGN. They included 16 of the 38 then gamma-ray detected sources in their analysis. Valtaoja and Terasranta (1995) split each of the monitored sources into high polarisation quasars (HPQ, optical polarisation $> 3\%$), low polarisation quasars (LPQ), radio galaxies (RG) and BL Lac objects (BL) and found that HPQs were much more likely to be detected by EGRET. They also found that 21 of the 25 EGRET detections of these sources were when the millimetre radio flux was rising or peaking. This strong correlation led them to conclude that the radio and gamma-ray flares observed in these sources must be produced by the same shocked regions of the jet, implying inverse Compton emission as the likely cause of the gamma-rays.

Unfortunately the sensitivity and sampling rate of EGRET did not allow for proper correlation analysis of individual flares. If this relation were to bear out however, it suggests the low energy photons being upscattered to gamma-ray frequencies are those produced in the jet itself, and that the gamma-ray emission is due to shocks occurring in the jet.

Considering the relativistic nature of the jets, the suggested delay between the radio and gamma-ray flares implies the gamma-rays are produced parsecs from the core of the AGN (Lähteenmäki and Valtaoja 2003). Such a result casts doubt over an external source of low energy photons, in a region well beyond the broad-line region of the AGN. This is potentially very interesting as it would then be possible with high frequency VLBI and space-VLBI to directly image the evolving shocked regions where the gamma-rays are generated (Jorstad et al. 2001b). VLBI measurements of the jet kinematics have been made, providing constraints on the viewing angle, intrinsic velocities of the jet and therefore the degree of beaming (Lister

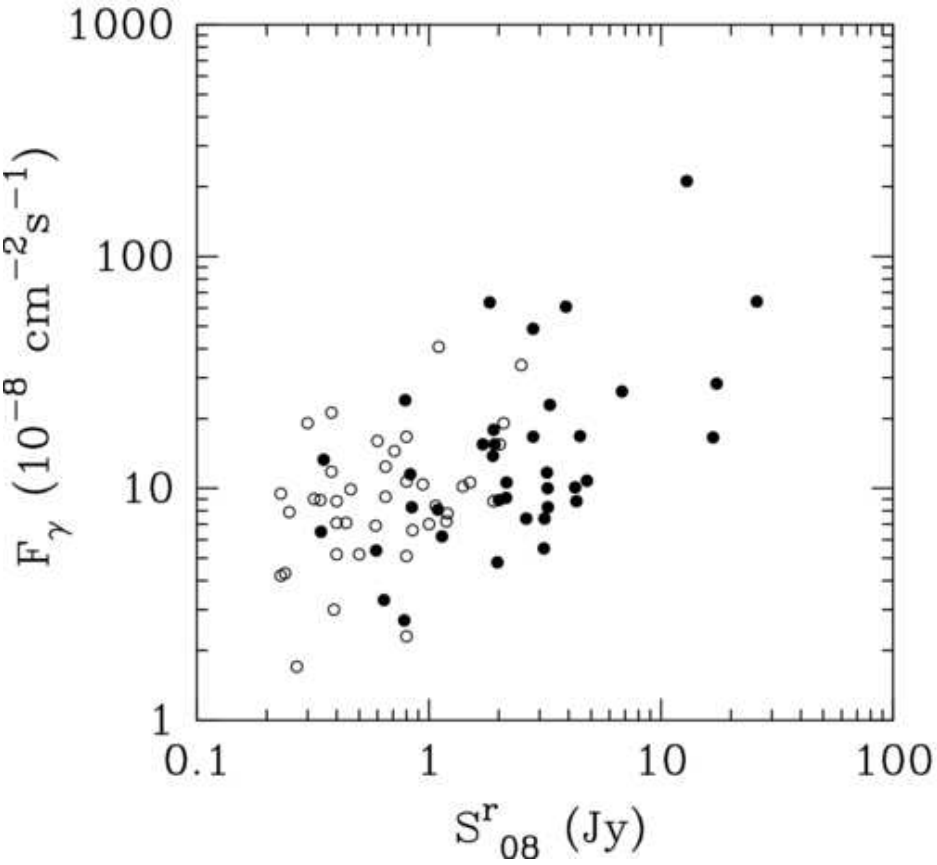

Figure 1.7 From Kovalev et al. (2009), *Fermi* LAT 100 MeV-1 GeV photon flux vs. quasi-simultaneous 15 GHz flux density. The filled circles represent total VLBI flux density while open ones are single-dish flux density. A correlation between the two was found with confidence level $> 99.9\%$.

et al. 2001; Kellermann et al. 2004).

1.9 The *Fermi* - LAT Era

The Large Area Telescope (LAT) onboard the *Fermi* Gamma-ray Space Telescope is the mission's primary instrument. *Fermi* was launched in June 2008 and commenced science operations by August. LAT has a field of view of roughly 20% of the sky, and covers the energy range from 20 MeV to 300 GeV. LAT operates continuously, scanning the entire sky once every three hours. LAT has a resolution of around 3 degrees at 100 MeV improving to arcminutes at 300 GeV. Most sources are typically detected at energies resulting in error circles for their positions of the order of 10 arc-minutes. The scanning nature of LAT makes it excellent for analysing the time dependent behaviour of gamma-ray detected blazars.

Kovalev et al. (2009) analysed the first three months of LAT observations, including only 10 σ or stronger detections positionally associated with radio-loud blazars. The MOJAVE radio sample used in their analysis consists of 135 sources with parsec scale flux density

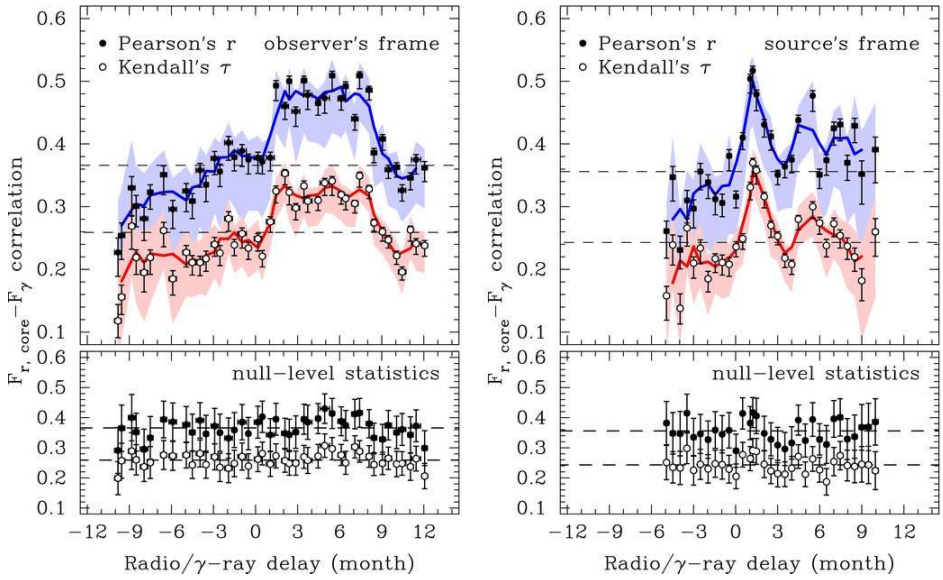

Figure 1.8 From Pushkarev et al. (2010), upper panel: flux-flux correlation level vs lag between *Fermi* and radio flux density measurements in both the observer (left) and source frames (right). Note the sharp peak in the source frame at a delay of 1-2 months. The lower panel shows the null level correlation based on the sampling.

greater than 1.5 Jy (at 15 GHz). The radio observations used were in the most part made with the Very Long Baseline Array (VLBA). Where VLBA observations contempane with the LAT observations were not available, single dish observations were used to infer the parsec scale flux. This was possible due (as previously mentioned) to the extremely compact nature of these sources. A correlation between *Fermi* LAT 100 MeV - 1 GeV photon flux and quasi simultaneous 15 GHz flux density was found, with a confidence level greater than 99.9% (Figure 1.7).

Kovalev et al. (2009) also found that radio-selected blazars were more likely to be detected by LAT if they were in an active radio state during the LAT observation period. This is further evidence linking radio flaring to gamma-ray activity. They conclude that gamma-ray and parsec scale radio emission is strongly related in bright gamma-ray objects. Again, gamma-ray bright sources were found to be brighter and more compact than other blazars, suggesting high Doppler factors.

Further work then found that the jets of LAT detected blazars have higher than average apparent speeds, with a median of 15 c (Lister et al. 2009), as well as large apparent opening angles, with a median of 20 degrees (Pushkarev et al. 2009), and high Doppler factors, with a mean of 20 (Savolainen et al. 2010).

Pushkarev et al. (2010) then attempted to constrain the lag between flaring at gamma-ray and radio frequencies for these sources. MOJAVE at this point monitored 186 sources with LAT detections. The time sampling of the VLBA based monitoring in their sample was not high enough to attempt a correlation analysis on an individual source directly. As

such the authors undertook a statistical approach, using 564 VLBA images and model fits for 183 bright LAT detected sources. All pairs of measurements for which the time difference between the radio and gamma-ray observations lay within a certain interval (for example -0.5 to +0.5 months) were then collated, and the time interval shifted by half a month each time. Pearson's r and Kendall's τ correlation coefficients were finally calculated for the resultant lag pairs. The results are shown in Figure 1.8. There is a clear increase in both the correlation coefficients between 1 and and 8 months lag. This correlation was found to tighten significantly when the radio/gamma-ray time difference was transferred to the reference frame of the sources. This gave a time delay of ~ 1.2 months in the source frame, which corresponds to ~ 2.5 months in the observer's frame for a $z = 1$ source (with the gamma-ray leading). The time delay observed and the fact the gamma-ray emission was found to lead the radio flaring, caused the authors to suggest the delay between gamma-ray and radio flaring may be due to optical depth effects. Some evidence to support this was found by comparing the critical radius (from the core) at which the jet becomes optically thin. By using typical parameters for a LAT detected radio loud blazar, they find the distance between the gamma-ray production zone and the $\tau \approx 1$ surface at 15 GHz (which is the radio core) to be roughly 7 pc. This is consistent with an estimate for the core radius obtained using core-shift measurements (O'Sullivan and Gabuzda 2009).

1.10 Interstellar Scintillation - Microarcsecond Structure

Scintillation at centimetre radio wavelengths is caused by turbulence in the inter-stellar medium (ISM) of our Galaxy. The turbulence acts like a number of small lenses moving across our field of view which in turn magnify and de-magnify the background light (Figure 1.9).

This turbulence scatters the waves into a distribution of width θ_{scatt} which is usually milliarcseconds at radio frequencies. The coherence scale $s_d = 1/(k\theta_{scatt})$ is the scale over which there is a one radian difference in phase, where k is the radio wavenumber. This difference in phase then causes constructive and destructive interference at distances L from the source. If the phase change is less than one radian across a Fresnel region, $s_d > r_f$ where $r_f = \sqrt{L/k}$ is the Fresenel scale, the scintillation is known as 'weak'. That is, the change in intensity is less than the mean. In this case the timescale of scintillation is given by:

$$t_{weak} \sim r_f/V = \sqrt{L/k}/V \tag{1.8}$$

where V is the inter-stellar scintillation (ISS) pattern velocity.

In the strong scattering case, where $s_d < r_f$, two effects become important in the diffraction pattern, diffractive and refractive scattering. These are governed by the diffractive scale (s_d again) and the refractive scale $s_r \sim L\theta_{scatt}$ (Rickett 2002). The two timescales of scintiallation then become:

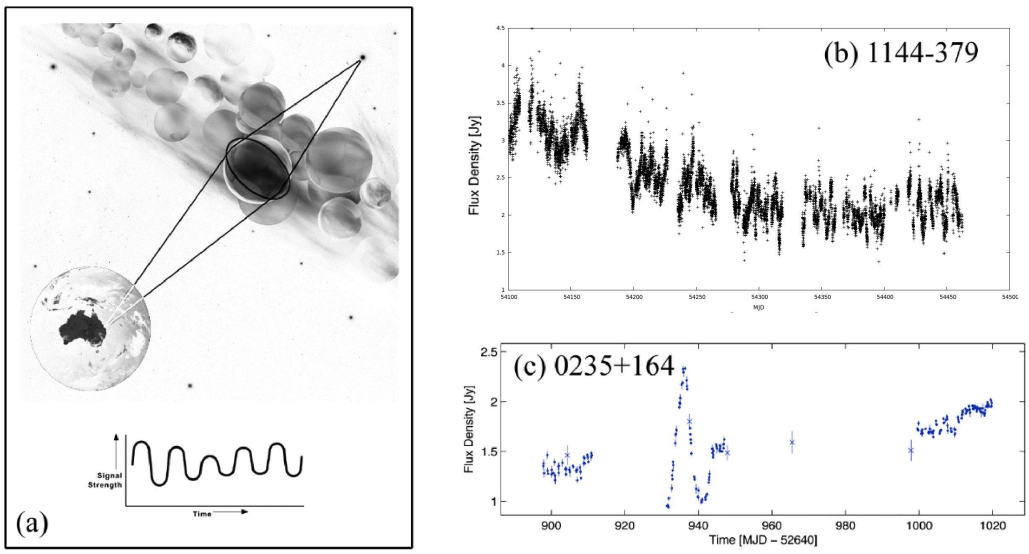

Figure 1.9 (a) A schematic of interstellar scintillation. The turbulent inter-stellar medium (ISM) acts as a number of small lenses, distorting the wavefront from the AGN. As the Earth moves with respect to the ISM screen, an observer sees induced AGN variability Image Credit: Renee Dillon, CSIRO. (b) One year of Ceduna 30m monitoring data of PKS 1144−379. The source scintillates strongly and there is a correspondence between amplitude of scintillation and long term mean flux density. (c) An Extreme Scattering Event (ESE) seen by Ceduna in the blazar 0235+164. A 1.5 Jy deflection was observed over just a few days (Senkbeil et al. 2008).

$$t_d \sim 1/(Vk\theta_{scatt}), t_r \sim L\theta_{scatt}/V \tag{1.9}$$

In AGN, low frequency scintillations with timescales of months have been observed, and are due to refractive scintillation, which is less affected by angular size restrictions (Rickett 1986; Hunstead 1972). Short timescale, intra day variability (IDV) has been observed for a few sources, and is usually seen at 5 - 10 GHz (Rickett 2002).

A sample of 443 flat spectrum radio sources were then monitored with the VLA at 5 GHz (Lovell et al. 2003, 2008). It was found that over half the observed sources showed variablity of the order of 2-10%, and this variability was connected to interstellar scintillation of a compact region with apparent angular diameter of 10-50 micro-arcseconds. MASIV showed, for the first time, that the dominant mechanism for IDV at centimetre wavelengths is inter-stellar scintillation.

Monitoring of blazars using dedicated short baseline interferometers for signs of scintillation thus provides indirect information on the microarcsecond-scale structure of the relativistic radio jets (Macquart and de Bruyn 2007). This is important when studying blazars, as flaring at both gamma-ray and radio frequencies is likely occurring within the jet. Scintillation is such a valuable tool to reveal evolution in a jet, such as a new component, which may be correlated with flaring activity.

1.11 This Thesis

This thesis presents an investigation into the multi-frequency properties of blazars. Chapter 2 presents the Ceduna - Hobart Interferometer (CHI), a new instrument capable of quick turn around, target of opportunity core flux density measurements of southern sources. Chapter 3 examines the MASIV survey and the LAT 2-year Point Source Catalogue (2FGL) for any possible links between scintillating and gamma-ray bright sources. Chapter 4 presents VLBI observations of the blazar PKS 0208−512, as well as modelfitting of jet components to calculate an apparent jet speed. In Chapter 5 a time series analysis of the multi-frequency light curves of PKS 0208−512 is performed and discussed. Chapter 6 presents multi-epoch spectral energy distribution modelling of PKS 0208−512. Chapter 7 outlines a similar analysis as performed in Chapter 5 for a further three sources, PKS 1424−418, PKS 1622−253 and PKS 2052−474. Finally Chapter 8 summarises and concludes this thesis.

Chapter 2

Ceduna–Hobart Interferometer

The material in this chapter is taken in most part from Blanchard et al. (2012):
Blanchard, J. M., Lovell, J. E. J., Ojha, R., et al. 2012, A&A, 538, A150

The structure and some wording has been altered somewhat to better fit the flow of this thesis.

2.1 Introduction

The launch of the *Fermi Gamma-ray Space Telescope* (formerly GLAST; Atwood et al. 2009) on June 11th, 2008, has ushered in an era when it is possible to observe astronomical objects, including AGN, simultaneously across the entire electromagnetic spectrum. Such multiwavelength observations are essential to understand the behaviour of astronomical objects in general and AGN in particular. This motivated the TANAMI program (Tracking Active Galactic Nuclei with Austral Milliarcsecond Interferometry; Ojha et al. 2010) which provides radio monitoring of γ-ray loud sources (and a control sample) south of -30 degrees Declination.

TANAMI observations are made at two radio frequencies using the telescopes of the Australian Long Baseline Array (LBA; e.g. Ojha et al. 2004) augmented by telescopes in South Africa, Chile, Antarctica and New Zealand. This array allows the imaging of the southern sky at milliarcsecond scale or better resolution on a regular basis (e.g., Müller et al. 2011). This observational technique, called Very Long Baseline Interferometry (VLBI), is essentially the only way to measure intrinsic parameters of the jets seen in AGN, as multi-epoch VLBI observations provide the sole direct measurements of their relativistic motion (Cohen et al. 2007). They also play a crucial role in the identification of the nature and location of regions where γ-ray emission originates in AGN (Jorstad et al. 2001a; Agudo et al. 2011). TANAMI VLBI observations are supported by radio monitoring programs at arc-second resolution using the Australia Telescope Compact Array (ATCA) and single-dish resolution using the Ceduna radio telescope (McCulloch et al. 2005). With its associated optical/UV and X-ray programs and its unique VLBI dual-frequency characteristics, TANAMI has become one of the major

multiwavelength resources for the *Fermi* mission and the only one covering sources south of −30 degrees. TANAMI VLBI observations are constrained, however, by the availability of the LBA which only observes in approximately one week blocks every 2∼3 months. This makes it difficult to quickly observe a southern source that exhibits interesting behaviour such as rapid changes in flux density at one or more wavebands. Target-of-opportunity proposals are possibly with the LBA, however as most individual telescopes are heavily subscribed a strong case must be made and a limited array often results.

The Ceduna Hobart Interferometer (CHI) was developed to provide rapid, high resolution observations of sources in the southern sky. A fundamental characteristic of AGN is their variability at all wavelengths in which they are detected (Ulrich et al. 1997; Abdo et al. 2010). Thus a proper study of the physics of AGN requires simultaneous multiwavelength observations, particularly when the flux density of an object changes significantly over a short period of time. Here the specific observational procedures and calibration techniques that have been developed to create this uniquely useful single-baseline interferometer are described. It is important to note that, even though the development of CHI was motivated by the *Fermi* and TANAMI programs, it is by no means restricted to observations of γ-ray loud AGN but can be used for multiwavelength study of a range of compact sources e.g. optically flaring AGN, X-ray sources being studied by the INTEGRAL and Swift satellites, TeV sources detected by H.E.S.S., radio supernovae and some microquasars.

In this chapter, the CHI instrument is described (Sect. 2.2) as well as the observing strategy (Sect. 2.3). The non-standard calibration procedures are then explained (Sect. 2.4) and some results presented in Sect. 2.5. A summary and description (Sect. 2.6) of further development planned for CHI concludes this chapter.

2.2 CHI: The Ceduna Hobart Interferometer

The Ceduna Hobart Interferometer is a single baseline interferometer formed by a 26 meter antenna located at Mount Pleasant, Hobart and a 30 meter antenna located at Ceduna in South Australia. They are both re-purposed antennas that are now operated by the Radio Astronomy group at the University of Tasmania. CHI has a physical baseline length of 1704 km corresponding to a resolution of 6.6 milliarcseconds at its current operating frequency of 6.7 GHz. The Hobart antenna is at a latitude −42.8 degrees while the Ceduna antenna is at latitude −31.87 degrees. Thus CHI can, in principle, observe sources up to mid-northern latitudes and can easily observe the entire southern hemisphere.

The 30m telescope at Ceduna is a former Telstra Satellite Earth Station, that was converted to astronomical use after its acquisition by the University of Tasmania in 1995. Ceduna uses a standard alt-azimuth mount, with a slew rate of 40 degrees per minute on each axis and an elevation limit of 10 degrees. It is a critical component of the Australian LBA, providing the major east-west baselines. However, Ceduna is primarily used for single dish programs monitoring γ-ray bright AGN in support of the TANAMI program as well as Intra Day

Variable (IDV; Wagner and Witzel 1995) AGN in support of the MASIV (Microarcsecond Scintillation-Induced Variability; Lovell et al. 2003, 2008) program. Ceduna is capable of observations at 2.2, 4.8, 6.7, 8.4, 12.2 and 22 GHz using room temperature receivers. Since the peak variability in amplitude of scintillating AGN is expected to be close to a frequency of 6.7 GHz, IDV observations are carried out in this band. As receiver changes at Ceduna are not automated, the standard observing frequency for CHI was selected to be 6.7 GHz, allowing for a rapid change between observing programs. Despite being uncooled, the 6.7 GHz receiver has a System Equivalent Flux Density (SEFD) of roughly 820 Jy, equivalent to that at Hobart. This is mostly due to the larger collecting area of the 30m dish, as well as the focus type. Hobart is a prime focus instrument with more spillover than the tertiary system at Ceduna.

The 26m telescope at Mount Pleasant was opened on 13 May 1986 after having been moved from Orroral Valley in the Australian Capital Territory where it had been a NASA tracking station for about two decades. It also is a component of the Australian LBA and a vital geodetic antenna regularly participating in International VLBI Service (IVS; Schlüter and Behrend 2007a) observations. Hobart uses a non traditional X-Y mount slewing at 40 degrees per minute on both axes to an elevation limit of 7 degrees (apart from a 17 degree limit in the keyhole) and can observe at all major astronomical frequencies from 1.4 through 22 GHz. The 6.7 GHz receiver at Hobart is cooled to 20 K using helium cryogenics, giving a system equivalent flux density of approximately 820 Jy. The backend system at both telescopes produces two channels (right and left hand circular polarisation) of 32 MHz bandwidth. The baseline sensitivity (in mJy) of a 2 element interferometer is given by equation 2.1 (Thompson et al. 2001).

$$\Delta S_{ij} = \frac{1}{\eta_s}\sqrt{\frac{SEFD_i \times SEFD_j}{2\Delta t \Delta \nu}} \tag{2.1}$$

where η_s is the system efficiency (roughly 0.88 for 2 bit sampling), $SEFD$ is the system equivalent flux density in Jy of each antenna, Δt is the integration time in seconds and $\Delta\nu$ is the bandwidth in MHz.

Thus, in just 60 seconds of integration time, CHI can reach a baseline sensitivity of about 15 mJy which is sufficient to observe all the sources in the TANAMI program. The coherence time at 6.7 GHz is approximately 4.6 minutes (calculated using the methods outlined in Briggs 1983 and checked against the given values in Walker 1995). This gives a maximum baseline sensitivity of approximately 7 mJy without phase referencing, more than enough to detect the above mentioned sources. Table 2.1 lists the brightness temperature sensitivity of CHI to a hypothetical 1 Jansky source for a range of parameters.

CHI data are recorded to disk at 256 Mbps at 2 bit sampling with the LBA Data Recorder system(Phillips et al. 2009) and the Ceduna disks are shipped to Hobart for correlation. The data are correlated using an installation of the DiFX software correlator (Deller et al. 2007). The correlator itself consists of a cluster of 6 PCs each containing dual quad-core Xeon

processors and 3 GB of memory. The correlator can manage data rates of up to 512 Mbps on a single baseline, giving a 2 times real time correlation speed for a typical CHI observation. The biggest constraint on the speed of analysis of data from CHI however is the time taken for disks from Ceduna to be shipped to the correlator in Hobart. This means a typical turn around time of around 5 days for data to be fully reduced. Transfer over network is not possible due to the limited network capacity to Ceduna and the volume of data recorded.

2.3 Observing Strategy for flaring AGN

Due to the peculiar calibration needs of a single baseline interferometer (see section 2.4) and the desire to obtain good absolute amplitude calibration, a non-standard observing strategy has been developed. A typical CHI observation runs for twelve hours. Each hour consists of a roughly 50 minute long scan on the target source and a ten minute scan of PKS B1934−638, the primary amplitude calibrator of the ATCA. PKS B1934−638 is observed as traditional amplitude calibration is not possible with a single baseline (see section 2.4 for a discussion).

Observations are usually triggered following an increase in gamma-ray activity as found by the *Fermi* LAT instrument. The flaring source is also added to the single dish monitoring program, providing a high cadence lightcurve at the observing frequency. If the source is observed to be flaring at radio frequencies multiple CHI observations are then undertaken to provide information on the state and evolution of the flare.

2.4 Calibration

Calibration of an interferometer with just two elements presents several interesting challenges. Since a minimum of 3 antennas is required for phase closure and 4 antennas for amplitude closure, it is not possible to use the standard VLBI tools of hybrid mapping (Readhead et al. 1980) or self-calibration (Pearson and Readhead 1984). Thus non-standard amplitude calibration must be performed on CHI data. Calibration requires two stages, a once off initial calibration and a calibration applied to each individual CHI observation.

2.4.1 Initial Calibration

The need for amplitude calibration using a calibrator source is well met by PKS B1934−638, which has a flux density of 3.983 Jy at 6.7 GHz and does not vary significantly (Reynolds 1994). Unfortunately, at VLBI resolutions, PKS B1934−638 is not a point source and so a model is required in order to make amplitude calibration possible.

To create the model of PKS B1934−638, data from the V255 series of Australian LBA observations were used. The V255 project focuses on methanol maser studies at 6.7 GHz, making use of VLBI to measure accurate positions, distances and proper motions of these masers. PKS B1934−638 was observed in the V255 observations to act as a polarisation

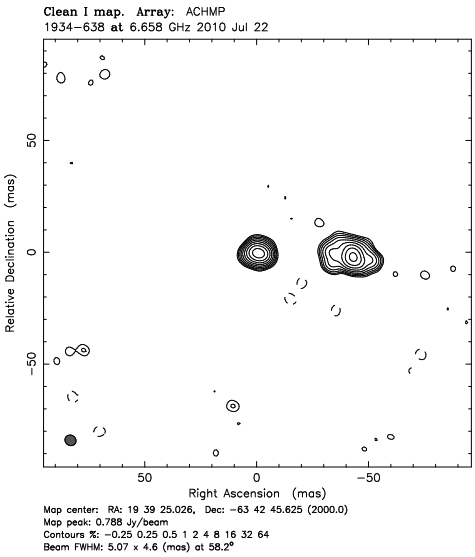

Figure 2.1 The brightness distribution of PKS B1934−638 derived from the model created using AIPS and Difmap.

calibrator. Three epochs of V255 were used to make the model of PKS B1934−638 used for CHI. As part of the calibration the effect of elevation on the gain of the receiver must be corrected for. These gain-curves are not available for all LBA antennas at 6.7 GHz. Gain-curves from existing 8.4 GHz data were adjusted for the new frequency for telescopes that did not have 6.7 GHz curves available. For Ceduna the gain-curve was taken from McCulloch et al. (2005). For Hobart it is approximated as a first order polynomial and this may introduce a small elevation effect into CHI data (see Figure 2.3).

Finally the absolute flux scale of the PKS B1934−638 model at 6.7 GHz was set using simultaneous ATCA and LBA data of several point sources (0506−612, 0808+019, 1022−665 and 1420−679). This was not possible to achieve using the PKS B1934−638 data itself as PKS B1934−638 is resolved on VLBI baselines. For a point source however the VLBI and ATCA fluxes should be the same and so the difference in VLBI and ATCA flux density was calculated for each of the point sources mentioned above, giving an average correction factor of 1.45 ± 0.2 used to scale the model of PKS B1934−638. This gave the final clean component model as seen in Figures 2.1 and 2.2. The error in this correction factor (of order 15 percent) is by far the dominant form of error in flux density measurements made using CHI and is thus used as an estimate of the total error in such measurements.

2.4.2 CHI Calibration

As described in section 2.3, PKS B1934−638 is observed in each CHI observation to perform additional amplitude calibration, as required by the single baseline. The CHI data (including both the target source(s) and PKS B1934−638) are initially calibrated in AIPS (Astronomical

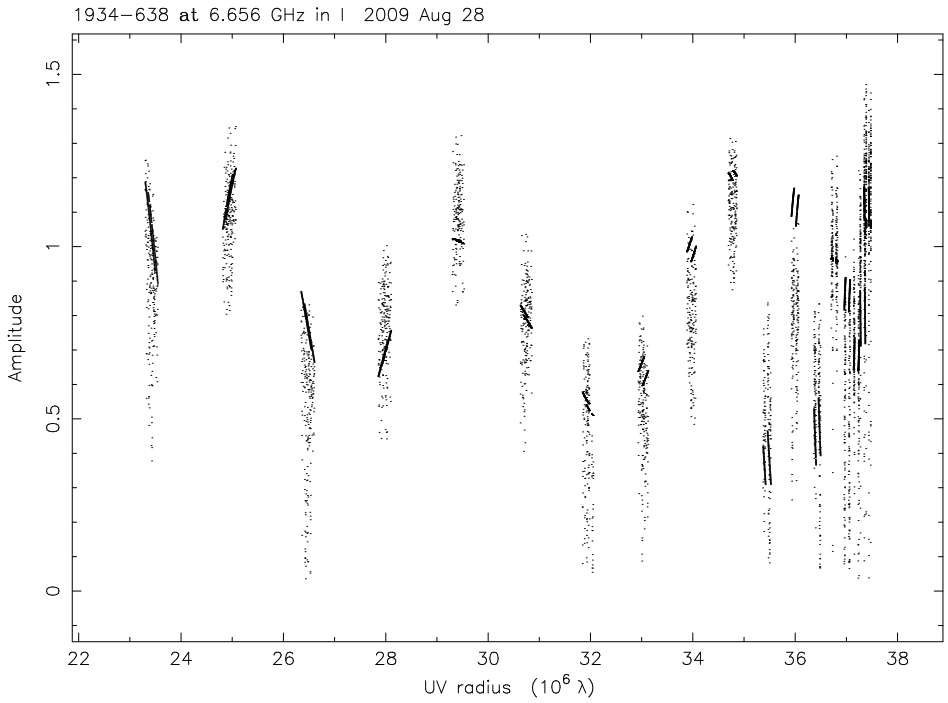

Figure 2.2 Calibrated PKS B1934−638 amplitude vs (u, v) distance plot with the overlaid model.

Image Processing System; Greisen 1998) in the standard manner. Fringe-fitting is carried out to correct for residual delay and rate errors. This is followed by amplitude calibration using the known gain-curves and system temperature measurements made at each antenna over the course of the experiment.

The AIPS calibrated PKS B1934−638 data are loaded into the Caltech Difference Mapping program 'Difmap' (Shepherd et al. 1995) and the model created as described in Section 2.4.1 is then overlaid on an amplitude vs (u, v) distance plot. A simple script is then used to manipulate the model to fit both the amplitude vs (u, v) distance plot (see Figure 2.2) and an amplitude vs time plot, giving a correction factor.

This correction factor is then used to scale the visibilities of the baseline producing the final calibrated source observation.

2.5 Results

Here a typical CHI observation is presented. PKS 2052−474 is a blazar at a redshift of 1.489. It is established to be a variable gamma-ray source. Abdo et al. (2010) show a light curve with two flaring events, occurring around February and June 2009 respectively. Previous VLBI observations have found the source to be strongly core dominated on the milli-arcsecond scale (Ojha et al. 2010, 2004; Piner et al. 2007). On the kilo-parsec scale, ATCA imaging shows some extended structure (Marshall et al. 2005; Burgess and Hunstead 2006) extending

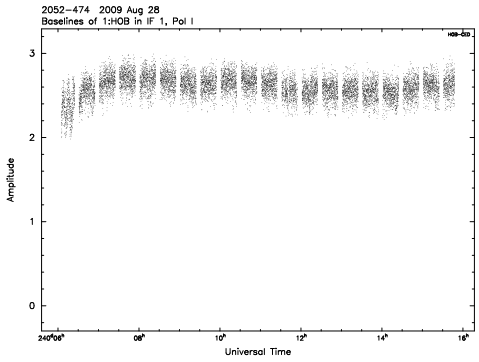

Figure 2.3 Amplitude vs time plot for the calibrated 2052−474 observation. Note the downturn in amplitude at the beginning of the experiment. This corresponds to low elevation of the source and is thus likely a residual elevation effect. This is perhaps due to the simple nature of the gain-elevation curve for the Hobart Antenna

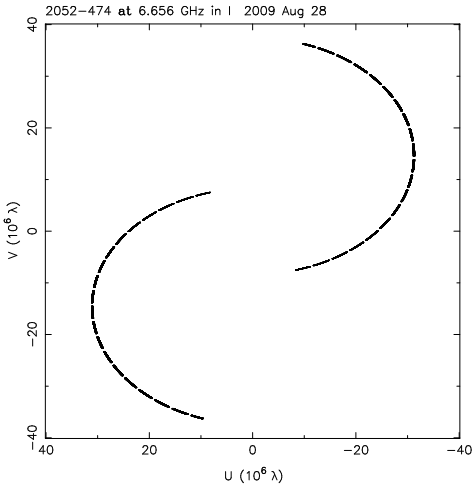

Figure 2.4 The (u, v) coverage obtained from a 12 hour CHI observation of 2052-474. This is typical of a CHI experiment.

over 4 arc-seconds. The observation presented here was made in support of a *Fermi*/LAT multiwavelength campaign on this object in 2009 (Chang et al. 2010) following the flaring seen in the gamma-ray.

Calibration was performed as explained in section 2.4, resulting in the amplitude vs time plot seen in Figure 2.3 and the amplitude vs (u, v) distance plot seen in Figure 2.6. This is consistent with a point source with a flux density of 2.6 Jy. Figure 2.5 shows single dish data from the Ceduna monitoring program, as well as ATCA data from the C1730 gamma-ray sources monitoring program, around the time of the CHI observation. The flux density obtained from the CHI observations is consistent with that of the single dish data (as expected for an unresolved source) giving us confidence in the amplitude calibration technique employed by CHI. The (u, v) coverage of a typical CHI observation is shown in

Figure 2.4. Applying the radiometer equation (equation 2.1) to this 7 hour observation of PKS 2052−474 gives an expected noise of 0.73 mJy rms, agreeing well with the observed noise in the visibilities of 0.75 mJy rms.

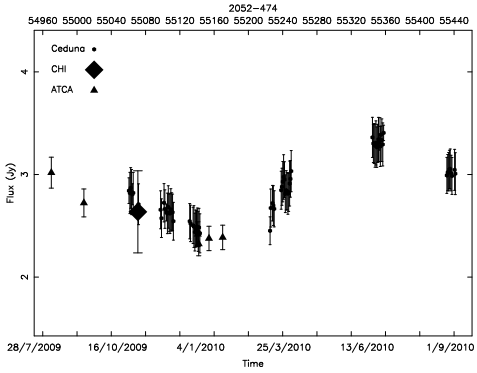

Figure 2.5 Single dish and ATCA monitoring data of PKS 2052−474 overlaid with the CHI observation (the large filled diamond). The Ceduna data are the circles and the ATCA data the triangles. The VLBI data is consistent with both the single dish and the ATCA monitoring flux density. Note that the ATCA data are interpolated between simultaneous 5.5 and 9 GHz data to match the 6.7 GHz Ceduna single dish data.

A constraint on the angular size of the source can be calculated by applying a Gaussian model to the visibilities. For this example observation of 2052−474 a model with an angular size of 0.8 mas is chosen, as the visibilities are well encompassed by the model (see Figure 2.6). Note that no attempt has been made to fit to the data directly, rather a gaussian was chosen which lies below the majority of the visibilities, thus providing an upper limit to the angular size.

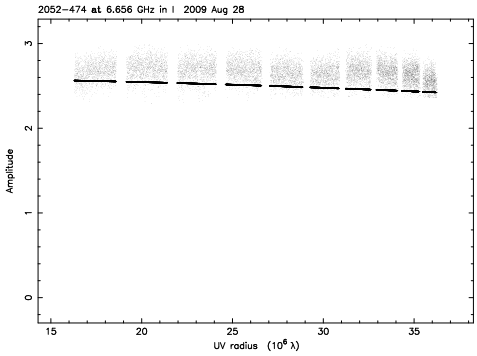

Figure 2.6 Amplitude vs (u, v) distance plot of the calibrated 2052-474 CHI data. A model with major axis of 0.8 mas and an axial ratio of 1 well constrains the visibilities, giving an upper limit on the angular size of the source. Note the choice of model is not a fit to the data but rather lies below the majority of points to give an upper limit to the angular size.

The brightness temperature of a source is given by

$$T_b = \frac{2ln2}{\pi k} \frac{S_\nu \lambda^2 (1+z)}{\theta_{maj}\theta_{min}} \tag{2.2}$$

where k is Boltzmann's constant, S_ν is the flux density of the source, λ is the wavelength, z is its redshift and θ the angular size (see for example Kovalev et al. 2005).

Using the upper limit to the angular size of the source and equation 2.2, a lower limit of 2×10^{11} K for the brightness temperature is calculated. This is well below the inverse Compton limit.

2.6 Summary and Future Developments

The CHI interferometer is the only facility capable of rapid, high resolution observations of compact radio sources south of about -30 degrees declination. The peculiar calibration challenges of such a single baseline interferometer have been met and initial results are presented. Currently CHI is a critical component in the multiwavelength study of AGN in the age of *Fermi*. However, its role is set to be broader as it is capable of observing any type of compact radio source in the southern sky with high sensitivity.

There are three developments under active consideration for CHI. First, observation at multiple radio frequencies would provide radio spectral index measurements which are very useful inputs to models of the emission from AGN. Both Hobart and Ceduna can observe at the standard centimetre wavelength radio bands. The calibration will be expanded to additional frequencies of 2.3, 8.4 and 22 GHz, in order to make CHI capable of spectral index measurements.

Second, while CHI observations can be initiated almost instantly, the remote nature of the Ceduna observing site makes the shipping of data to the correlator in Hobart the biggest bottleneck to rapid analysis. The possibility of taking preliminary measurements using a 'sniffing' strategy is being explored. This would involve taking short (about one second) slices of the twelve hours of data and transferring them back via network, thus decreasing the transfer time without sacrificing (u, v) coverage too much. This would allow a quick analysis showing the flaring state of a target (for example) where such information is needed to trigger observations at other wavelengths.

Finally, the possibility of including the new 12 meter antenna at Warkworth, New Zealand (Gulyaev et al. 2011) in the CHI array is being investigated. This would increase the maximum baseline to 3724 kilometers boosting the resolution 2.5 times at an observing frequency of 8.4 GHz, as well as providing phase closure.

Table 2.1. Brightness Temperature Sensitivity

Redshift	Shape	Brightness Temperature[a] K
0	Gaussian	1×10^9
0	Sphere	0.5×10^9
0	Disc	0.4×10^9
1	Gaussian	2.2×10^9
1	Sphere	1×10^9
1	Disc	0.8×10^9

[a]For a 1 jansky source.

Chapter 3

Scintillation Analysis

Evidence of variability in the flux densities of extragalactic radio sources was first presented by Dent (1965). Dent found large variations in the flux densities of 3C 273, 3C 279 and 3C 345, and noted that each of these sources had flat radio spectra. Around the same time, Sholomitskii (1965) found variations in the flux density of CTA 102 of the order of 30%, although these were not confirmed until later.

Further studies focused mainly on individual sources and it was not until more statistically complete samples were optained that a link between flat spectrum sources and flux density variability, as well as source compactness, was confirmed (Rudnick and Jones 1982; Seielstad et al. 1983; Heeschen 1984). The quintessential radio blazar BL Lac was one of the first sources seen to show large day to day flux density variability (Heeschen 1984), and then Witzel et al. (1986) presented a lightcurve of 0716+71 showing intra-day 'flickering' on time scales of 10-30 hours.

Witzel et al. (1986) proposed two possible causes of the short time-scale variability: 1) Scintillation, or 2) intrinsic variation, and noted that intrinsic variation would require a brightness temperature in excess of $10^{18}K$ (well over the Compton limit) and thus Lorentz factors approaching 100. This is because the brightness temperature inferred from variability studies scales as the Doppler factor cubed (Lähteenmäki and Valtaoja 1999), and so to avoid breaking the inverse Compton limit, extremely high Doppler factors are required.

Further work (Kedziora-Chudczer et al. 2001; de Bruyn and Dennett-Thorpe 2001; Bignall et al. 2003) not only cast doubt on intrinsic variation being responsible for the short time scale variations, due to the excessive Doppler factors required, but also found a pattern in the variations consistent with an annual cycle, the variability timescale being more rapid when the Earth was moving opposite the motion of the turbulent medium. These findings suggested inter-stellar scintillation as the major cause of the intra-day variability observed, prompting a major survey (MASIV) of compact, flat-spectrum radio sources using the VLA, with the aim of providing a large statistically robust sample of sources and thus analyse both the microarcsecond nature of the sources themselves, as well as the properties of the ISM causing the scattering (Lovell et al. 2003, 2008). The observed sample was selected in two

groups based on catalogued 8.5 GHz flux densities, one containing sources with flux densities between 105 and 130 mJy and the other with flux densities greater than 600 mJy. In order for a source to scintillate its angular size must be comparable to the Fresnel scale of the cattering medium, giving an angular size of at most tens of microarcseconds.

Gamma-ray detected blazars show frequent flaring behaviour, with gamma-ray flares shown to be correlated with optical flaring, and in some cases radio flaring (see Chapters 5 and 7). This is (in some cases) consistent with a model in which a new, compact component is ejected from the radio core, causing flaring at various frequencies as the shocked region becomes optically thin (Linford et al. 2011). Such a compact, bright component is likely to scintillate strongly and in fact scintillation has been observed to increase in strength during radio flaring periods in PKS 1144−379 (see Figure 1.9) and possibly scintillation during flaring at both radio and gamma-ray frequencies in the case of PKS 1622−253 (Figure 7.13). The micro-arcsecond apparent size of scintillating sources is consistent with the parsec scale evolution of a gamma-ray blazar at redshift 1 (See Chapter 5). Unfortunately there is as yet no source for which radio and gamma-ray flaring, and consistent scintillation has been monitored at sufficient length and cadence. Therefore a statistical approach is attempted in order to determine if scintillating sources are linked with gamma-ray blazars, which would strengthen the likelihood of a physical link between gamma-ray flaring and scintillation.

The MASIV survey data also allows an analysis into the long term variability of both gamma-ray detected and scintillating sources at 4.9 GHz, including any potential intrinsic relationships.

3.1 Fermi-LAT vs MASIV

The Fermi LAT second year bright source catalogue lists associated radio sources, based on the error ellipse of the gamma-ray detection, and matching with preferrentially compact, flat spectrum sources from various radio surveys. See Table 6 of Nolan et al. (2012) for a full list of surveys used. In this analysis the positions of those Fermi associated radio sources were run through the NASA/IPAC Extragalactic Database, and all non radio galaxy sources were rejected (mostly pulsars, nebulae and so on).

These *Fermi* associated radio sources were then cross matched by position with the MASIV catalogue (the first four epochs) (Lovell et al. 2008), to within the reported error of the NED positions, and the MASIV positions. Positions were used instead of matching by name due to the various catalogues using different source names.

A flux density cutoff of $S > 0.3$ Jy for the MASIV data was imposed as, due to the scanning mode employed, there are very few low luminosity sources detected by *Fermi*-LAT, and as there is an overall (average) gamma-ray to radio flux density correlation (Linford et al. 2012), this results in only a small number of associated radio sources with flux densities less than 0.3 Jy, causing uncertain statistics at those flux densities. As mentioned, the MASIV survey had two groups of sources, weak and strong, and the flux density cutoff removes the

weak group, preventing their distribution from affecting the analysis.

This resulted in 95 sources associated with *Fermi* detections and MASIV. The number of these cross matched sources showing evidence of scintillation in at least one epoch of the MASIV survey results in 64/95 sources scintillating, or approximately 67%. When this is compared with all sources in MASIV that have $S > 0.3$ Jy, 146/230 of those sources are found to scintillate, which is approximately 63%.

A z two proportions test does not allow the rejection of a null hypothesis that the two proportions are identical, to greater than 99% confidence. Thus there is no statistically consistent difference between the fraction of *Fermi*-LAT detected sources that scintillate and the fraction of sources in all of the MASIV survey that scintillate.

3.2 MASIV vs *Fermi*-LAT

The previous analysis merely shows that *Fermi*-detected sources are no more likely to show scintillation than an average flat spectrum, compact radio source. However, the question still remains if *Fermi* detected sources are more likely to be scintillators than none *Fermi* detected sources, that is, is there a difference in the distributions in the MASIV survey when they are classified based on their gamma-ray properties. To investigate this, the question was approached from the other side, how many scintillating sources are LAT detected compared to non scintillating MASIV sources. Again a flux density cutoff of $S > 0.3$ Jy was imposed.

It was found that 64/146 scintillating MASIV sources are LAT detected, this is 43.8%. Compared to 31/84 NON scintillating MASIV sources, 36.9%.

Statistically it is again not possible to reject the hypothesis that these are the same to a confidence level of 95%. However at a confidence level of 80% the null hypothesis is rejected, that is, to 80% confidence, scintillating sources in MASIV are more likely to be LAT detected than their non scintillating counterparts. Again, this is not unexpected, the compact natures of most gamma-ray associated radio sources lend themselves well to the requirements of scintillation. It is worth noting that the analysis may be skewed somewhat due to several biases in the data. The MASIV survey was targeted toward flat spectrum, compact radio AGN, and the source matching performed as part of the 2FGL catalogue preferentially matches gamma-ray detected sources with flat spectrum, compact radio sources. A less targetted scintillation catalogue would make for a much better analaysis, as in this case the distribution of sources in both the MASIV catalogue, and the radio associations in 2FGL likely stem from the same population. It is likely that if a broader survey was used, a more well defined correlation between scintillators and *Fermi*-LAT associated sources would be found.

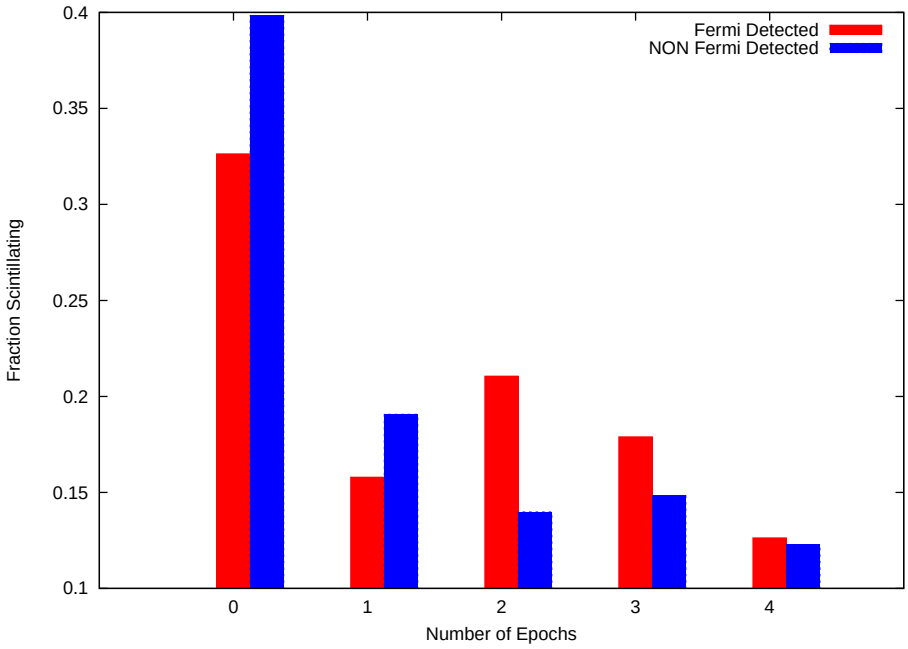

Figure 3.1 The fraction of sources scintillating in no, one, two, three and four epochs for both the *Fermi*-LAT detected sources in MASIV (Red) and the none *Fermi*-LAT detected MASIV sources (Blue).

3.3 Scintillation per epoch

The MASIV survey studied each source for four epochs, allowing a more detailed comparison between the *Fermi* associated sources and the MASIV catalogue in general to be performed. It might be expected that scources which scintillate in more epochs, and thus are more consistent scintillators, are more likely to be active gamma-ray sources, assuming a link between new component generation and both gamma-ray flaring and scintillation. In effect, sources which only show scintillation on one epoch may not be compact, and thus are actually unlikely to be gamma-ray detected as no new component evolution has occurred. A histogram of the fraction of sources scintillating in one or more, two or more, three or more and four epochs for both the *Fermi*-LAT detected sources and the non LAT detected sources is shown in Figure 3.1. Note the large fraction of *Fermi* detected sources that show no evidence of scintillation at all, and yet the larger fraction of *Fermi* detected sources compared with non *Fermi* detected sources found to scintillate in just one epoch. Sources scintillating in 2, 3, or 4 epochs are each more likely to be *Fermi* detected. Individually the only statistically significant difference is the fraction of *Fermi* detected sources scintillating in 2 epochs, at a confidence level of 80%. However that *Fermi* detected sources appear to be more likely to scintillate in 2 epochs or more further strengthens the tentative finding that LAT detected radio sources are more likely to be scintillating sources.

3.4 Long term Radio Variability Related to Gamma-Ray Flux Density

To investigate the possible relation between long term radio variability and the presence (or lack thereof) of gamma-ray emission an analysis of the maximum change in radio flux density (over the four epochs) vs the average radio flux density of all the sources was made (see Figure 3.2).

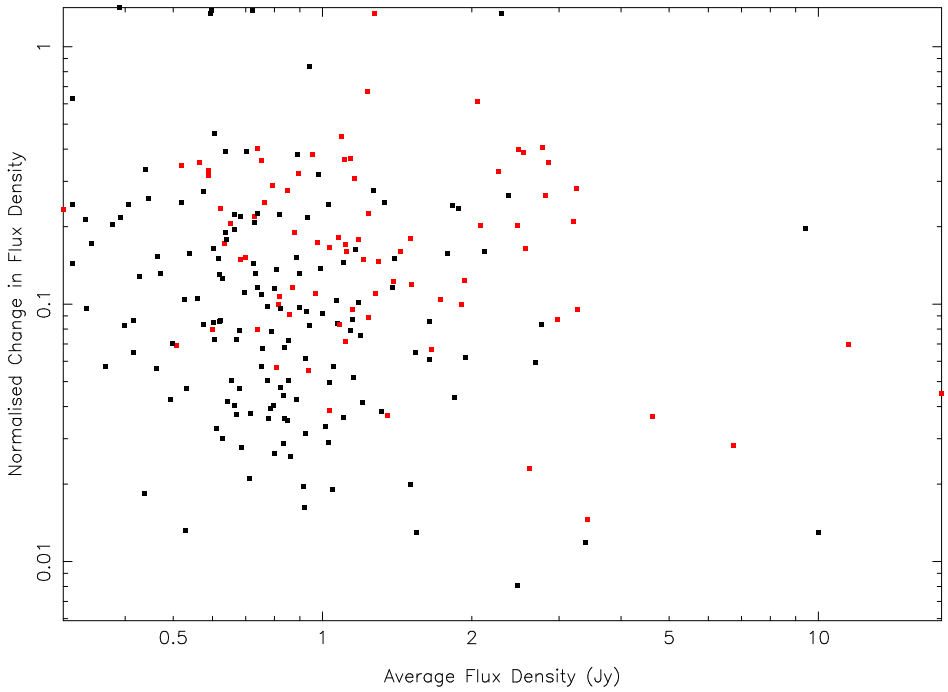

Figure 3.2 Maximum change in flux density over the four MASIV epochs (normalised against flux density) vs the flux density of the source. Red sources are *Fermi* detected, black are not.

Again using a flux density cutoff of $S > 0.3$ Jy, these points were then binned to see if *Fermi* sources do indeed have a tendency to be more variable. This is suggested by Figure 3.2 although a t-test does not show a significant difference between the mean change in flux density for *Fermi* and non *Fermi* detected sources. Figure 3.3 does show that *Fermi* associated sources (red) do seem to be slightly more variable than non *Fermi* sources (black), as evidenced by the extension of the distribution to the right of the plot. A statistically significant difference in the skew of the two histograms is found at the 95% confidence interval, that is, the histogram for the *Fermi* detected sources has a significantly longer tail to the right (increasing normalised change in flux density). Since most *Fermi* sources are not continuously detected but rather show flaring behaviour, often brightening by factors of 2 or more (see Chapter 7 for some examples of gamma-ray light curves), this finding could suggest a correlation between gamma-ray and radio flaring. At the least it shows that a source capable of generating the large energies required to produce gamma-ray emission tends to be quite variable even at wavelengths far removed from the gamma-ray regime. Figure 3.2 also

suggests a higher average flux density for *Fermi* detected sources, as compared with their non-*Fermi* detected counterparts. This is perhaps not surprising, as *Fermi* detected sources are naturally highly energetic, as well as variable, and thus more likely to produce new radio components. This does not affect the variability analysis performed here as a normalisation to average flux is performed.

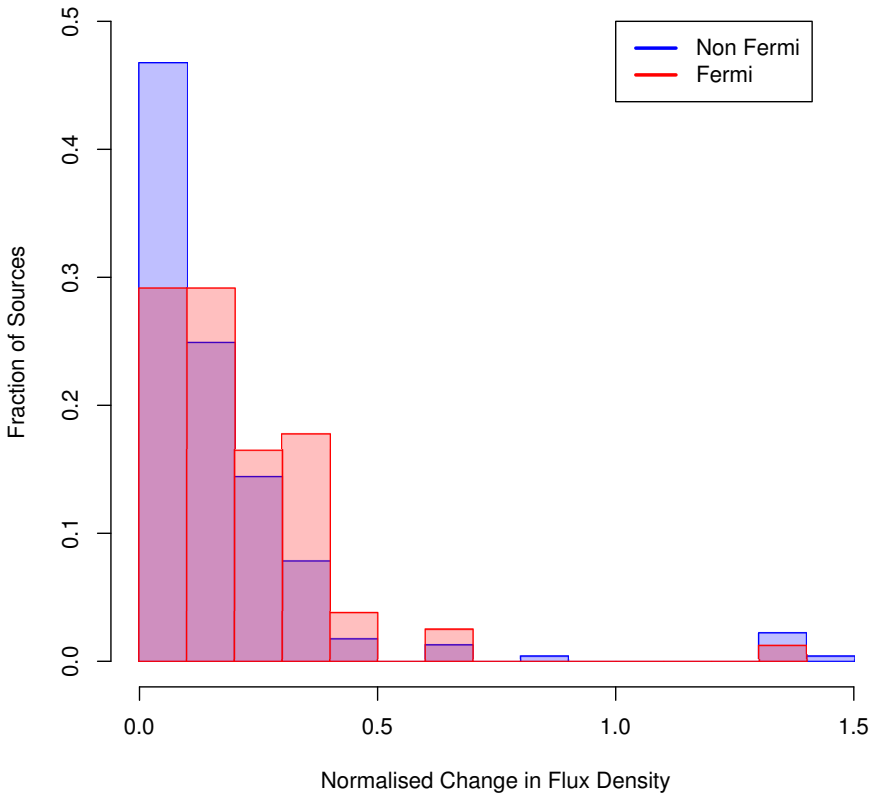

Figure 3.3 Histogram of fraction of sources vs normalised maximum change in flux density for *Fermi* associated sources (Red) and non *Fermi* associated sources (Blue).

3.5 Long term variability of scintillating sources

Finally the analysis outlined in the previous section was repeated, but the difference between scintillating sources in the MASIV survey and non scintillating sources was explored. In this case the difference in the mean change in normalised flux density between scintillating and non scintillating sources was found to be statistically significant at a confidence level of 90%, with scintillating sources having higher mean changes in normalised flux density. A histogram of the results is shown in Figure 3.4. Scintillating sources do seem to be more likely to show long term flux density variability, as shown by the difference in the means,

as well as a statistically significant (95% confidence) higher skew towards higher change in normalised flux density for scintillating sources. This might be due to their more compact natures. Compact sources will show variability on shorter timescales than more extended sources. As such, the sources that do not show variability over the course of the MASIV monitoring program may merely be evolving (in flux density) at a much slower rate, being more extended in nature.

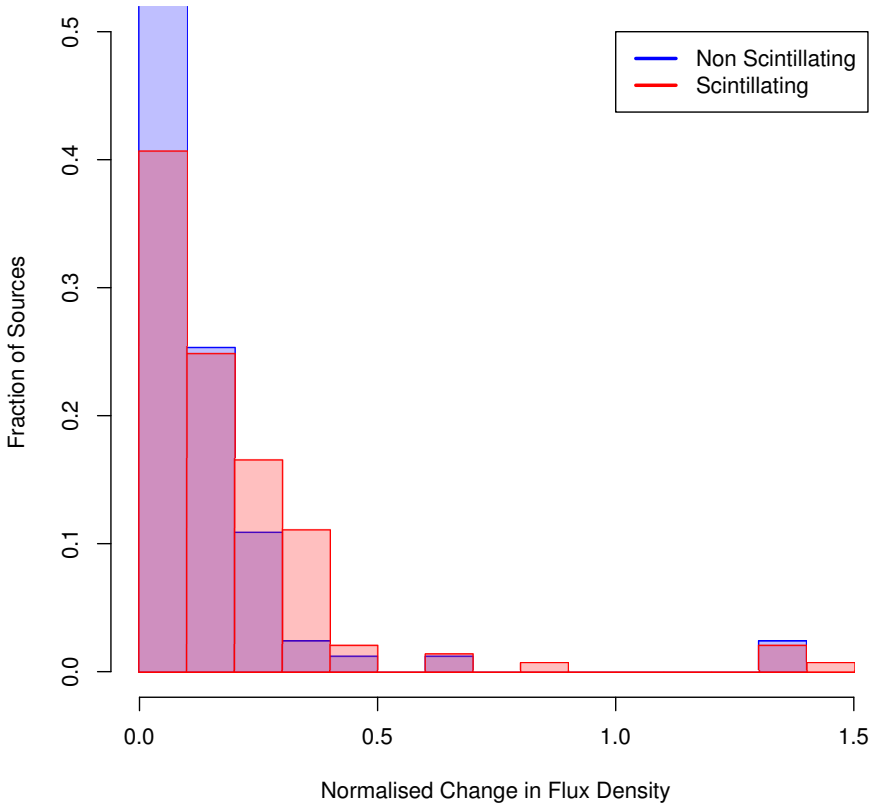

Figure 3.4 Histogram of fraction of sources vs normalised maximum change in flux density for scintillating MASIV sources (Red) and non scintillating MASIV sources (Black).

3.6 Summary

There is tentative, but consistent evidence that bright, flat spectrum, compact radio sources that scintillate are also likely to be gamma-ray detected. The significance of the connection increases if a source is a consistent scintillator, which physically suggests a dynamic source with a consistently compact component near the core likely showing both strong scintillation and associated gamma-ray emission.

Bright, compact, flat spectrum radio sources that are *Fermi* detected show more intrinsic flux density variation (at radio frequencies) than their non *Fermi* detected counterparts. Sources that show evidence of scintillation in the MASIV survey also tend to produce greater intrinsic flux density variations than non scintillating sources. Scintillation is a useful indicator of microarcsecond structure and could help provide insight into the physical processes taking place during, and/or preceding, a gamma-ray flare. In order to fully investigate a causal link between scintillation and flaring behaviour, individual sources showing multi-wavelength flaring as well as consistent scintillation need to be studied on long time scales. One such candidate source is PKS 1622−253, which shows consistent scintillation, increasing in magnitude during radio flares, as well as multiple flares occuring at radio to gamma-ray frequencies (see Figure 7.13 in Chapter 7) and is the subject of future work beyond the scope of this thesis.

Chapter 4

VLBI and Modelfitting

In this chapter VLBI data on PKS 0208−512 are presented, including modelfitting and a calculation of apparent jet speed. Modelfitting allows the calculation of core brightness temperatures and kinematics. The analysis of the jet speed was undertaken in conjunction with the work presented in Chapter 5, as this allows a calculation of the distance between gamma-ray and radio emission sites.

As described in Section 2.1, the TANAMI project monitors around 50 southern (declination south of -30 degrees) blazar sources at 8.4 and 22 GHz, using the LBA (Ojha et al. 2010), South African, Chilean, Antarctic and New Zealand telescopes. This includes an inital sample of 43 sources, with new sources added based on *Fermi* observations. TANAMI observations occur at a cadence of approximately three months, however the full sample is not observed at every epoch due to scheduling constraints.

4.1 PKS 0208−512 Imaging

PKS 0208−512 has been included in the sample since observing commenced in November 2007, prividing a detailed view of the sources evolution with time, as well as possible emission sites (i.e. knots in the jet) of the gamma-ray radiation. Six epochs of PKS 0208−512 observations have been observed, correlated and calibrated and are presented here. The first in November 2007, and then June 2008, November 2008, September 2009, October 2010 and July 2010. Only the 8.4 GHz observations are presented here, as their sensitivity is greater than their 22 GHz counterparts. The first epoch image is shown in Figure 4.1. The higher frequency images resolve out the jet resulting in too few component detections for jet speed calculations.

Correlation of the first two epochs was performed at the Swinburne University of Technology, with the remaining epochs correlated at Curtin University using the DIFX software correlator (Deller et al. 2007). Calibration was performed in AIPS (Astronomical Image Processing System Greisen 1998) in the standard manner. Residual rate and delay errors are corrected using the task FRING, followed by gain-elevation and system temperature am-

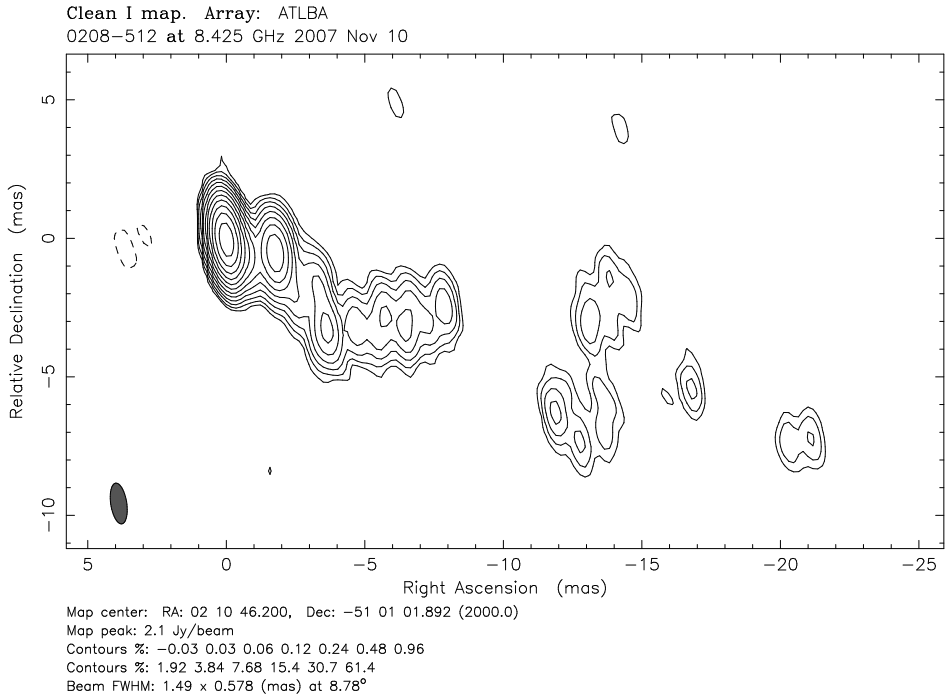

Figure 4.1 The first epoch 8.4 GHz TANAMI image of PKS 0208−512, showing a bent jet extending south-west about 25 mas.

plitude calibration. The imaging program 'Difmap' (Shepherd et al. 1995) is then used to perform hybrid mapping (Readhead et al. 1980) and self-calibration (Pearson and Readhead 1984). The same cell-size and mapsize were used for each epoch for consistency. Both phase and amplitude selfcal were used to create CLEAN maps. The typical u, v coverage is shown in Figure 4.2 and the large gap between short and long spacings reveals the major difficulty in working with these data. The resultant clean images are shown in Figure 4.3. The image scale has been compressed on the y axis to allow for comparison between all epochs. The source shows a one sided jet extending out past 40 milli-arcseconds, and a bend in the jet at roughly 4 mas from the core. Due to each observation having only a subset of antennas available, the beamsize and shape vary between epochs, however the maps are generally consistent, showing a jet extending south-west to about 2 mas and then straightening directly west to 8 mas.

4.2 PKS 0208−512 Modelfitting

The data were modelfit in Difmap, with the cleaned, self-calibrated image used as a template. No further amplitude or phase calibration was applied during the modelfitting. For each epoch the first three model components (including the core and two brightest jet components) of the previous epoch were loaded into difmap, and a chi-squared minimisation was performed before additional model components were added as needed. This was done in an attempt to identify component motion and hence measure a jet speed. Only circular gaussian components

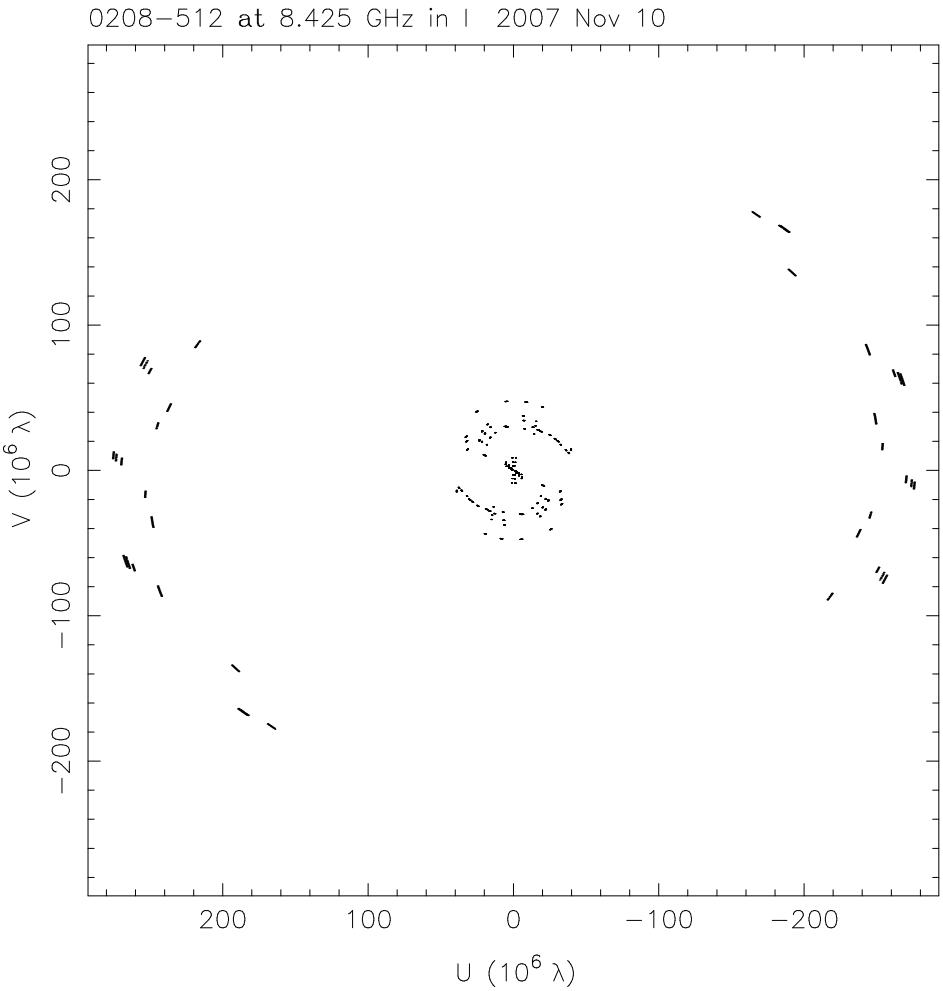

Figure 4.2 Typical u, v coverage of the PKS 0208−512 VLBI observations, note the large gap between the long baselines, and the short Australian baselines.

were used, although they were allowed to collapse to points. Elliptical components were not employed in the modelfitting in order to keep components as consistent as possible between epochs, it was found that elliptical components would collapse to linear ones in most epochs. The results are shown in Figure 4.4. The number of components required for a good fit to the u-v data is strongly dependent on the noise level of the image, making it difficult to identify the same component in each epoch. The component distance from the core is plotted in Figure 4.5. Components were cross matched based on position, flux density and semi major axis. Errors have been approximated by using DIFWRAP (Lovell 2000) to calculate the error in component position for the second component from the core in each epoch, and using that error as representative of the errors for that epoch. Three trendlines were fit to these data, for the first, second and fourth component from the core (in general, some epochs contain a further component, or are lacking one) with slopes of 0.221, 0.414 and 0.449 mas per year respectively, giving an average of 0.361 ± 0.057 mas per year.

Due to the difficulty in cross matching components, and the over resolved nature of

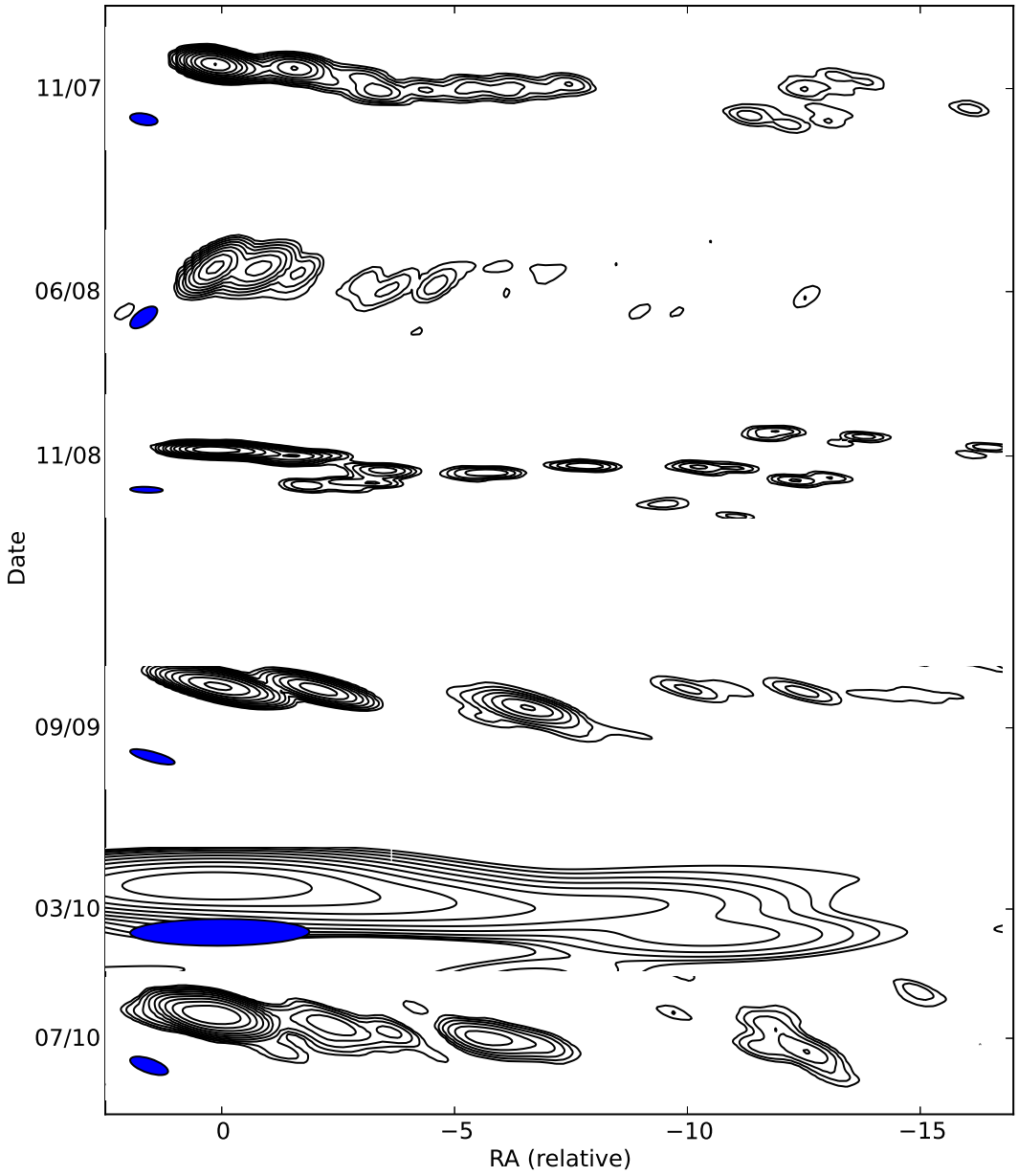

Figure 4.3 Clean maps of PKS 0208−512 at 8.4 GHz, for the six observed epochs, arranged by observation date (y-axis). The beam is shown filled bottom left. Note the general agreement in source structure but relatively poor localisation of individual components, the jet is overresolved resulting in a large number of small components making cross matching between epochs difficult. The y axis on each epoch is compressed from the original (Figure 4.1) to allow all epochs to be presented and compared.

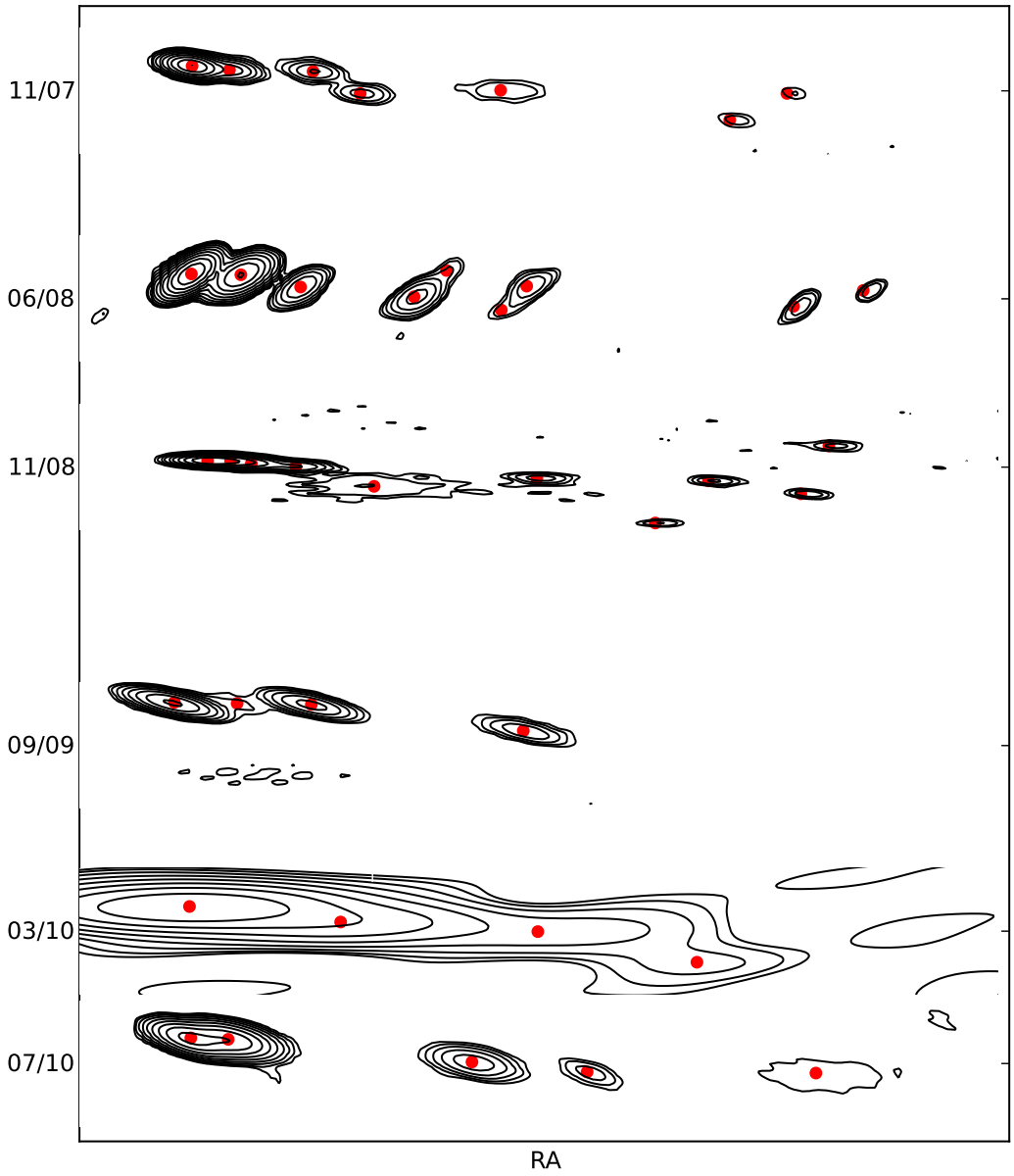

Figure 4.4 Modelfitting of PKS 0208−512 at 8.4 GHz, for the six observed epochs, arranged by observation date (y-axis). The red points indicate component position. Note that the y-scale has been changed slightly in this Figure compared with Figure 4.3, to produce a cleaner looking plot.

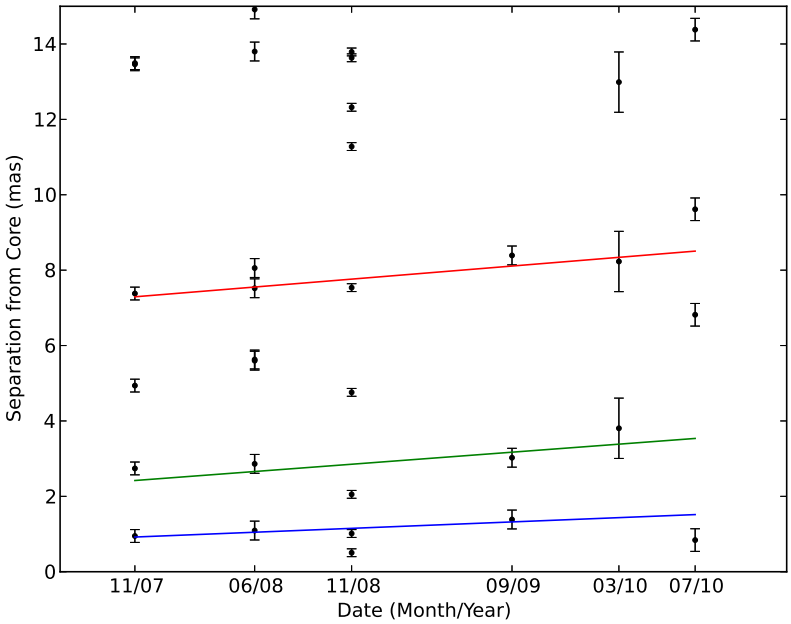

Figure 4.5 Distance from the core (first fitted component) in degrees, for the components shown in Figure 4.4. Trend lines have been fitted for those components that could be cross-matched and were detected in at least 5 epochs. Errors in the component composition were calculated for the second component out from the core using DIFWRAP and used as representative of the errors for each component in that epoch.

components in the jet in general, each epoch was reimaged and modelfit using the Australian baselines only. Imaging was based on the clean images using the full array of telescopes, flagging the long baselines and starting a fresh CLEAN component map. No new amplitude calibration was applied, however phase calibration was used. Modelfitting was then performed as described above. The larger beamsize forms a jet without as many isolated components, which can gravitate towards local chi-squared minima and then be reinforced by amplitude self-calibration. The resultant model fits are shown in Figure 4.6. It is much easier to see the evolution of the model components in this figure and thus to identify which to fit to. The distance of each of the components from the core vs the epoch is plotted in Figure 4.7. The lines fitted through the first, second and third components have slopes of 0.417, 0.347 and 0.284 mas per year respectively, giving an average of 0.349 ± 0.063 mas per year. This agrees well with that found from the full TANAMI array modelfitting. The fourth slope fit to the furthest out components has a slope statistically indistinguishable from zero. Either those components have slowed due to interaction with the surrounding medium and gravitational effects of the AGN, or their localisation is too poor for a good fit to be found. These data could also point to a standing shock in the jet.

When the new slopes and those found previously are averaged a slope of 0.355 ± 0.033 mas

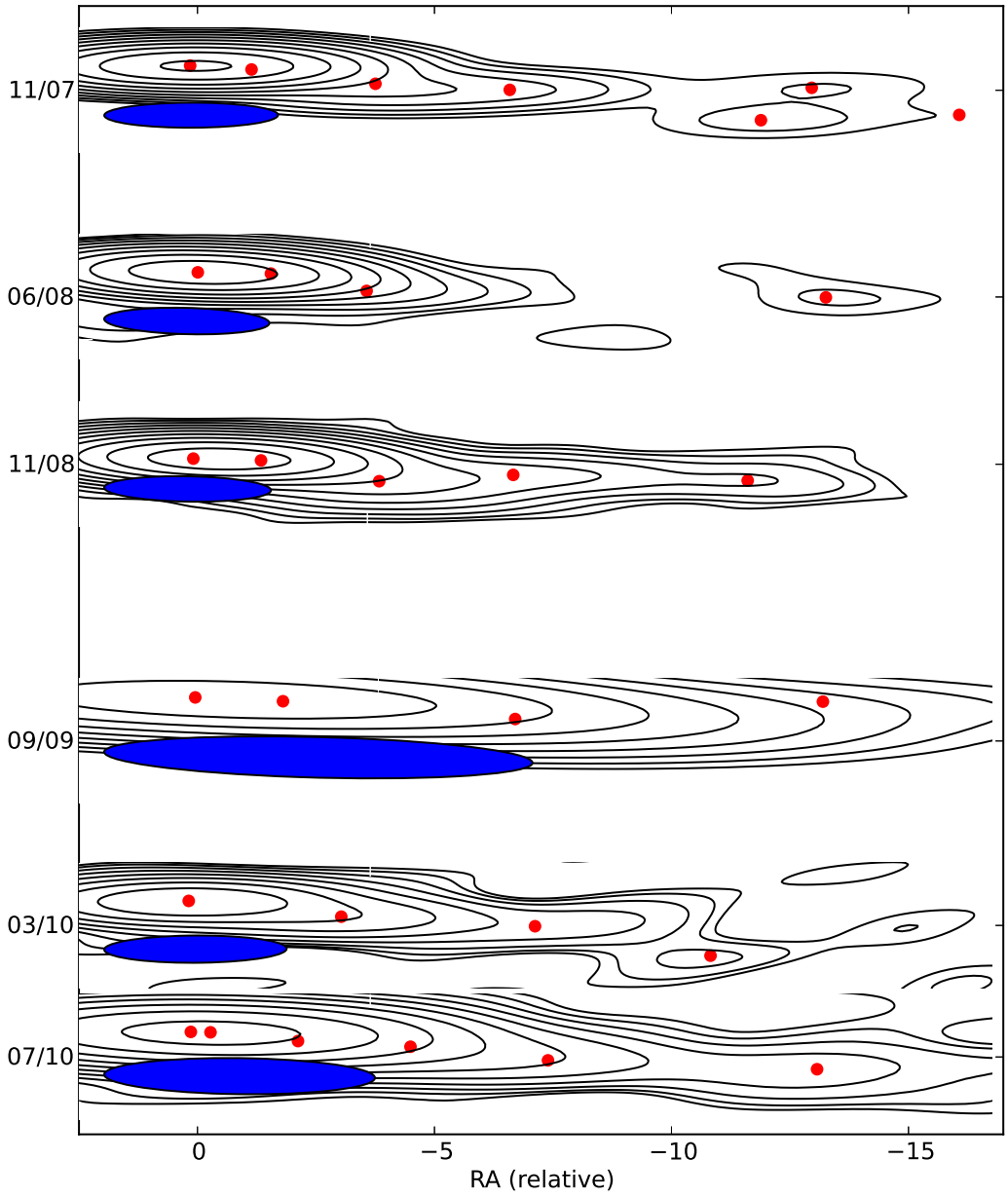

Figure 4.6 Modelfitting of the Australian baselines of the six epochs of PKS 0208−512 observed at 8.4 GHz as part of the TANAMI project. The red points indicate component position. Again, DIFWRAP was used to estimate the error of one component per epoch, and this error used for the whole epoch.

Table 4.1. Fluxes and Brightness Temperatures of the Core

Epoch	Core Flux (Jy)	$T_B(K)$
2007-11-11	2.1	1.5×10^9
2008-06-09	1.7	2.4×10^8
2008-11-27	1.2	2.1×10^8
2009-09-05	0.98	1.7×10^9
2010-03-12	0.98	1.7×10^9
2010-07-24	0.98	1.7×10^9

per year is found. PKS 0208−512 is at a redshift of 0.999 (Wisotzki et al. 2000). Assuming lambda CDM cosmology, this gives a scale of 8.041 kpc/" and thus an apparent jet speed of 9.3 ± 0.86 c.

The apparent jet speed is given by:

$$v_{app} = \frac{v \sin(\theta)}{1 - \beta \cos(\theta)} \tag{4.1}$$

So for $v_{app} = 9.3$ and $v \to c$, this gives $\theta < 12.27$ degrees. That is, the jet must lie within 12.27 degrees to the line of sight.

Table 4.1 lists the brightness temperatures and flux density of the core for the Australian baseline only modelfitting.

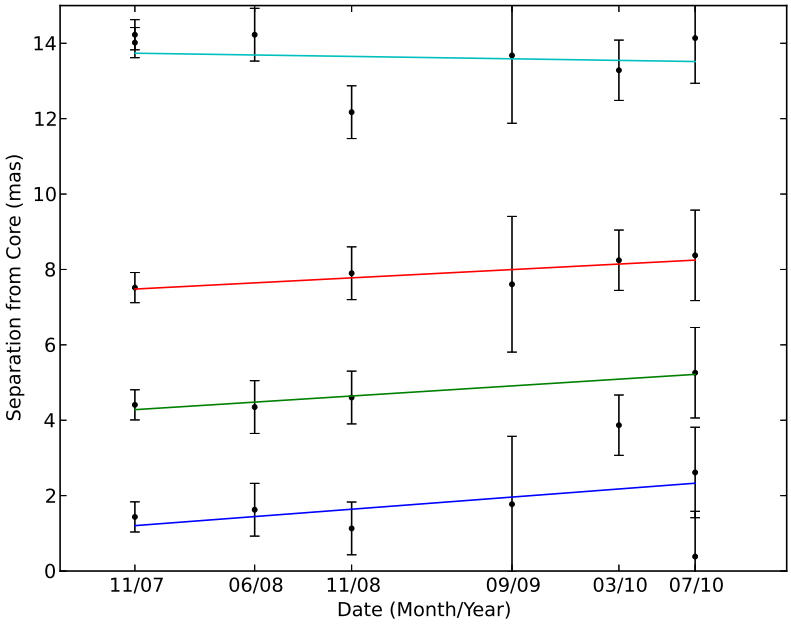

Figure 4.7 Distance from the core (first fitted component) in mas, for the components shown in Figure 4.6. Trend lines have been fitted for those components that could be cross-matched and were detected in at least 5 epochs.Note that the first component in the March 2010 epoch has been ignored. This is justified as in this particular epoch one large component encompasses the region occupied by (for example) the second and third component in the July 2010 epoch. The significantly higher noise in the image is thought to account for this, and is due to a less complete hour angle coverage.

Chapter 5

PKS 0208−512 Time Domain Analysis

PKS 0208−512 has been a part of several monitoring projects at varying frequencies and cadences throughout the spectrum. We present those data here, together with a description of a time domain analysis designed to study the relationship between flaring events observed at different wavelengths and the implications on source morphology and locations of emission.

The radio data, covering 1.4 GHz to 230 GHz obtained using the Australia Telescope Compact Array (ATCA), the Ceduna single dish, and the Atacama Pathfinder Experiment (APEX). The Small and Moderate Aperture Research Telescope System (SMARTS) provided both optical and near infrared data, which is complimented by the Swift UV and optical instrument (Swift-UVOT), and the Rapid Eye Mount (REM) optical telescope. X-ray light curves were generated from Swift X-ray Telescope (Swift-XRT) data, and the *Fermi* satellite provided the gamma-ray lightcurves.

5.1 Australia Telescope Compact Array Light Curves

As part of the TANAMI program (Ojha et al. 2010), a multi frequency flux density monitoring program of southern hermisphere AGN using the ATCA was initated in November 2007. The sample was selected from known gamma-ray AGN detected by EGRET and has grown since then to include AGN detected by *Fermi*. This monitoring program observes at frequencies between 4.1 and 90 GHz at a cadence of roughly six weeks. The data on PKS 0208–512 are further enhanced by making use of the ATCA calibrator database (Stevens et al. 2012). As PKS 0208–512 is bright, $\sim$ 2 Jy, and compact on ATCA baselines, it is often used as a bandpass calibrator. Calibrator observations are automatically added to said database and allow us to both increase the time sampling of the PKS 0208–512 lightcurve and the frequency coverage down to 1.4 GHz.

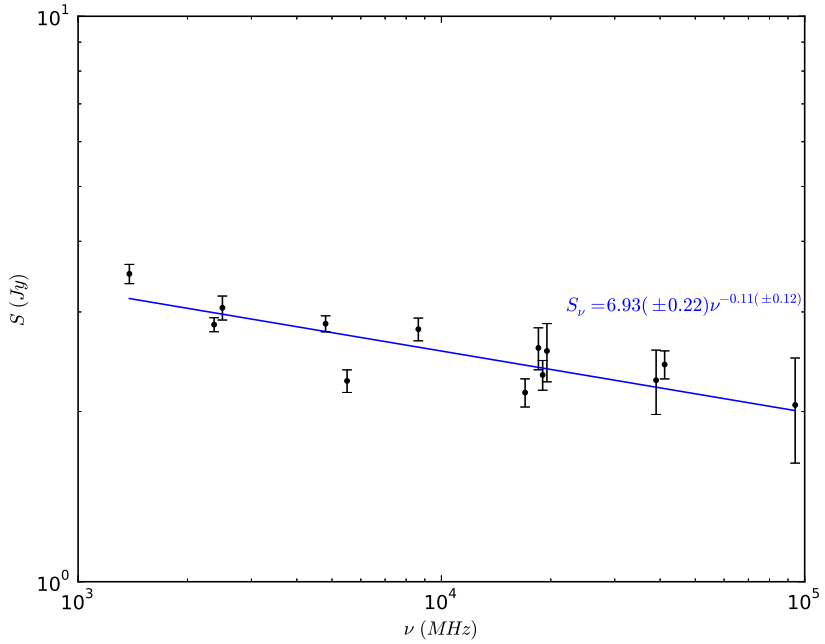

Figure 5.1 Radio spectrum of PKS 0208–512. Note the slope consistent with zero (within errors).

5.1.1 Radio Spectral Shape

PKS 0208–512 is a very flat spectrum source with $S_\nu = 6.93(\pm 0.22)\nu^{-0.11(\pm 0.12)}$ (Figure 5.1). The spectrum was calculated from the ATCA and Ceduna multifrequency data, during a non-flaring section of the light-curve averaged over 300 days in 2010. The resultant spectrum has a slope consistent with zero, it is not possible to within 95% confidence to reject the null hypothesis that the slope is equal to zero. It is worth noting that it is possible to reject said hypothesis with a confidence level of 90 % (less than 2 sigma).

In order to minimise time gaps in the ATCA lightcurves, and taking into account the flat spectrum of the source, the data were binned to produce lightcurves for frequencies at 1.4 and 2.4 GHz, and between 4.8 and 5.5 GHz, 8.6 and 9.0 GHz, 17 and 24 GHz, 33 to 45 GHz and 88 to 96 GHz. These lightcurves are presented in Figure 5.2. No correction for spectral index was applied within each bin, as the spectrum is so flat uncertainties in the flux density measurements greatly exceed those introduced by the lack of spectral index correction.

5.2 Ceduna Single Dish Light Curves

The Ceduna antenna is a radio telescope with a 30 m diameter main reflector, located at Ceduna in South Australia, and is operated by the University of Tasmania. Ceduna is a repurposed Telstra Satellite Earth Station, which now forms an integral part of the Australian

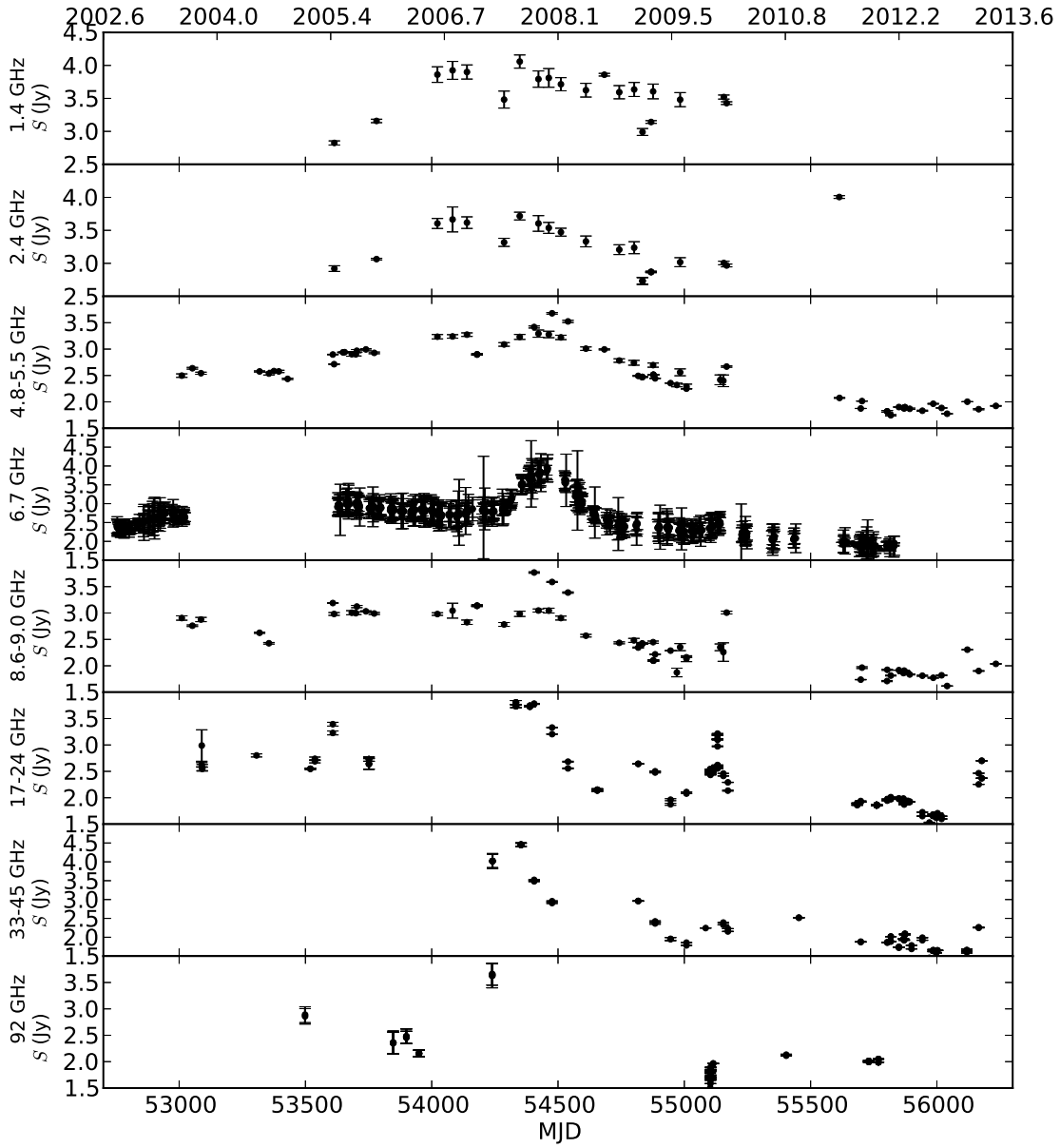

Figure 5.2 ATCA Monitoring of PKS 0208–512 at frequencies between 1.4 and 96 GHz. Note the tentative suggestion that the source is flaring at high frequencies earlier than at low frequencies.

Long Baseline Array (LBA) after its conversion to astronomical use in 1995. The telescope monitors a subsample of approximately 50 *Fermi* detected AGN at a two week cadence, as well as twelve sources at a nearly daily cadence. PKS 0208–512 is one of these frequently monitored sources, although bad weather and technical problems have created some large time gaps, which can affect the time domain analysis as discussed in Section 5.9. Ceduna uses a standard alt-azimuth mount, with a slew rate of 40 degrees per minute on each axis, and has an elevation limit of 10 degrees. Part of its monitoring program is dedicated in support of TANAMI, but the majority of monitoring is of Intra Day Variable (IDV) sources as part of the COSMIC project, which has monitored two groups of strong scintillators since 2003 (McCulloch et al. 2005). These data were used by Senkbeil et al. (2008) to investigate extreme scattering events and by Carter et al. (2009) who detected an annual cycle in the variability time-scale of the radio emission from PKS 1622–253 and PKS 1519–273. Ceduna is capable of observations at 1.4, 2.2, 4.8, 6.7, 8.4, 12.2 and 22 GHz using room temperature receivers. However as the variability of scintillating sources is expected to peak at around 6.7 GHz, and receiver changes at Ceduna are not automated all monitoring discussed here was carried out at 6.7 GHz.

5.2.1 Data Reduction

Ceduna has been monitoring a core group of around twelve AGN since early 2003, however the data reduction software was not fully completed at the start of this project, and was extremely inefficient as well as prone to frequent crashing. There was a large backlog of data to be reduced at the start of this project, so the decision was made to re-write what code did exist into C, to improve speed, efficiency and reliability. Sources are automatically selected by the observing software based on elevation and time since the last observation. The source list file contains both target sources and the calibrators used. Ceduna observes in four scan blocks, two in Right Ascension and two in Declination. Scans are then saved in the FITS file format, with one file being generated per day.

These FITS files then require splitting into individual sources and calibration. This is a multi step process. Each four scan block is treated individually. Scans are first normalised to a noise diode, and then fitted with a Gaussian and a polynomial baseline. The two RA and DEC scans are averaged together in amplitude, respectively, and cross-checked for consistency. If, for example, two RA scans do not match to within 10% the entire block is discarded. Pointing corrections are then applied based on the offset of the source from the beam centre in the orthogonal scan. The averaged RA and DEC scans are then combined. Finally a gain elevation correction is made based on a gain curve calculated from one year of observations of PKS 1934–638, one of our calibrator sources which is known to be flux density stable Reynolds 1994, (3.9383 Jy at 6.7 GHz, Reynolds 1994), and saved as a text file per source.

These data are then calibrated using either PKS 1934–638 or 3C227 (assumed flux density

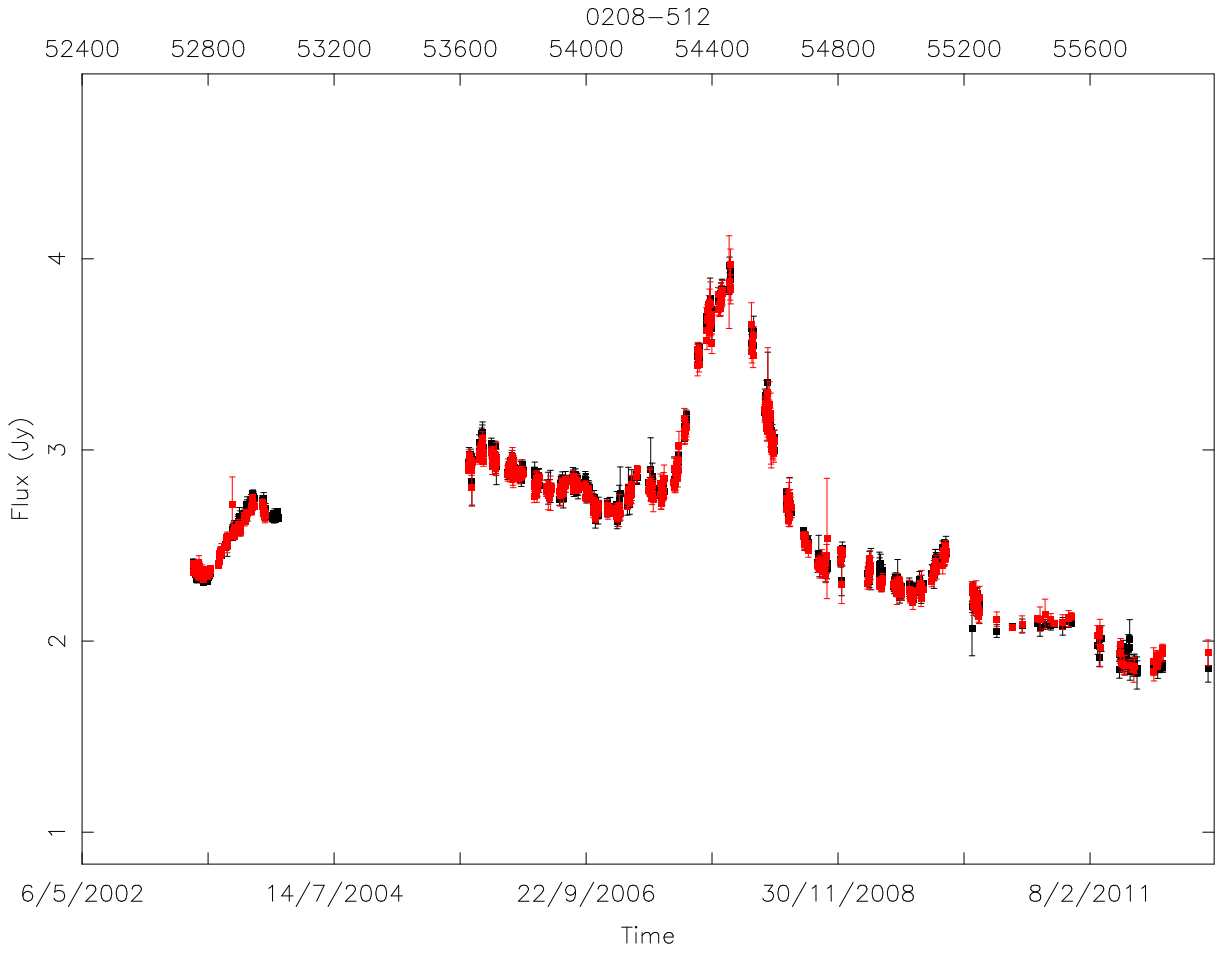

Figure 5.3 Ceduna single dish 6.7 GHz lightcurve of PKS 0208–512. The black points are RCP and the red are LCP.

1.9885 Jy), depending on their location in the sky, and averaged into one day bins. The resultant lightcurve for PKS 0208–512 can be seen in Figure 5.3.

5.3 APEX

The ATACAMA Pathfinder Experiment (APEX) is located in the ATACAMA desert in northern Chile, and uses a prototype Atacama Large Millimeter Array (ALMA) antenna at sub-millimetre wavelengths (Güsten et al. 2006). A sample of around 40 gamma-ray blazars has been monitored since 2007/2008 at 345 GHz. This is the first systematic, long term blazar monitoring campaign at sub-mm wavelengths. APEX monitors PKS 0208–512 and the resultant light-curve is shown in Figure 5.4. This lightcurve has been provided by the APEX team using their standard reduction methods (Güsten et al. 2006).

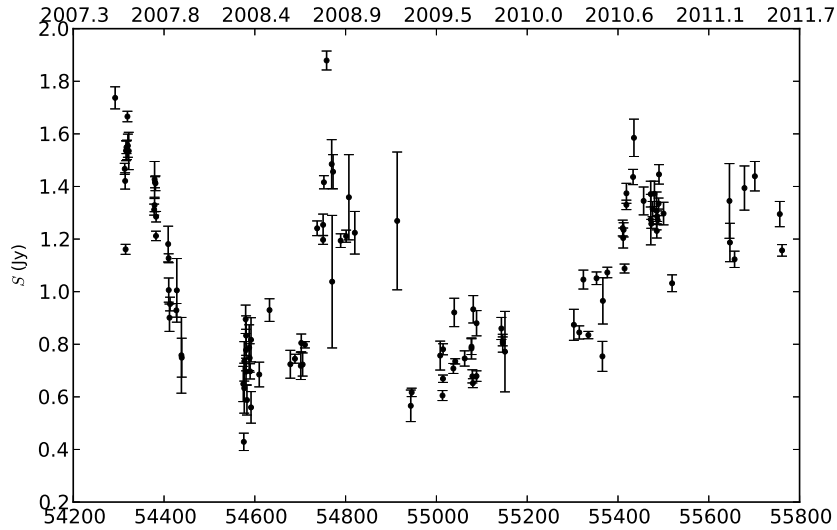

Figure 5.4 APEX 345 GHz monitoring of PKS 0208–512.

5.4 Small and Moderate Aperture Research Telescope System

The Small and Moderate Aperture Research Telescope System (SMARTS) is a collection of four small optical telescopes located on Cerro Tololo and operated by the SMARTS consortium (a consortium of Universities). A monitoring program for *Fermi* detected AGN has been set up (Bonning et al. 2012) using around 700 hours of telescope time per year on three of those telescopes. The majority of monitoring is done daily on a 1.3 m telescope, feeding into an optical CCD and a infrared imager simultaneously. This provides good quality monitoring data at multiple frequencies in the optical/near-infrared regime, which is particularly interesting as this may be near the crossover between synchrotron and thermal emission in PKS 0208–512; see Chapter 6.

The light curves of PKS 0208–512 generated from this monitoring are shown in Figure 5.5. These lightcurves are publicly available and have been taken directly from the Yale Fermi/SMARTs project (Yale-Fermi/Smarts 2013). Some suspect data points were removed from the lightcurve under consultation with the Yale Fermi/SMARTs team.

smarts

Figure 5.5 SMARTS optical and near-infrared monitoring of PKS 0208–512. Top axis is decimal year.

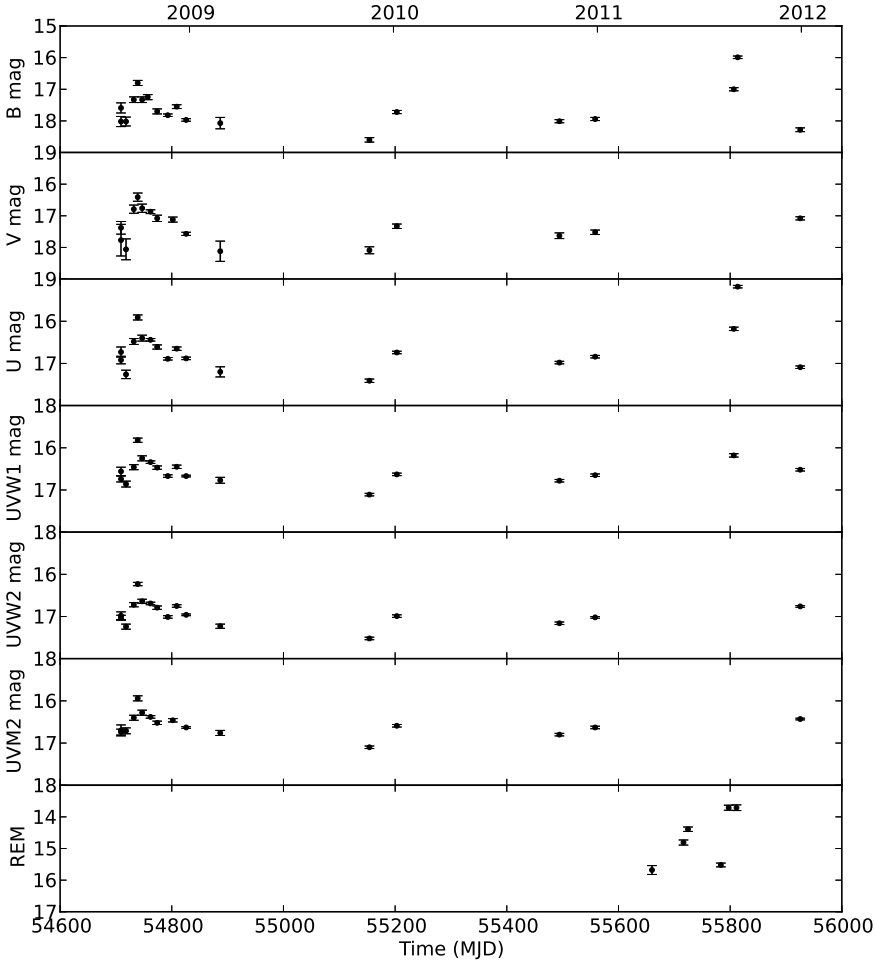

Figure 5.6 Swift-UVOT monitoring of PKS 0208–512 at various optical and ultraviolet bands, as well as some higher cadence REM observations over the course of a bright optical flare (bottom panel).

5.5 Swift-UVOT

The UV/Optical Telescope (UVOT) is a 30 cm modified Ritchey-Chretien, co-aligned with Swift's X-ray telescope (XRT). UVOT can provide simultaneous ultraviolet and optical coverage between 170 and 650 nm in a 17 by 17 arcminute field of view. UVOT is mostly used to study optical/UV afterglows of gamma-ray bursters, but in this case makes an excellent addition to the multifrequency monitoring of PKS 0208–512.

The nature of SWIFT however means that there is no regular cadence to the monitoring, UVOT data is only obtained when the telescope is performing targeted observations of PKS 0208–512. Figure 5.6 shows U,V,UVW1,UVW2, and UVM2 band light curves produced from UVOT data.

5.6 Rapid Eye Mount Telesope

The Rapid Eye Mount (REM) telescope is a 60 cm diamater optical telescope located in the ESO Chilean Observatory. It is designed to be able to react quickly to target of opportunity observations (Chincarini et al. 2003), and was used to provide data over just one particular flaring period of PKS 0208–512. These data were taken in response to flaring observed in support of TANAMI observations, and were reduced as detailed in Nesci et al. (2013). The resulting lightcurve is not long enough for time domain analysis of multiple flares. It is however beneficial when combined with the other optical/infrared/ultraviolet monitoring. The bottom panel of Figure 5.6 shows the benefit of the REM monitoring over the flaring period.

5.7 Swift-XRT

The primary purpose of the Swift X-ray Telescope (XRT) is to study gamma-ray bursts, triggering on detections from the Swift Burst Alert Telescope (BAT) and acquiring data often before the event ends. It can however be used in pointing mode when not observing a GRB and has observed PKS 0208–512 several times over the period of interest. Swift-XRT has two main readout modes of its CCD: Windowed Timing (WT) mode and Photon Counting (PC) mode. WT is a high gain mode designed for high time resolution, at the cost of image resolution. PC mode is a standard frame transfer CCD operation. The data presented here are a combination of both modes of observing.

The Swift-XRT light curve is presented in Figure 5.7

5.8 *Fermi*

Fermi (formerly known as GLAST) was launched in 2008 and is the first dedicated gamma-ray space observatory since The Energetic Gamma Ray Experiment Telescope (EGRET) which ceased operation in 2000. Data used in this project are from the on-board Large Area Telescope (LAT). LAT is an imaging gamma-ray telescope which operates from 20 MeV to approximately 300 GeV. Having a field of view encompassing roughly 20% of the sky, LAT scans the whole sky roughly every three hours. This makes it an excellent instrument for high cadence, broad band, gamma-ray monitoring of AGN.

The LAT light curve presented in Figure 5.8 has been reduced in the standard manner using likelihood analysis (Mattox et al. 1996), and is binned in seven day time intervals. Shorter time binning has also been performed and will be presented in Section 5.11. Upper limits are given when the test statistic (see Mattox et al. (1996) for a full explanation) is below 25, corresponding to an approximately 5σ detection.

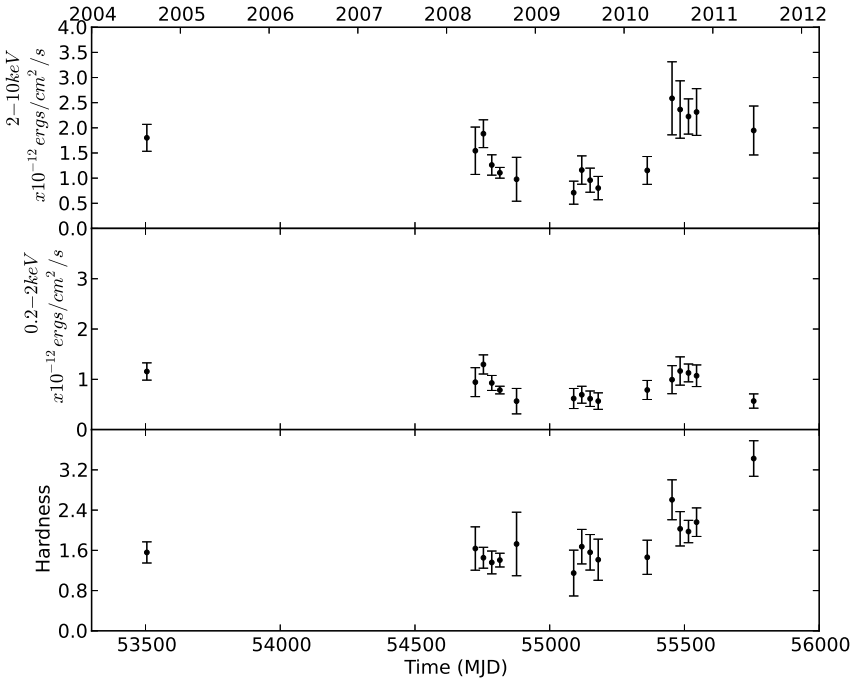

Figure 5.7 Swift-XRT monitoring of PKS 0208–512 at $2-10keV$ and $0.2-2keV$ respectively, as well as the hardness ratio. Note the increase in hardness as the source flares

5.9 Cross Correlation Analysis

Pushkarev et al. (2010) claim the major source of the time delay between radio and gamma-ray flaring is caused by synchrotron opacity in the nuclear region. The critical radius at which the radio core becomes optically thick is given by $r_c \propto \nu^{-1}$ (Blandford and Königl 1979). Therefore (ignoring relativistic effects) if the delay is mostly due to these opacity effects, the time delay between emission seen at a higher frequency ν_h and a lower frequency ν_l should be proportional to $\frac{1}{\nu_h} - \frac{1}{\nu_l}$. In essence, Pushkarev et al. (2010) propose a model in which gamma-rays are free to escape immediately a flare creating perturbation in the jet, whereas said perturbation must propagate along the jet until it reaches some critical radius r_c at which the region becomes optically thin to radio waves. In their analysis of a sample of gamma-ray AGN, they find that the average delay is approximately 1.2 months in the source frame (Figure 1.8).

To investigate this theory in the case of PKS 0208–512 (and for other sources presented in Chapter 7), cross correlation analysis is performed. A variant of the discrete cross correlation function has been used as it allows for good analysis of sample bias, as well as being (relatively) standard in the field, allowing for comparison with previous work. The standard discrete cross correlation function (Edelson and Krolik 1988) has been enhanced in a number of ways in this analysis as follows.

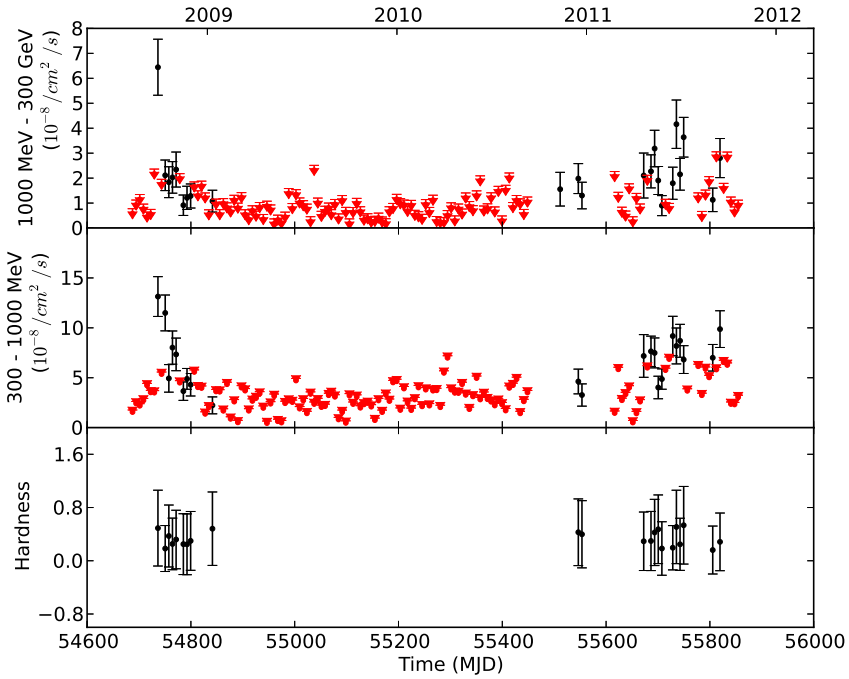

Figure 5.8 *Fermi* monitoring of the gamma-ray blazar PKS 0208–512. These data have been binned in seven day intervals, and cover the energy range from 300 MeV to 300 GeV. Red points are upper limits. Note the constant hardness ratio even during flaring periods.

For all cross correlation analysis the unbinned discrete cross correlation (UDCF) is calculated as given by Edelson and Krolik (1988),

$$UDCF_{ij} = \frac{(a_i - \bar{a})(b_j - \bar{b})}{\sqrt{(\sigma_a^2 - e_a^2)(\sigma_b^2 - e_b^2)}} \tag{5.1}$$

where (a_i, b_j) are all measured pairs, e_f is the measurement error associated with data set f, and σ_f is the standard error of set f.

The UDCF is binned adaptively, with an equal number of pairs per bin, based on the length of the lightcurves being correlated. A correction to the normalisation of the UDCF was made as discussed in White and Peterson (1994). The discrete cross correlation function assumes that the lightcurve being analysed is statistically stationary. That is, that the mean, and variance remain constant with time. As can be seen in any of the lightcurves presented in this chapter, this is not the case for PKS 0208–512. To correct for this, we calculate the mean and standard deviation for each bin separately, and use these to normalise the binned discrete correlation function.

A similar analysis to that presented in Chatterjee et al. (2008) was performed to test for significance of the peak correlation as follows. The power spectrum of each lightcurve is calculated, following Uttley et al. (2002). The light curve is then normalised to the mean

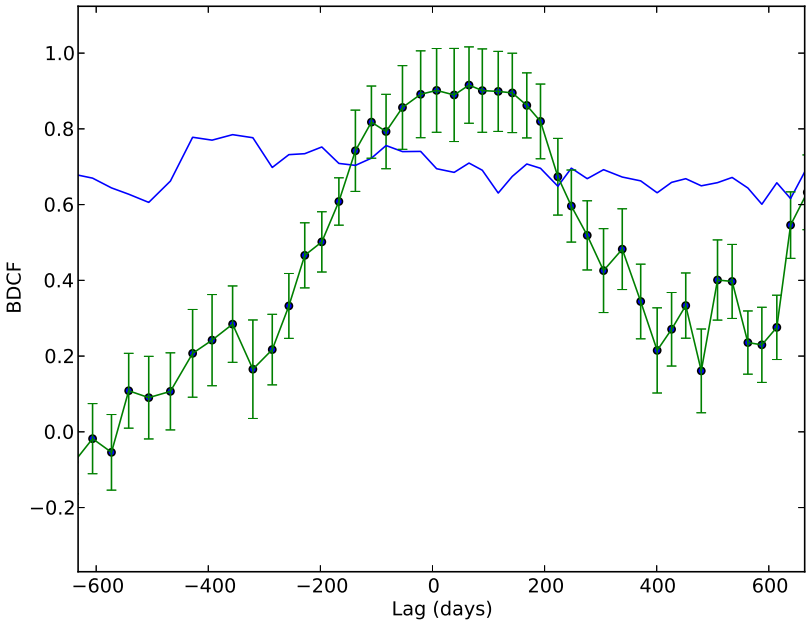

Figure 5.9 Example correlation between 6.7 GHz Ceduna data and 5.5 GHz ATCA data. The (roughly) horizontal line is the three sigma limit for correlations generated from simulated light curves with the same power spectra and time sampling as the original light curves. A peak is considered significant if it (and associated errors) lie above this line. In this case a lag of 46.7 ± 19 days is found.

flux density, and the modulus squared of the discrete Fourier transform is calculated at each sampled frequency $\nu = \nu_{min}, 2\nu_{min}, 3\nu_{min}, ..., \nu_{Nyq}$, where ν_{Nyq} is the Nyquist frequency and $\nu_{min} = T^{-1}$ for total light curve length T.

$$|F_N(\nu)|^2 = \left[\sum_{i=1}^{N} f(t_i) cos(2\pi\nu t_i)\right]^2 + \left[\sum_{i=1}^{N} f(t_i) sin(2\pi\nu t_i)\right]^2 \tag{5.2}$$

The power spectrum is then calculated by normalising by:

$$P(\nu) = \frac{2T}{\mu^2 N^2} |F_N(\nu)|^2 \tag{5.3}$$

and fit with a simple power law model $S(\nu) \propto \nu^{\alpha}$ with flux density $S(\nu)$ and spectral index α.

Following Timmer and Koenig (1995), simulated light curves with the same power spectrum are generated by taking two randomly generated numbers, multiplying them by $\sqrt{0.5S(\nu)}$ and using the result as the real and imaginary part of the Fourier transform of the required simulated lightcurve (for more detail see Timmer and Koenig (1995)). 100 of these light curves are generated for each of the pairs to be correlated, and given the same length and

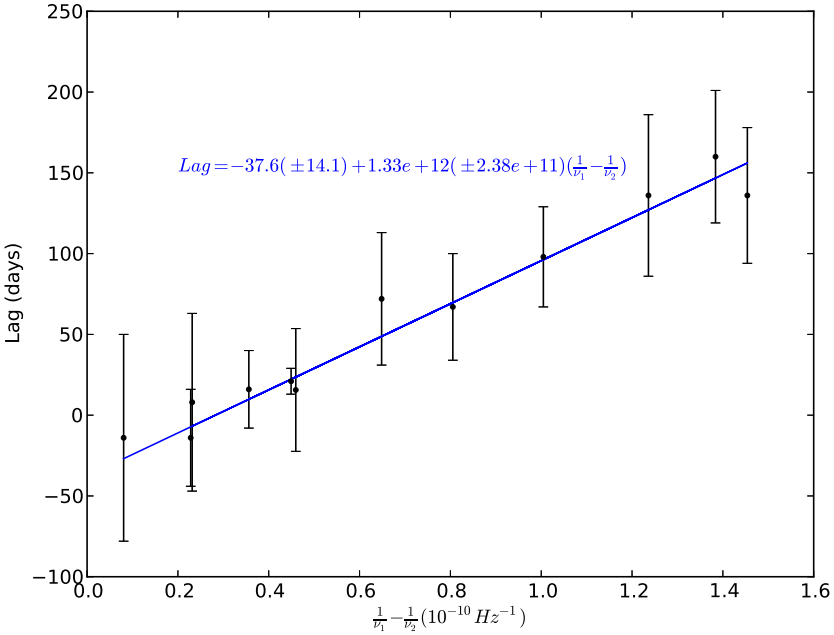

Figure 5.10 The resultant lag measured between radio frequencies, against the change in ν^{-1}. There is a non zero slope in the best fit function, indicating an increase in time lag with increasing change in ν^{-1}. We plot here $\frac{1}{\nu_l} - \frac{1}{\nu_h}$ to give a non negative lag (higher frequencies are leading lower frequencies in the binned DCF).

time sampling as the original light curve. These pairs are then cross correlated as described above, and the unbinned discrete correlation is calculated for each pair, and binned using the same bins as the original pair. The standard deviation of the correlations in each bin are then calculated, and the peak correlation of the original pair of lightcurves is considered to be significant only if it (and associated errors) lie above three times that standard deviation. This ensures a correlation is not due only to time gaps in the light curves. An example of a resultant cross correlation analysis is shown in Figure 5.9.

A significant peak is then fit with a Gaussian above a baseline, and the position of the peak of the fitted Gaussian is used to determine the associated lag between the two light curves being analysed. Errors in the lag term are calculated based on the diagonal components of the covariance matrix of the fitted model, and are slightly more conservative than those produced by the methods outlined in Larsson (2012)

5.10 Radio Cross Correlation

The methodology explained in Section 5.9 (preceding) was applied to each pair of radio lightcurves. The pairs for which a significant peak in the cross correlation function was detected are shown in Figure 5.10. There does appear to be an increase in lag with increase

in $\Delta\nu^{-1}$ consistent with the change in the critical radius of the $\tau \approx 1$ surface. A linear regression gives:

$Lag = -37.6(\pm 14.1) + 1.33 \times 10^{12}(\pm 2.38 \times 10^{11})\Delta\nu^{-1}$, days

showing a non zero slope term.

5.11 Optical - Gamma-Ray

Recent work by Chatterjee et al. (2013) has shown a correlation between optical and gamma-ray wavelengths for this source. This work is part of the SMARTS monitoring mentioned previously (see Section 5.4). SMARTS uses a 1.3 m telescope located at the Cerro Tololo Inter-American Observatory fitted with a dual-channel imager utilising a dichroic, which allows simultaneous optical CCD and IR imaging. Chatterjee et al. (2013) have analysed the time series shown in Figure 5.5 and their own light curves generated from *Fermi* data. Some of their findings are confirmed here and presented so as to reference them with the other frequency analysis performed in this thesis.

As can be seen in Figure 5.11, PKS 0208–512 has undergone three main optical flaring events since SMARTS monitoring commenced in 2008. Chatterjee et al. (2013) classify these as occuring in the timeranges (1) MJD 54690 - 54856 (August 2008 to January 2009), (2) MJD 55087 - 55233 (September 2009 to February 2010) and (3) MJD 55712 - 55893 (May 2011 to November 2011), henceforth referred to as Flare O1, Flare O2, and Flare O3 respectively. Note however that the gamma-ray data spanning the same time range does not show a flaring event during the second optical flare. This is confirmed by the treatment of the gamma-ray data presented in this thesis, shown in Figure 5.8. The source is not detected at gamma-ray energies at all during the time range of the second optical flare (only upper limits are established). Cross correlation analysis as described in Section 5.9 was applied to each of the flaring periods individually. The results are shown in Figures 5.12 and 5.13, showing a strong correlation with zero lag during the first and third flare, and no correlation during the second flare.

Chatterjee et al. (2013) consider the model wherein gamma-ray emission is produced via the Inverse Compton effect, and the OIR emission is from the synchrotron jet (without differentiating between internal and external seed photons). They present two possible cases wherein the OIR emission may show flaring without a corresponding increase in gamma-ray flux density. In the first case this requires a change in the magnetic field strength or direction, without a change in the number of emitting electrons N_e, or the Doppler factor. The other potential explanation for an optical flare without associated gamma-ray emission may be the location of the flare. An outburst occurring closer to the black hole will occur in a region of enhanced magnetic field and particle density, and possibly a lower Lorentz factor.

Examining the gamma-ray and optical data presented in this thesis, for the same time period, reveals a fourth small optical flare occurring at MJD 55547, hereafter referred to as Flare O4. Overlaying three day binned *Fermi* gamma-ray data suggests a possible correlation.

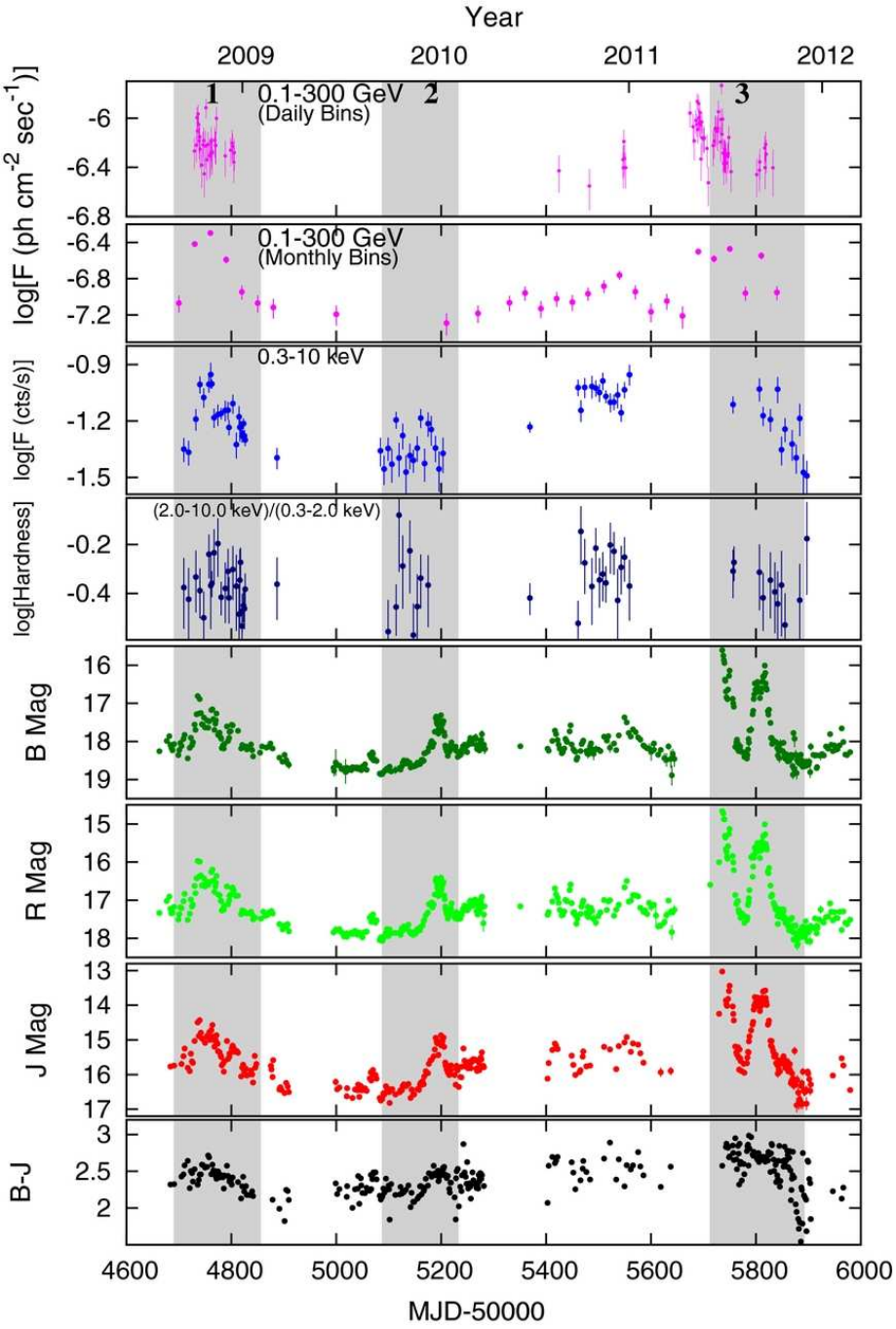

Figure 5.11 Figure 1 from Chatterjee et al. (2013). 0.1300 GeV gamma-ray flux density from *Fermi*-LAT, X-ray flux density from SWIFT and Optical/IR flux density from SMARTS. The three grey shaded regions are considered flaring interval one, two and three.

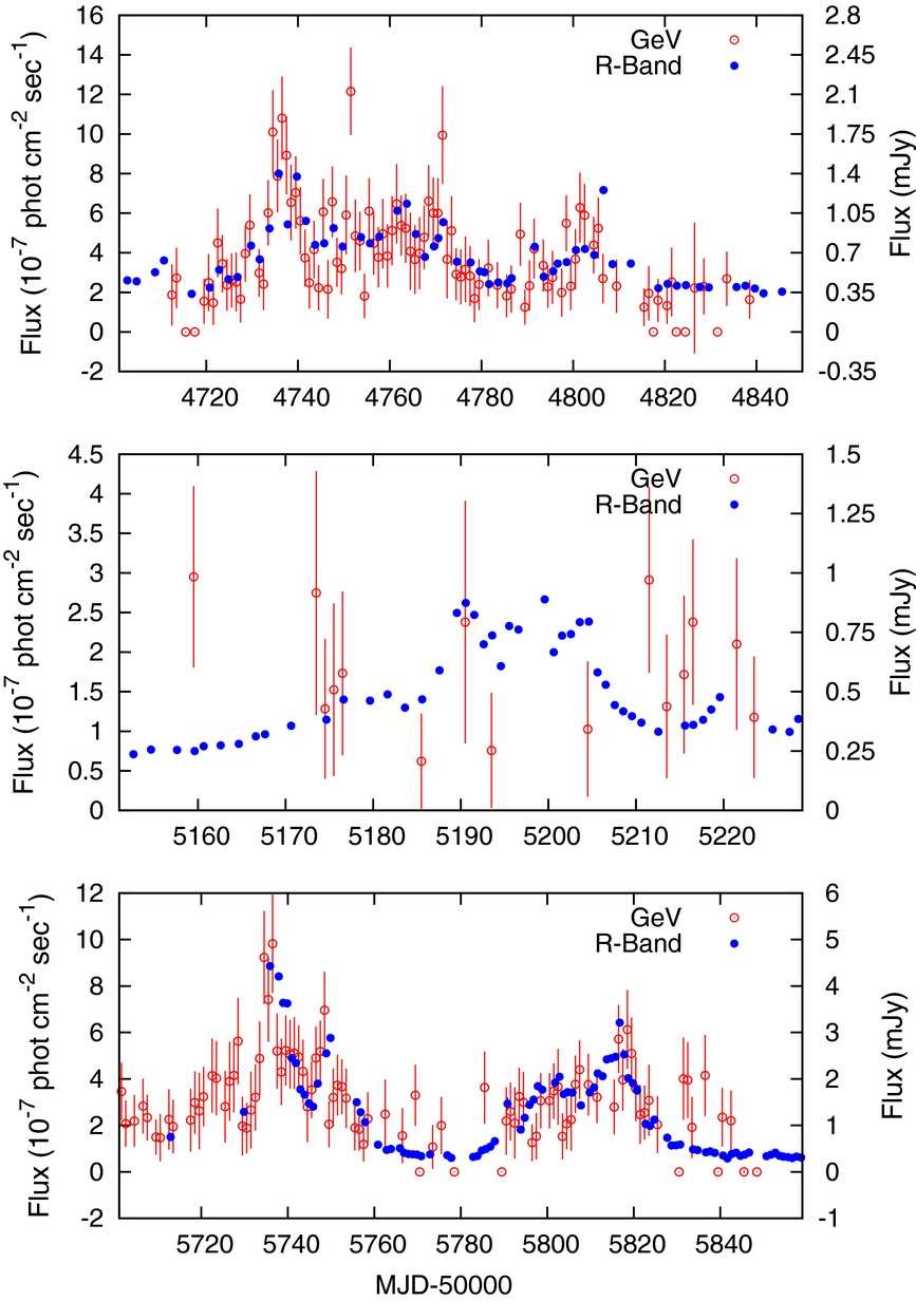

Figure 5.12 Figure 2 from Chatterjee et al. (2013). Gamma-ray and optical R-band flux density during the three flaring intervals. Note the good correlation during interval one and three, and the lack thereof in interval two.

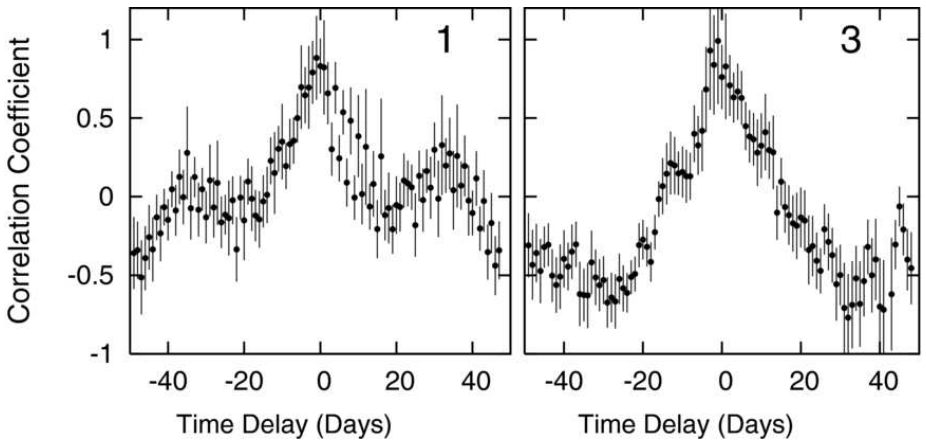

Figure 5.13 Figure 3 from Chatterjee et al. (2013). Discrete cross correlation function for flaring interval one and three. The correlation is consistent with zero lag between the optical and gamma-ray radiation.

This is confirmed when performing a cross correlation analysis, with a statistically significant correlation found at lag 0.2 days ±5, consistent with zero lag (see Figure 5.14).

5.12 Radio - Optical Correlation

As a strong optical to gamma-ray cross correlation was found (Section 5.11), finding a link between optical and radio flaring in PKS 0208–512 would tie the emission together all the way from radio to gamma-ray. This might be more achievable than a straight radio to gamma-ray cross correlation due to the closer relationship between radio and optical emission models. The major emission at both these wavelengths is though to be due to synchrotron emission in the jet (see Chapter 1 for a review).

Multi frequency radio monitoring was undertaken over the same period and the time domain analysis is presented here. The ATCA radio monitoring data were rebinned in frequency space to include all millimetre observations, as presented in Figure 5.15, to aid in visual inspection of the data, however analysis was performed on the frequency bins presented in Section 5.1 as well as the newly binned millimetre ATCA data, the Ceduna 6.7 GHz data, and the APEX high frequency (sub mm) monitoring data.

Discrete cross correlation analysis was performed as explained in Section 5.10. For the full light curve two significant correlations to the optical data were found, one to the APEX monitoring and one to the 92 GHz ATCA data. Both of these show lags consistent with the data presented in Figure 5.10, shown as the blue points in Figure 5.16. The more well sampled radio light curves (for example the Ceduna data) show multiple peaks in the cross correlation analysis, suggesting different behaviour during different flares. For this reason each optical flare was analysed individually, with 500 days of data surrounding the peak of the flare. For flares Flare O1, Flare O3 and Flare O4, statistically significant cross correlations were found

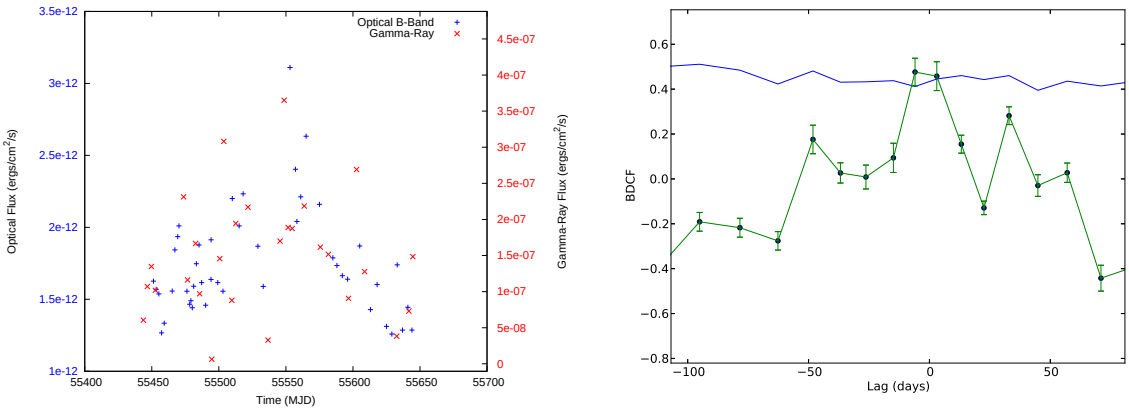

(a) (b)

Figure 5.14 (a) Optical B-band (blue points) and Gamma-Ray (red points) data for the proposed flare occurring at MJD 55547. Errors have been omitted for clarity. (b) The resultant cross correlation of the data.

with lags consistent with the radio cross correlations, and the full light curve optical to radio correlations. These points are the green points shown in Figure 5.16.

For the flare occurring at MJD 55195 however three significant correlations were found with negative lags, that is, the radio flare is preceding the optical flare. This suggests a different emission mechanism or location is occurring during this flaring period. As Chatterjee et al. (2013) propose, the lack of gamma-ray emission during this flare suggests either a change in the magnetic field, or an emission location further 'down' the jet. A change in magnetic field strength would produce both radio and optical flares, however does not explain the radio flare preceding the optical. This leaves the possibility of different emission locations. Possibly, the radio emission is produced as a shock in the jet due to the creation of a new component near the core, with the associated optical flare not being observed until this component has propagated outwards along the jet to a region where the optical emission is not blocked by dust.

For the other three flares cross correlations consistent with an optical depth effect have been found to the optical flaring. Since these optical flares have also been shown to correlate with zero lag to gamma-ray flaring, a consistent model emerges in which flaring occurs first at gamma-ray and optical frequencies, before flaring at lower frequencies with a delay consistent with optical depth effects.

If the gamma-ray emission is assumed to originate from the 'core' of the AGN, then the above relation for delay leads to an expected lag of 121 days between a gamma-ray flare and 8.4 GHz flaring. Since the source has an apparent jet speed of 9.3c (see Chapter 4), this corresponds to a distance from the core of $3.13 \times 10^{15} m$ which equals approximately 0.1 pc. At redshift 0.999 the angular scale is 8.041 kpc/arcsecond, so the apparent angular separation of the emission would be around 0.12 mas, beyond the current resolution limit of VLBI.

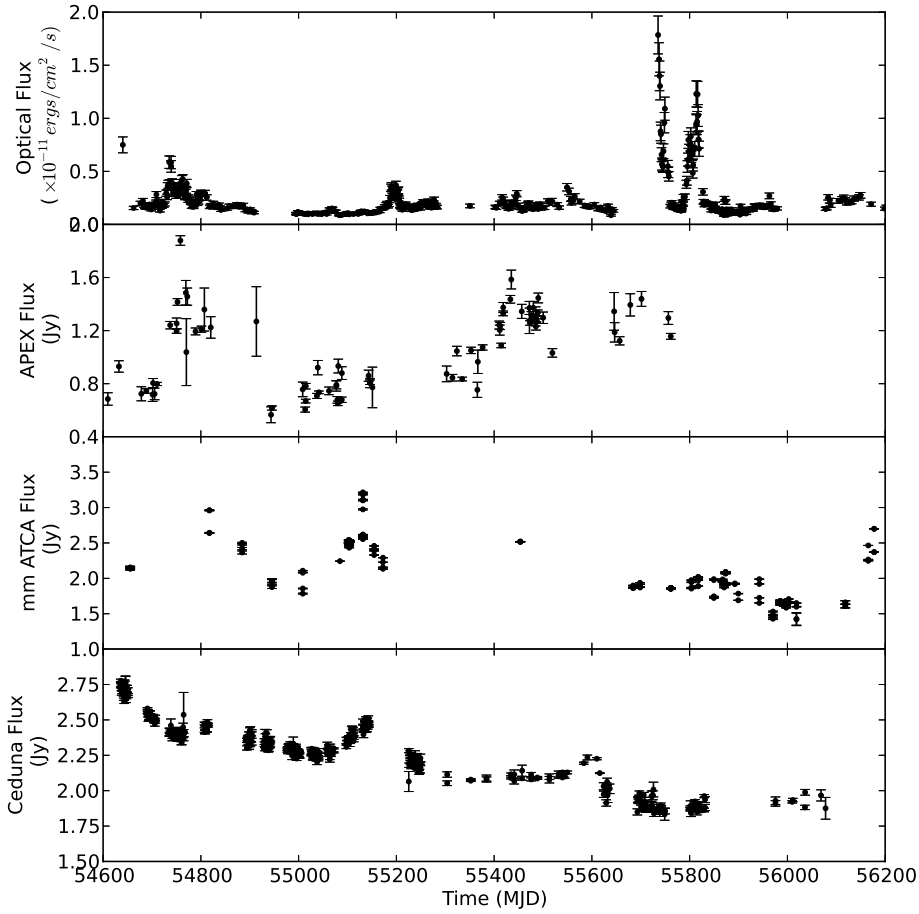

Figure 5.15 Optical B band flux density, APEX sub mm flux density, ATCA mm flux density and Ceduna 6.7 GHz flux density. Note the small flares as well as large longer timescale flux density changes.

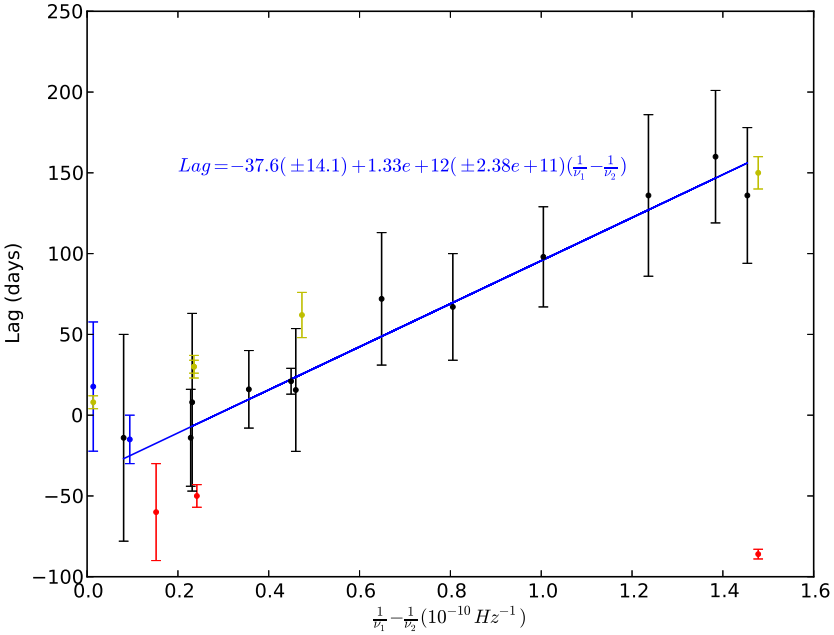

Figure 5.16 The same data as shown in Figure 5.10, overlaid with optical to radio cross correlations. Black points are radio cross correlations, blue points are optical to radio cross correlations for the full light curve, green points are optical to radio cross correlations for the three optical flares with an associated gamma-ray flare, and the red points are optical to radio cross correlations for the optical flare that has no associated gamma-ray flare.

A discussion of the implications of these findings is reserved for Chapter 8.

Chapter 6

Spectral Energy Distribution of PKS 0208–512

The work presented in this chapter was undertaken as part of a collaboration with the author as lead. The following people were also involved as described:

- **Dutka, M**: Gamma-ray light curve and spectra production.
- **Finke, J**: Model Fitting
- **Krauss, F**: X-ray Spectra

Analysis is the work of the author.

The spectral energy distribution of blazars is dominated by two components, one at low energies, often peaking at optical wavelengths, and the other at X-ray and gamma-ray wavelengths (Fossati et al. 1998). The relative intensity of these two components was used by Padovani and Giommi (1995) to classify sources as High-energy peak BL Lacs (HBL) and Low-energy peak BL lacs (LBL). The low energy component emission fits well with a synchroton emission model, but there are two major models currently being considered for the high energy component, being hadronic and leptonic in nature (Böttcher 2007). For the leptonic model, the emission mechanism relies on the inverse Compton effect, upscattering a seed population of photons via collisions with high energy electrons in the jet. The seed population could be internal to the jet (SSC) or external, originating from the accretion disk, the dusty torus, or even potentially from the broad line region. Hadronic models involve a significant fraction of the jet power being used to accelerate relativistic protons up to the threshold for pion production. This requires magnetic field strengths of several tens of Gauss (Boettcher 2010).

Multi frequency, quasi-simulataneous data are required to produce quality SED models of a source, due in part to the highly variable nature of blazar sources at all frequencies. Multiple instruments are thus needed for a well sampled SED.

Table 6.1. The states targeted for SED modelfitting.

Designation	MJD	Date
Active 1	54735	2008-09-26
Active 2	54770	2008-10-31
Active 3	54798	2008-11-28
Quiescent	55323 to 55442	2010-05-07 to 2010-09-03
Active 4	55736	2011-06-24
Active 5	55819	2011-09-15

Note. — MJD and Dates are centre points of a two week window, except for the Quiescent state where they designate the start and end.

In this chapter SEDs for five active and a quiescent state of the blazar PKS 0208–512 are presented, and the implication for emission models for the source are discussed.

6.1 Data

Some of the data used in this analysis have been previously presented in Chapter 5, however they are re-produced here for clarity and due to a few subtle differences in the data reduction employed. Data from the LAT onboard *Fermi* were used as the 'trigger' for this analysis and are presented in Figure 6.1. These data have been binned into weekly time bins. Five active states of the source were selected based on the test statistic of the gamma-ray points, and all data within two weeks of that date were collated for SED production. These are designated by the blue lines in Figure 6.1. High test statistics were chosen both as they coincide with flaring events in the source, and as they allow for more precise gamma-ray spectra to be calculated. In addition, the SED was also calculated for a quiescent period of the source, designated by the shaded region in Figure 6.1. The gamma-ray data show two distinct flaring periods, one at around MJD 54750 (October 2008), and the other at around MJD 55750 (July 2011). The first period shows a double sharp flare, and then a slower fall with a secondary flare during the falling phase. The peak, the secondary flare, and the tail of the first flare were all selected for SED analysis. The latter flare is less sharply defined and corresponds to a much longer time period. There are again two distinct flares within this region and both have been targeted for SED analysis. These targeted periods will henceforth be referred to by the designation assigned in Table 6.1.

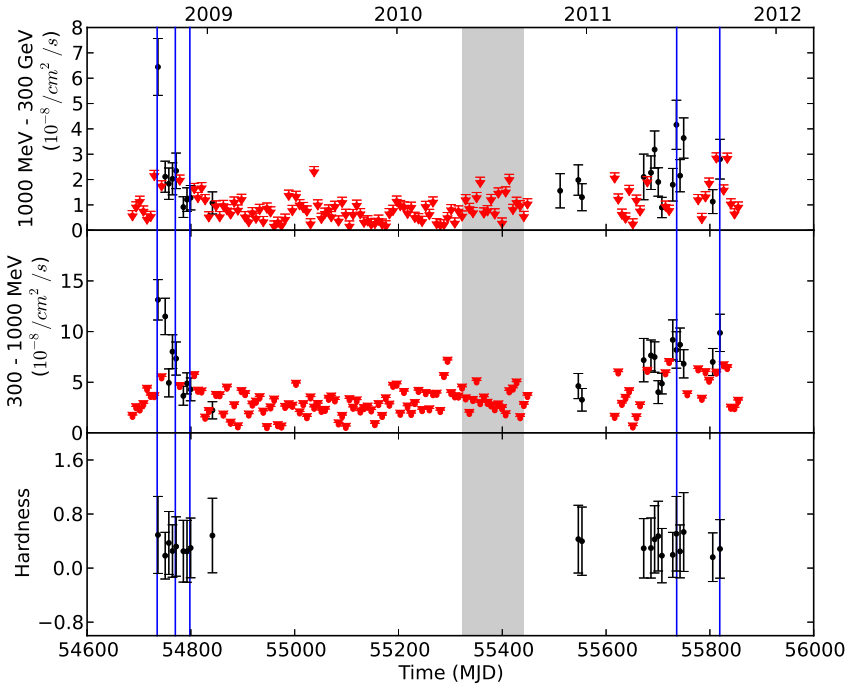

Figure 6.1 Gamma-ray light curve and hardness ratio of PKS 0208–512. The blue lines mark the active states for which an SED has been calculated, and the gray shaded area represents the time range used for calculating a quiescent SED. Red points are upper limits.

6.1.1 Radio Data

The radio data used for the SED modelling comes from the Ceduna and ATCA monitoring programs in support of the TANAMI project, described in Chapter 5. These data are shown in Figure 6.2. Again the quiescent SED zone is designated by the gray shaded area, and the active SED centre points are designated by the blue lines. This gives multiple radio points for the SEDs, at 1.4, 2.4, 5, 6.7, 8.8, 20, 39, and 92 GHz. The radio data show a major flare around 200 days before the gamma-ray flare, however the higher radio frequencies (17-24 GHz and 33-45 GHz) do appear to show a radio flare coincident with the first gamma-ray flare. The second gamma-ray flaring period does not show any co-occurring radio activity.

6.1.2 Optical Data

Optical data used for the SED analysis has been provided by several instruments, some which are dedicated to monitoring and some targeted observations.

SMARTS

The Small and Moderate Aperture Research Telescope System (SMARTS) uses a 1.3 m class telescope fitted with dichroic filters. This allows simultaneous optical and infrared observations to be performed. SMARTS monitors a subset of *Fermi* detected blazars at daily cadence, providing an excellent resource for SED modelling. The SMARTS data at B, R, V, J, and K bands is shown in Figure 6.3. These data have been corrected for optical extinction based on Fitzpatrick (1999), and converted to $\nu S(\nu)$ in preparation for SED modelling. Errors are dominated by the uncertainty in the extinction correction, resulting in roughly 5% errors. The SMARTS data show several flaring states, the first well correlated with the first gamma-ray flare at MJD 54750 (October 2008). There appear to be distinct peaks during each of the targeted SED states Active 1, 2 and 3. This is also the case during the other two targeted SED analysis regions Active 4 and Active 5, with two very distinct flares coincident with the gamma-ray flaring (last two blue lines on Figure 6.3). There is however an optical/IR flare at around MJD 55200 which has no associated gamma-ray flare whatsoever (discussed in detail in Chapter 5).

SWIFT-UVOT

The SWIFT satellite was designed to detect and analyse gamma-ray bursters (GRBs), using a hard X-ray detector (the Burst Alert Telescope, BAT), an X-ray Telescope (XRT), and a UV/optical telescope designed for monitoring the optical/UV afterglow of GRBs. BAT constantly monitors for GRBs and SWIFT can rapidly reorient to a target. This allows the other instruments to be used for pointing science in between GRB detections, making SWIFT an excellent tool for monitoring, particularly with SED modelling in mind, as both X-ray and optical/UV data are provided simultaneously. The UVOT data used here have been reduced

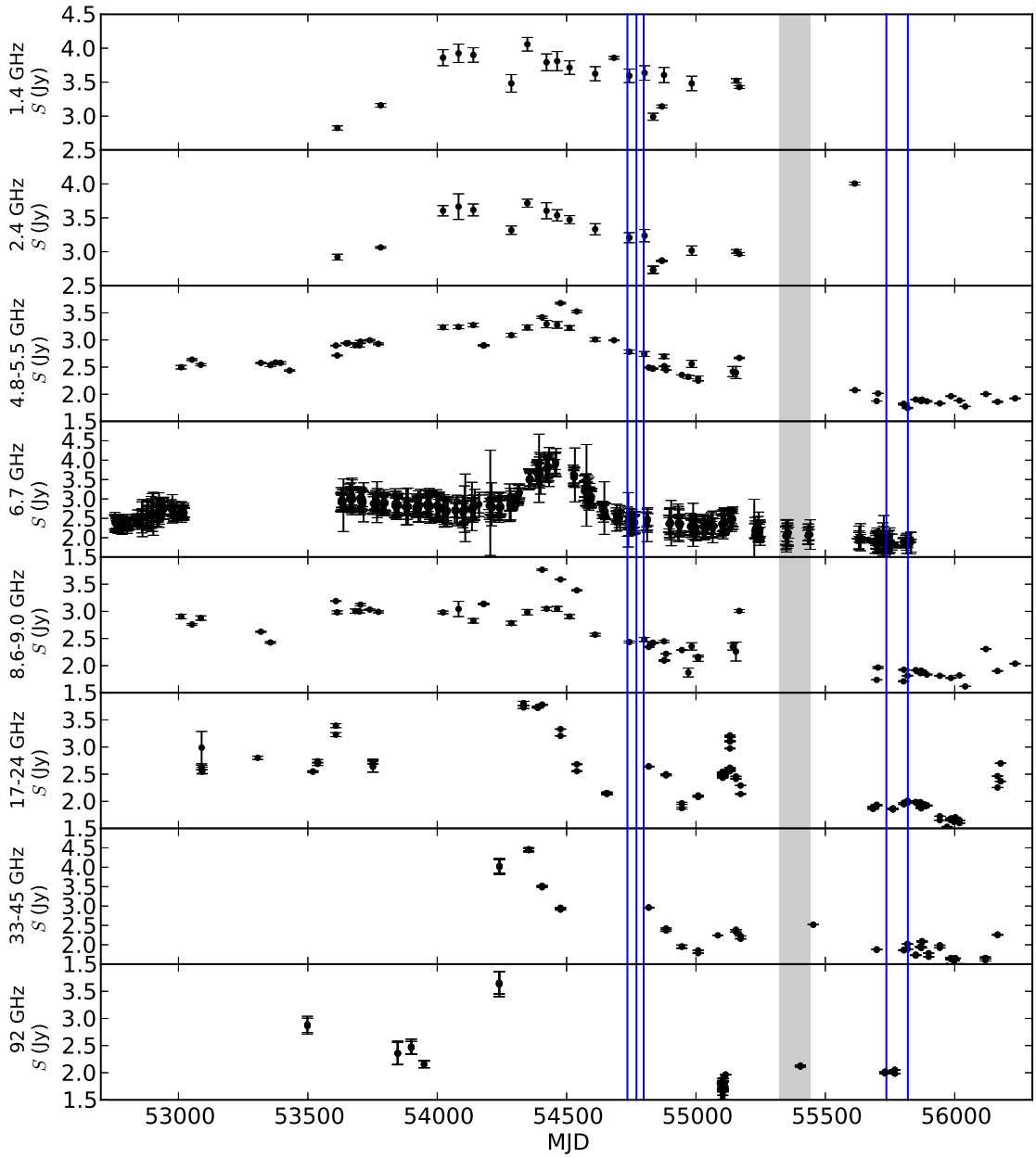

Figure 6.2 Radio light curves of PKS 0208–512 from Ceduna single dish and ATCA monitoring data. The blue lines mark the active states for which an SED has been calculated, and the gray shaded area represents the time range used for calculating a quiescent SED.

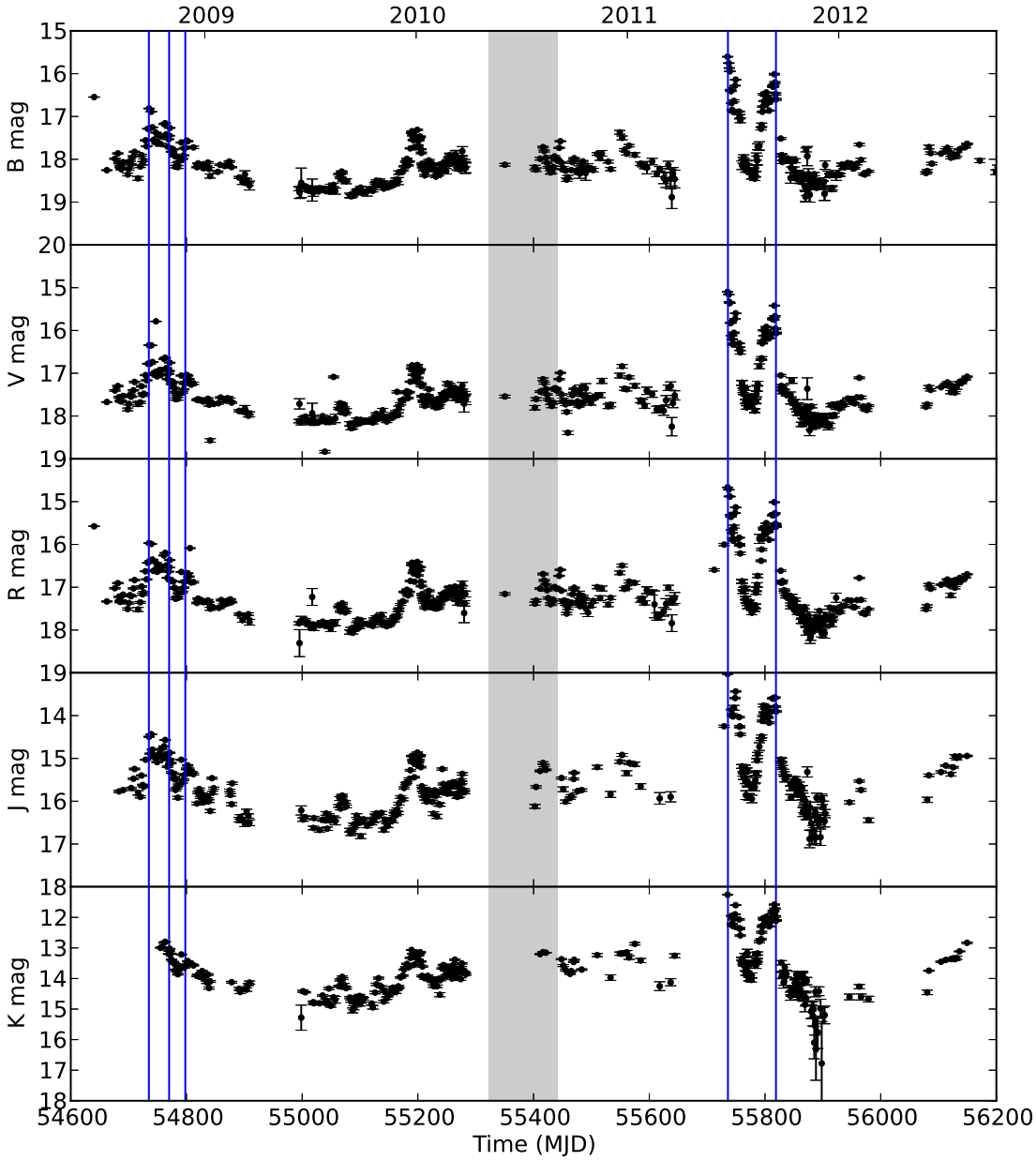

Figure 6.3 SMARTS optical and near-infrared monitoring of PKS 0208–512. The gray shaded area is the time range for which a quiescent SED has been calculated, and the blue lines are the centre points of the active SEDs.

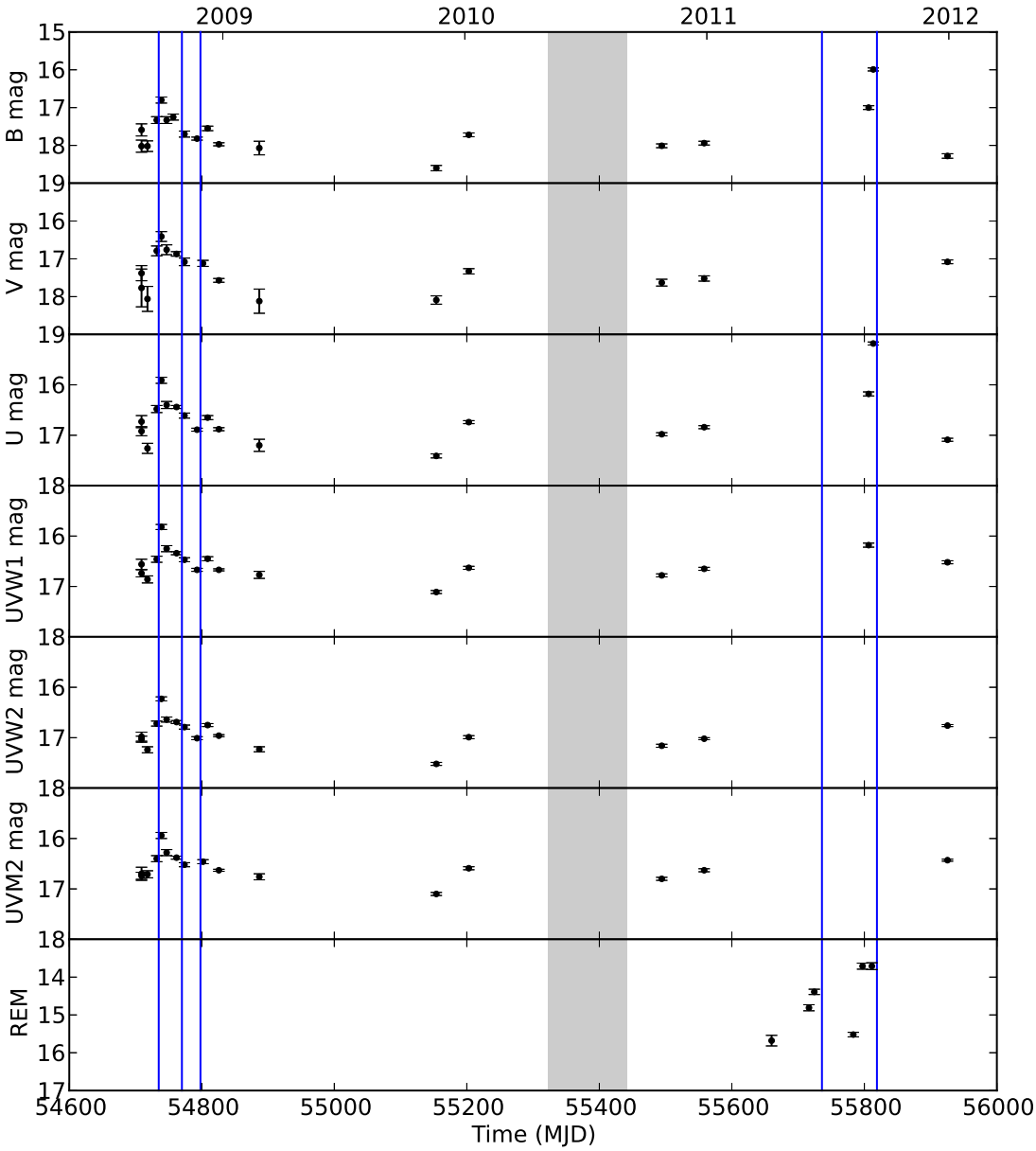

Figure 6.4 Swift-UVOT monitoring of PKS 0208–512 at various optical and ultraviolet bands, as well as some higher cadence REM observations over the course of a bright optical flare. The gray shaded area is the time range for qhich a quiescent SED has been calculated, and the blue lines are the centre points of the active SEDs. Note there are no SWIFT data during the quiescent period. This does not affect the analysis as there are sufficient SMARTS and WISE data available over the interval.

using the UVOT reduction task UVOTSOURCE, providing aperture photometry. Again, extinction corrections dominate the errors, and are calculated as described by Fitzpatrick (1999). This results in approximately 5 % errors at V B and U bands, and 25 % errors in the UV bands. The resultant light curves are shown in Figure 6.4. The SWIFT data show an optical/UV flare consistent with the SMARTS data. The second flare at around MJD 55750 is not as well sampled, however the REM data are available during this time, and do show the flare.

REM

The Rapid Eye Mount (REM) telescope was also used in a targeted observation of PKS 0208–512 during the major gamma-ray flare in 2010. REM is a 60 cm class telescope located at the ESO Observatory in Chile, and operates in the near infrared band. The REM light curve is shown in Figure 6.4.

WISE

The quiescent SED was enhanced further by the inclusion of data from the Wide Field Infrared Survey Explorer (WISE). WISE operated at infrared wavelengths of 3.4, 4.6, 12 and 22 μm, and performed an all sky survey. This provides an extra datapoint during the quiescent SED period, with excellent calibration (errors to within 2 %). The WISE data are taken from the data products of the Wide-field Infrared Survey Explorer, which is a joint project of the University of California, Los Angeles, and the Jet Propulsion Laboratory/California Institute of Technology, funded by the National Aeronautics and Space Administration.

6.1.3 SWIFT-XRT

SWIFT-XRT data have been used to produce the X-ray light curve shown in Figure 6.5. This has been created by reducing all targeted SWIFT observations of PKS 0208–512 during the observation period, and includes observations in both window timing and photon counting modes. X-ray spectra have also been calculated where possible, that is, when enough data were available. These will be discussed further with respect to the individual SEDs produced.

6.2 SED Modeling

The SED model used in this analysis is a leptonic model, consisting of a low energy synchrotron component, and both a synchrotron self-Compton component (SSC), and an external Compton component for the higher energy 'hump'. A disk emission spectrum is also added, using a Shakura Sunyaev disk with black hole mass 8.0×10^8 solar masses, a disk luminosity of 0.06 times the Eddington luminosity, an accretion efficiency of 1/12 and an inner disk radius of $6R_g$ (where R_g is the Schwartzschild radius).

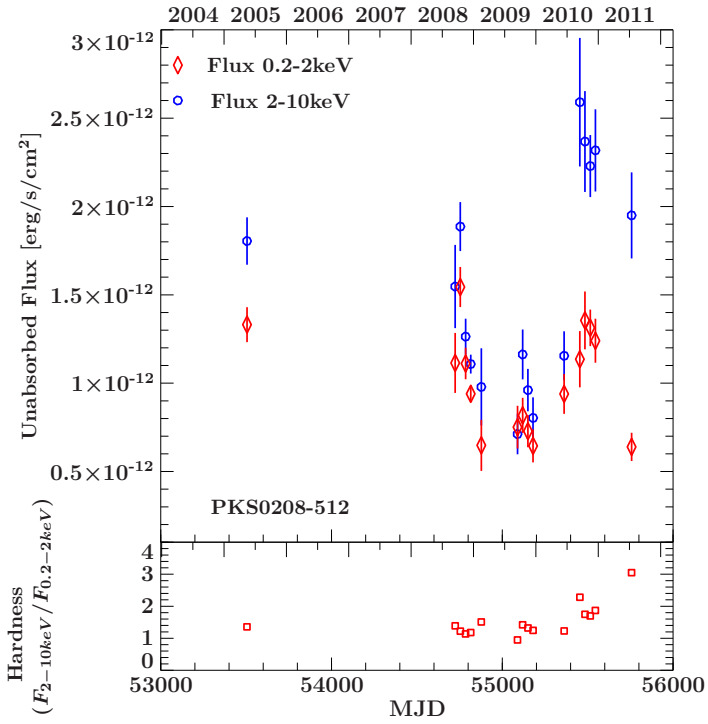

Figure 6.5 X-ray monitoring of PKS 0208–512 from SWIFT-XRT.

The external Compton emission assumes an isotropic and mono-energetic external radiation field, in the frame stationary to the black hole, with energy density u_0 and mono-energetic photon energy ϵ_0. These values are given in Table 6.2. Note that they do not change between the states being modelled, and are consistent with the external radiation source consisting of a dusty torus. The Lorentz and Doppler factors are assumed to be equal and are also held constant between models. The electron population is modelled with a broken power law with indices p_1 and p_2 below and above break Lorentz Factor γ_{brk}.

Low frequency radio flux densities are not directly included in the model due to the difference in assumed emission region size. Radio emission can originate from kpc scale regions, compared to pc scale regions for gamma-ray emission. Millimetre radio flux densities are however included, as the emission is not as affected by optical depth effects and is thus likely to orginate from the same regions as the optical emission. The WISE data were used to renormalize the UVOT and SWIFT-UVOT data.

6.2.1 Quiescent

The quiescent state of the source has been defined as the time period between MJD 55323 and 55442, the shaded region in Figures 6.1, 6.2, 6.3 and 6.4. All data within this region were used to calculate and model the SED of the source. This region was carefully chosen to contain no flaring at any of the frequencies sampled. A gamma-ray spectrum was calculated based on these data, as well as an X-ray spectrum. The SED is shown in Figure 6.6 and

Parameter	**Symbol**	**Quiescent**	**Active 1**	**Active 2**	**Active 3**	**Active 4**	**Active 5**
Bulk Lorentz Factor	Γ	30	30	30	30	30	30
Doppler Factor	δ_D	30	30	30	30	30	30
Magnetic Field [G]	B	0.5	0.16	0.25	0.25	0.25	0.3
Variability Timescale [s]	t_v	7×10^4	2.2×10^5	4.3×10^5	4.3×10^5	4.3×10^5	2.2×10^5
Comoving Blob Radius [cm]	R'_B	3.1×10^{16}	9.9×10^{16}	1.7×10^{17}	1.7×10^{17}	1.7×10^{17}	9.9×10^{16}
Low-Energy Electron Spectral Index	p_1	2.0	2.0	2.0	2.0	2.0	2.0
High-Energy Electron Spectral Index	p_2	3.8	3.2	3.4	3.55	2.9	3.4
Minimum Electron Lorentz Factor	γ_{min}	1.0	1.0	1.0	1.0	1.0	1.0
Break Electron Lorentz Factor	γ_{brk}	8.5×10^2	8.5×10^2	2.7×10^2	2.7×10^2	2.7×10^2	8.5×10^2
Maximum Electron Lorentz Factor	γ_{max}	2.0×10^4	2.3×10^4	8.0×10^3	8.0×10^3	1.0×10^4	1.0×10^4
Seed photon source dimensionless energy	ϵ_0	1.3×10^{-6}	1.3×10^{-6}	1.3×10^{-6}	1.3×10^{-6}	1.3×10^{-6}	1.3×10^{-6}
Seed photon source energy density [erg cm^{-3}]	u_0	$1.45 \times 10^{-5}5$	1.45×10^{-5}	1.45×10^{-5}	1.45×10^{-5}	1.45×10^{-5}	1.45×10^{-5}
Jet Power in Magnetic Field [erg s^{-1}]	$P_{j,B}$	1.7×10^{45}	1.6×10^{45}	1.6×10^{46}	1.6×10^{46}	1.6×10^{46}	6.0×10^{45}
Jet Power in Electrons [erg s^{-1}]	$P_{j,e}$	7.9×10^{45}	1.6×10^{46}	1.6×10^{46}	1.5×10^{46}	1.2×10^{46}	1.0×10^{46}
Black Hole Mass [M$_o$]	M_{BH}	8×10^8	8×10^8	8×10^8	8×10^8	8×10^8	8×10^8
Accretion Efficiency	e	1/12	1/12	1/12	1/12	1/12	1/12
Inner Disk Radius [R_g]	R_{in}	6	6	6	6	6	6
Disk Luminosity [erg s^{-1}]	L_D	6.25×10^{45}	6.25×10^{45}	6.25×10^{45}	6.25×10^{45}	6.25×10^{45}	6.25×10^{45}

Table 6.2 Model Parameters for the quiescent and all five active states.

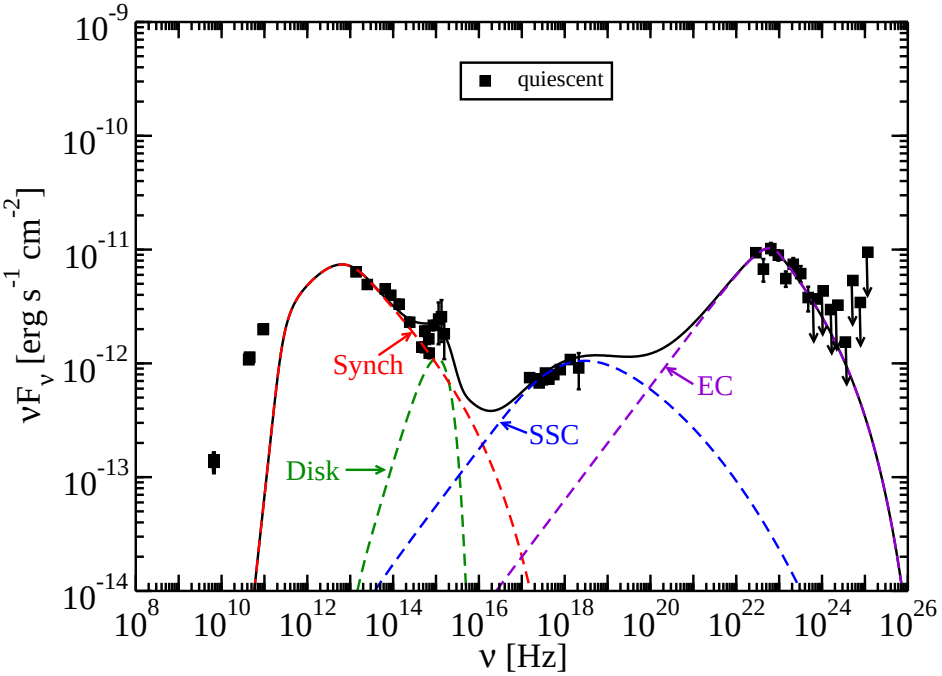

Figure 6.6 Quiescent SED for PKS 0208–512. Note the two distinct humps produced by a synchrotron component (low energies), and an inverse Compton component (high energies). The high frequency inverse Compton component is consistent with seed photons originating in the dusty torus. The broken green line is the contribution to the model by thermal emission from the accretion disk, the broken red line shows the contribution by the synchrotron component, the broken blue line shows the contribution by the SSC component and the broken purple line the contribution by the EC component.

the model parameters are shown in Table 6.2. The model is consistent with a synchrotron component at low energies (radio to UV), a small component due to thermal emission in the accretion disk, and then an inverse Compton component at the higher frequencies, SSC at X-ray and external Compton (EC) at gamma-rays. The jet power is dominated by nonthermal electrons , and the seed photons are consistent with a dusty torus.

6.2.2 Active 1

The first active state is centered on MJD 54735 (2008-09-26), which is the largest peak of the gamma-ray lightcurve (first blue line in Figure 6.1). A separate gamma-ray spectrum was produced for this state. The X-ray spectrum produced was modelled based on the averaged X-ray data from active states 1,2 and 3. This was done to improve the accuracy of the spectrum, and is justified by the lack of X-ray variability during the flare, the X-ray flux density varies by less than a factor of two during the first three active states which does not effect the modeling. The resultant SED is shown in Figure 6.7. In order not to overproduce

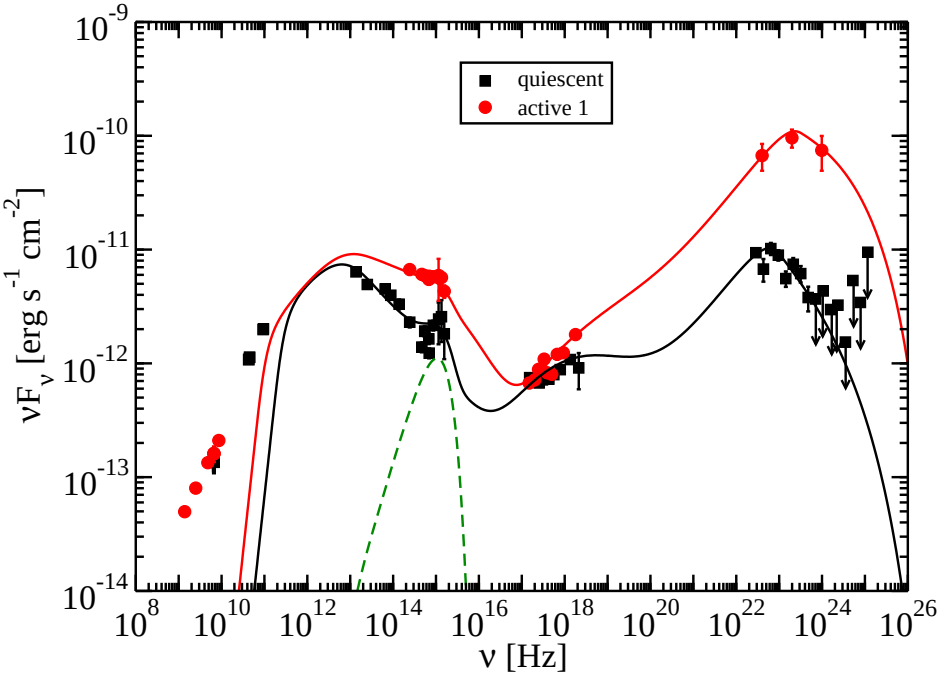

Figure 6.7 SED of PKS 0208–512 during the first active state (red), compared to the quiescent SED fit for the source (black). Note the increase in power of both the synchrotron component and the inverse Compton component.

the X-ray emission, the size of the emission region had to be increased in the model, and the magnetic field strength decreased. This results in a very similar magnetic jet power to the quiescent state, but an increase in the electron jet power by nearly a factor of two. The peak of the Compton component lies within the LAT bandpass.

6.2.3 Active 2

The centre point of the second active state for which an SED has been modelled is at MJD 54770, 35 days after Active 1. The same X-ray spectrum has been used as in Active 1 but a new gamma-ray spectrum was produced. The resultant SED fit can be seen in Figure 6.8. The optical data are clearly softer than in both the Quiescent and the Active 1 state, and the gamma-ray spectrum appears to peak at a lower frequency than the Active 1 state. As such, the $\gamma_{\rm brk}$ of the electron distribution had to be reduced by almost a factor of three. The size of the emission region was also increased again. This would agree with a physical interpretation of an expanding emission zone as the flare progresses. This results in a magnetic jet power roughly 10 times that of the Active 1 and Quiescent states, the nonthermal electron and Poynting flux energy densities are in equipartition. Reaching equipartition at the peak of a flare is consistent with the supposition of Readhead (1994), who propose something similar for radio flares.

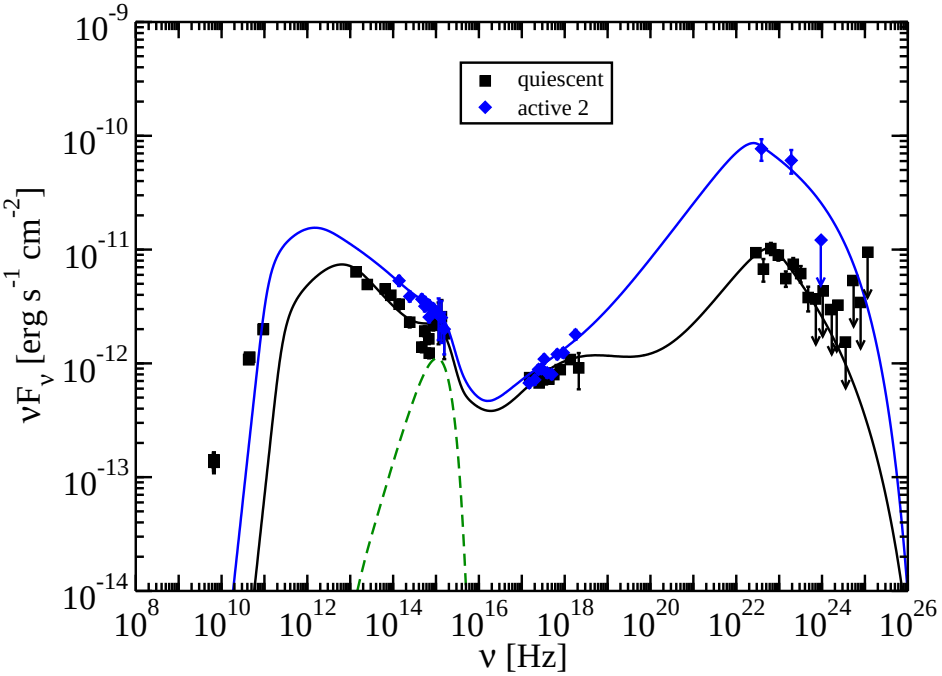

Figure 6.8 SED of PKS 0208–512 during the second active state (blue), compared to the quiescent SED fit for the source (black).

6.2.4 Active 3

The third active state SED calculated for PKS 0208–512 is centered around MJD 54798. This is the last SED produced for the first gamma-ray flare, and lies on the tail of the flare, a further 29 days after Active 2. Again, the same X-ray spectrum was used as in Active 1 and Active 2. A new gamma-ray spectrum was fit to the gamma-ray data and used in the model. The resultant SED can be seen in Figure 6.9. This SED is almost identical to that of Active 2, with again the gamma-ray peak occuring at a lower frequency than the Active 1 state. The only difference in the model for Active 2 required was a change in the electron distribution, with the magnetic field and blob size the same.

6.2.5 Active 4

This SED focuses on the first peak of the second major gamma-ray flare observed from PKS 0208–512. The gamma-ray spectrum produced for this SED is very flat, requiring a hardening of the electron distribution above γ_{brk}. The synchrotron component of the SED calculated for this state is relatively poorly constrained due to the scarcity of optical data available. It was possible to fit a very similar model as those for Active 2 and Active 3, apart from the hardening of the electron distribution already mentioned. The resultant SED is presented in Figure 6.10.

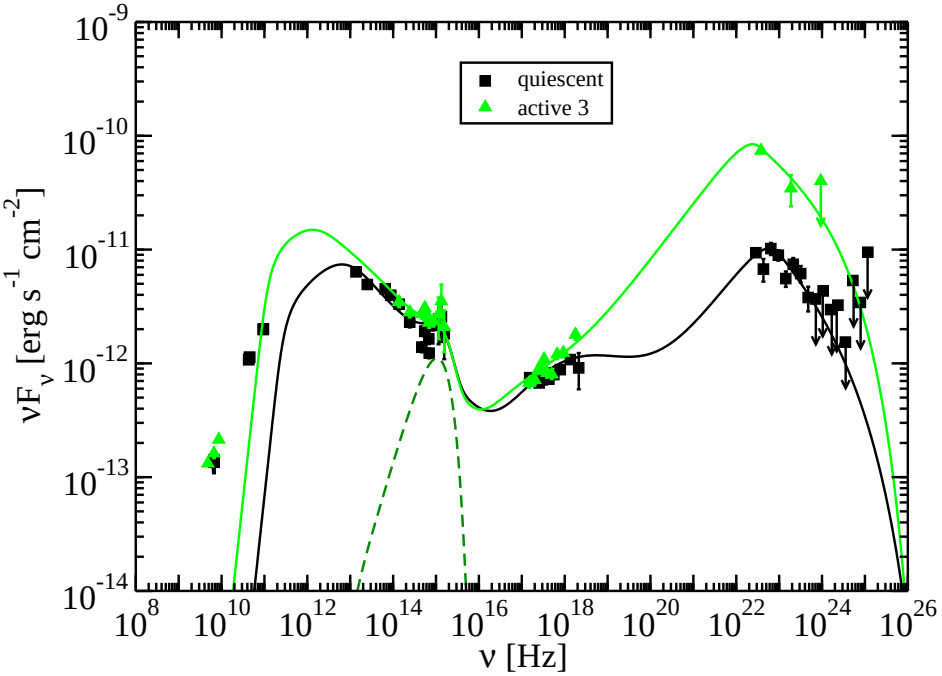

Figure 6.9 SED of PKS 0208–512 during the third active state (green), compared to the quiescent SED fit for the source (black).

6.2.6 Active 5

The last SED modeled for PKS 0208–512 is centered on MJD 55819, which is the second peak in the second major gamma-ray flaring period. This is an interesting flare as no associated radio flaring was observed at the time. This state most resembles Active 1, with the peak of the gamma-ray emission increasing back to a higher frequency than Active 2, 3 and 4. The major difference is a much brighter optical component, requiring an increase in the magnetic field strength. The SED for this state is shown in Figure 6.11. The emission region size is again consistent with Active 1.

6.3 Implications

The electron jet power remains very similar for all of the SEDs fit, with the major difference in the models being in the electron distribution parameters, the size of the emission region and the nature of the magnetic field. All the active states show an increase in the jet power contained in the electron distribution compared to that seen in the quiescent state. A combined figure of all the SEDs is shown in Figure 6.12. The evolution of a flare as modelled by the SED suggests a relatively small emission zone, with an initial drop in the magnetic field strength, and then an increase in the size of the emission region, and an increase in the

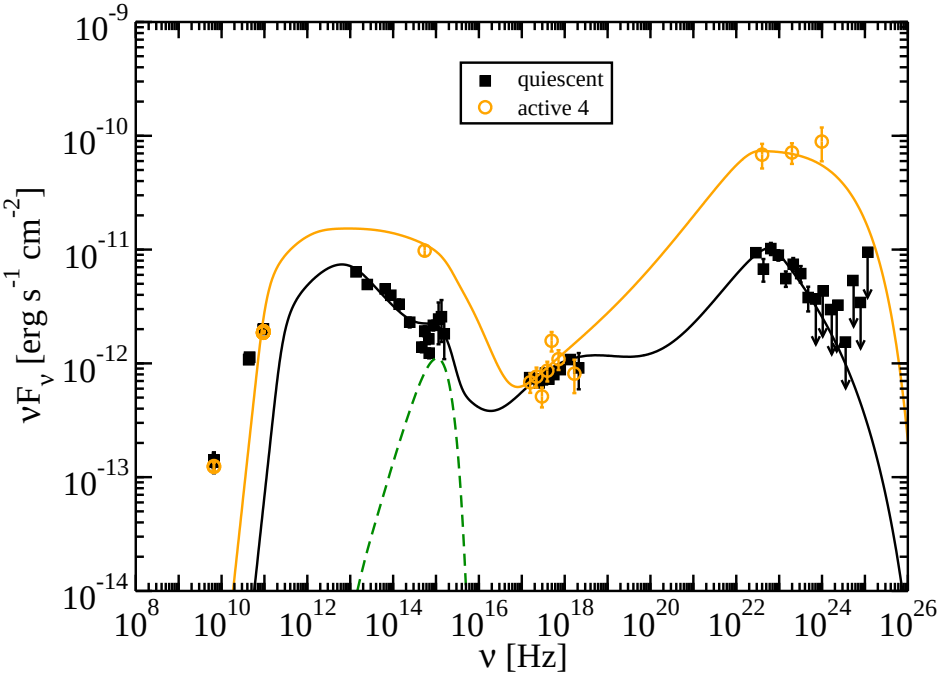

Figure 6.10 SED of PKS 0208–512 during the fourth active state (orange), being the first SED calculated during the peak of the second major gamma-ray flare observed from the source, compared to the quiescent SED fit for the source (black).

magnetic field strength as the flare tails off. The major components are synchrotron emission extending out to the optical (with a small bump from the accretion disk in the optical) and an inverse Compton component dominated by seed photons from the dusty torus. SSC (while present) does not appear to be a major component of the emission detected from PKS 0208–512.

An analysis of the results found in this Chapter, as well as in Chapters 4 and 5 is reserved for the Conclusions presented in Chapter 8, Section 8.1.1.

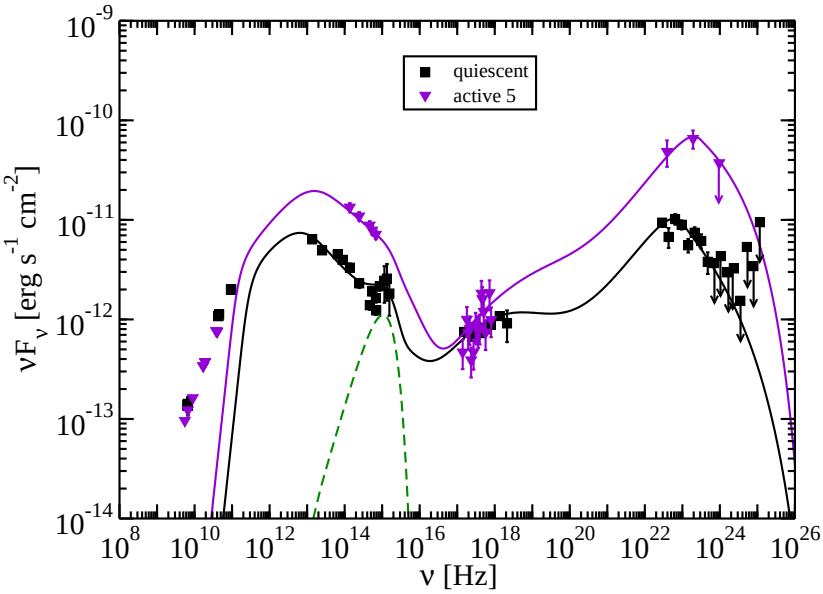

Figure 6.11 SED of PKS 0208–512 during the fifth active state (purple), the last SED calculated during the second peak of the second major gamma-ray flare observed from the source, compared to the quiescent SED fit for the source (black).

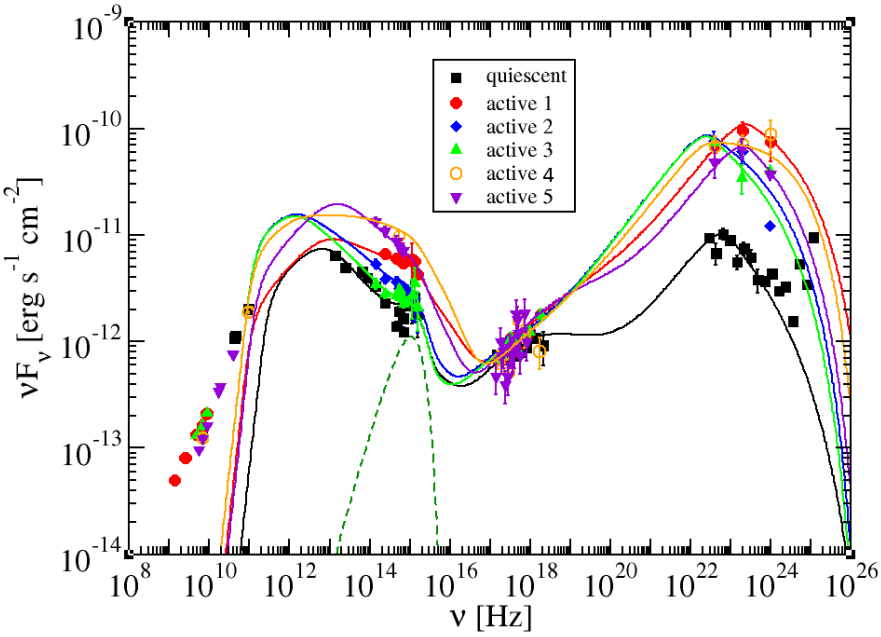

Figure 6.12 All the SEDs modelled for PKS 0208–512 for comparison.

Chapter 7

Other Sources

The analysis presented in Chapter 5 is applied here to three other blazars: PKS 1424–418, PKS 2052–474, and PKS 1622–253. These sources were selected based on their radio and gamma-ray lightcurves, all show at least one major flare in each band and have high cadence radio monitoring data available.

7.1 PKS 1424–418

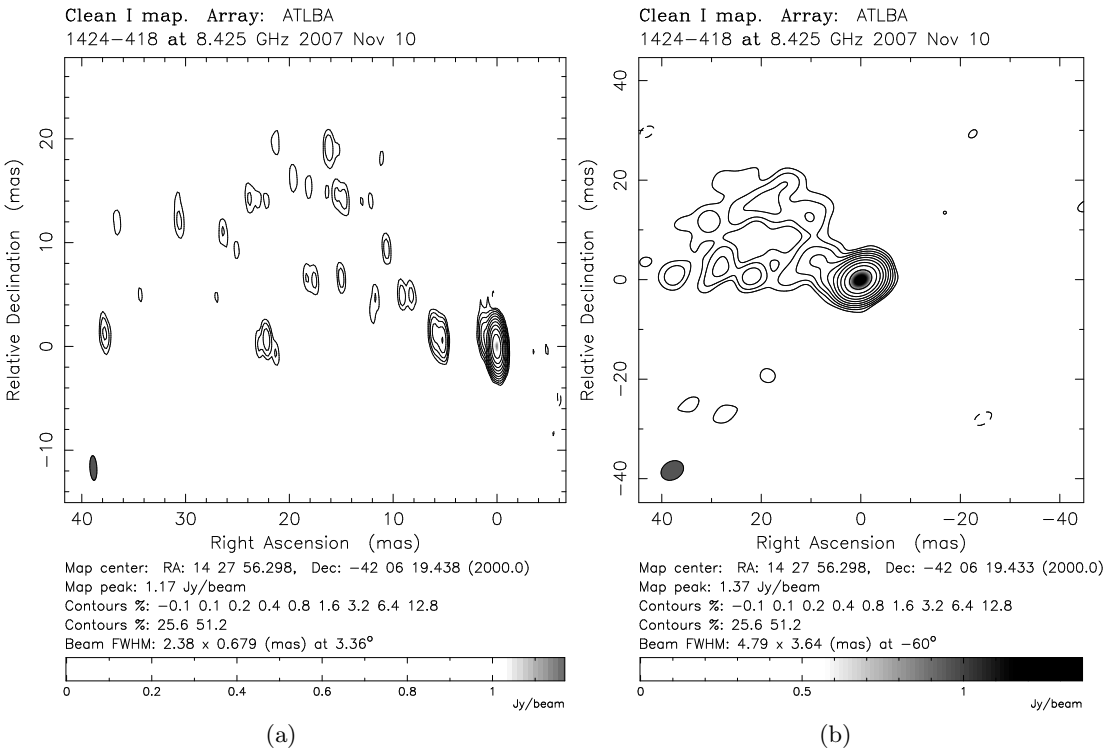

(a) (b)

Figure 7.1 (a)8.4 GHz X-band image of PKS 1424–418. (b) The same image tapered to favour the Australian only baselines. This better shows the extended emission in the jet.

PKS 1424–418 is a flat spectrum radio quasar (FSRQ) located at a redshift of 1.522 (Healey et al. 2008). It shows a high level of optical polarisation, up to 9.43 % (Impey and Tapia 1988). PKS 1424–418 was imaged by Preston et al. (1989) using the first southern VLBI array at 2.3 GHz, finding a core with a peak flux density of 1.06 Jy and a north eastern jet-like component extending out around 25 mas. It was also a target of the VSOP space VLBI mission, which also detected a north east pointing jet as well as fitting a lower limit to the brightness temperature of $1.2 \times 10^{12} K$ (Tingay et al. 2002) to the unresolved core. PKS 1424–418 is part of the TANAMI observing program, and has been imaged at both 8.4 and 22 GHz on multiple epochs. The first epoch 8.4 GHz image is presented in Figure 7.1 (see Ojha et al. (2010) for a full presentation of the program, calibration and imaging performed) and shows a core with peak flux density 1.17 Jy, a second bright component around 5 mas east thereof and then a well resolved jet extending north east.

The jet has an opening angle of 47.9 degrees (Ojha et al. 2010), which is well above the mean value for LAT detected blazars of 22.9 ± 1.5 degrees (Pushkarev et al. 2009). As noted therein, *Fermi* - LAT detected blazars show, on average, larger opening angles than non LAT detected blazars. Jet opening angle is an important parameter used in the modelling of jet formation and magneto-hydrodynamics. It is often used in conjunction with the Lorentz factor, to model the interaction of the ambient medium to the jet's internal pressure, as well as affecting the the structure of the shocked regions in the jet and the jet stability (Clausen-Brown et al. 2013).

7.1.1 Gamma-ray Properties

PKS 1424-418 was detected by the EGRET mission multiple times in 1994 and 1995, including the tail end of a flare in 1994 followed by the source falling below detection limits, only to be redetected in 1995. This resulted in speculation that this was a very active source in the gamma-ray regime (Mukherjee et al. 1997).

Fermi-LAT detected increased gamma-ray emission coincident with the source location from the 17th to the 23rd of June 2009, with a flux density of $6 \pm 2 \times 10^{-7}$ photons/cm^2/s (Longo et al. 2009). The source then flared again on April 21, 2010 this time with a flux density of $1 \pm 0.2 \times 10^{-6}$ photons/cm^2/s, an increase of more than a magnitude over its average flux density prior to the flare (Donato 2010), and again on May 5 2011 with a flux density of $1.1 \pm 0.3 \times 10^{-6}$ photons/cm^2/s (Szostek 2011). Most recently, flaring has been observed from October 1 to October 14, 2012, with a gamma-ray flux density of $1.4 \pm 0.2 \times 10^{-6}$ photons/cm^2/s for the energy band greater 100 MeV (see the lightcurve presented in Figure 7.2). Increased X-ray flux density was also detected during this time by SWIFT-XRT (Gal-Yam et al. 2012).

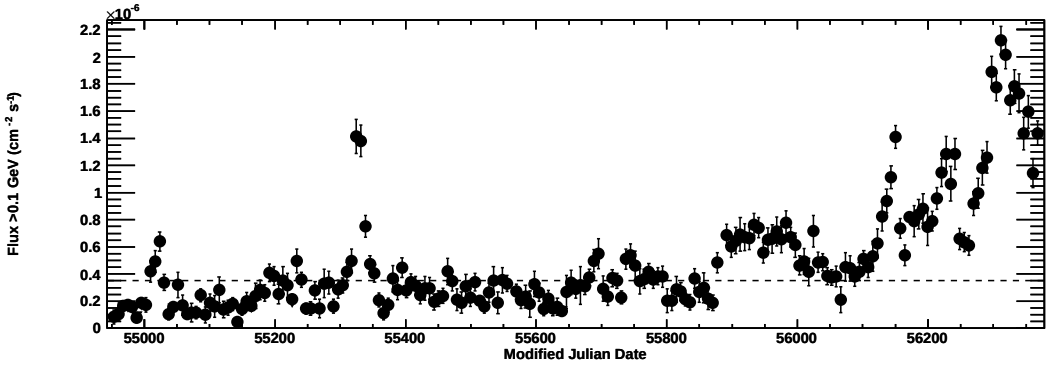

Figure 7.2 7 Day binned *Fermi*-LAT light curve of PKS 1424–418.

7.1.2 Radio Monitoring

After the 2010 flare, PKS 1424–418 was added to both the Ceduna single dish monitoring at 6.7 GHz and the ATCA multifrequency monitoring, both supporting the TANAMI project. Some ATCA monitoring data taken prior to the 2010 flare for other observing programs were also available. The multifrequency light curves from these programs are presented in Figure 7.3. The Figure also shows S-band (2.4 GHz) and X-band (8.4 GHz) data obtained from International VLBI Service (IVS) observations of the source (Schlüter and Behrend 2007b). While in general the flux density calibration of IVS observations is quite poor (flux density monitoring is not the primary goal of these observations) the frequent nature of the observations allows aggressive averaging to be applied and thus generates acceptable errors. That is, the relative error in the flux density become quite low, and as the analysis performed normalises with respect to flux density the relative flux density is much more crucial than the absolute scale. In this case the data have been adaptively binned into unequal size time bins, such that each bin contains 20 individual observations. This provides a more even distribution in the error for each bin. Equal error binning was attempted but it was found that this applied too much averaging over time periods in which the source was varying quickly.

7.1.3 SMARTS

The Small and Moderate Aperture Research Telescope System (SMARTS) team have also been monitoring this source at optical and infrared wavelengths, and their data are used in the analysis presented herein. The respective SMARTS lightcurves are shown in Figure 7.4.

7.1.4 *Fermi*

PKS 1424–418 is bright enough at gamma-ray wavelengths to be detected using weekly binning at all times since its first detection. The *Fermi* gamma-ray light curve is presented in Figure 7.2. An overview of the gamma-ray, optical and radio lightcurves is shown in Figure

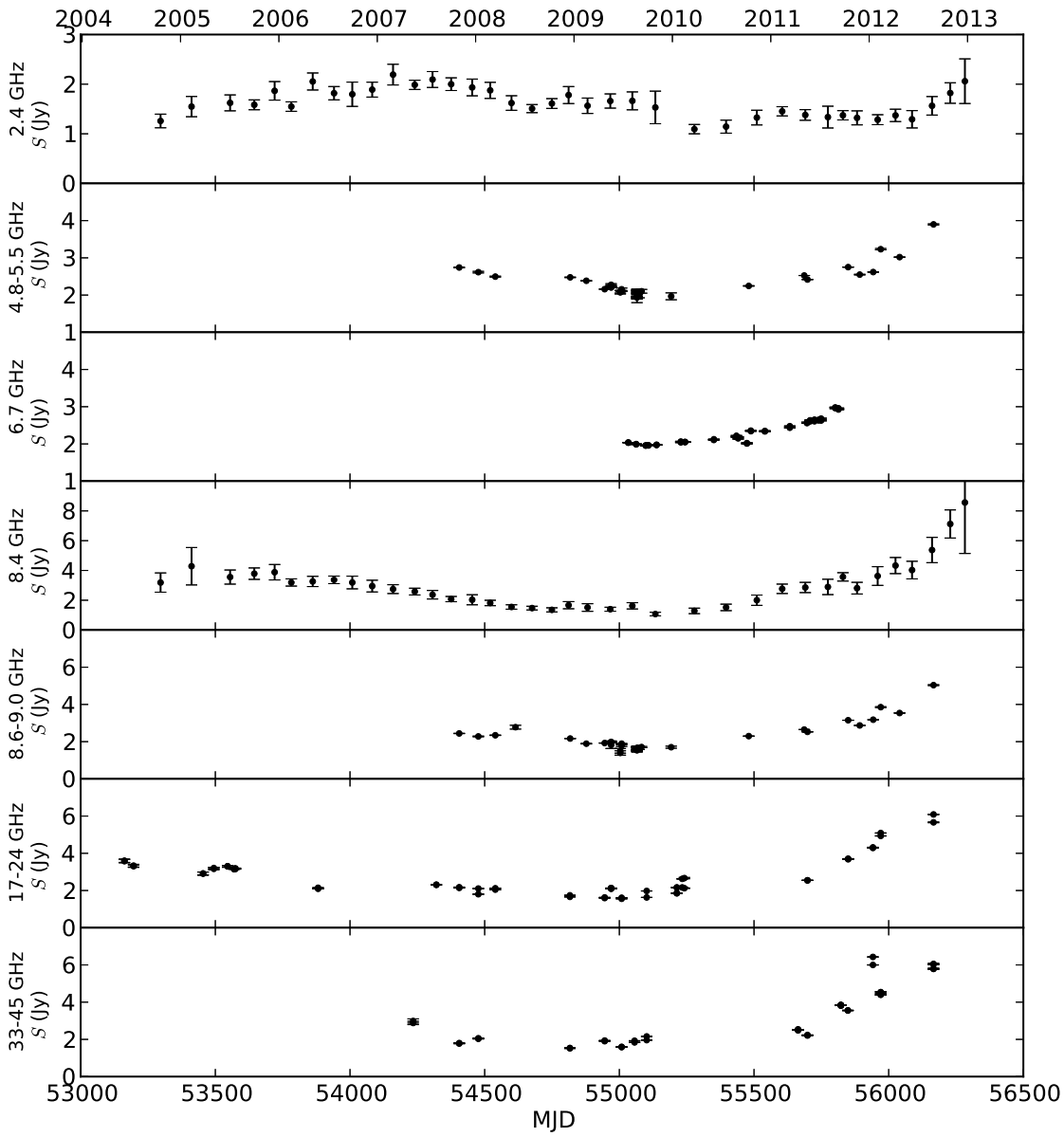

Figure 7.3 Multifrequency monitoring of PKS 1424–418 using the ATCA, Ceduna and the IVS observations. 2.4 and 8.4 GHz observations are IVS data, the 6.7 GHz data are from the Ceduna monitoring, and the rest are from the ATCA.

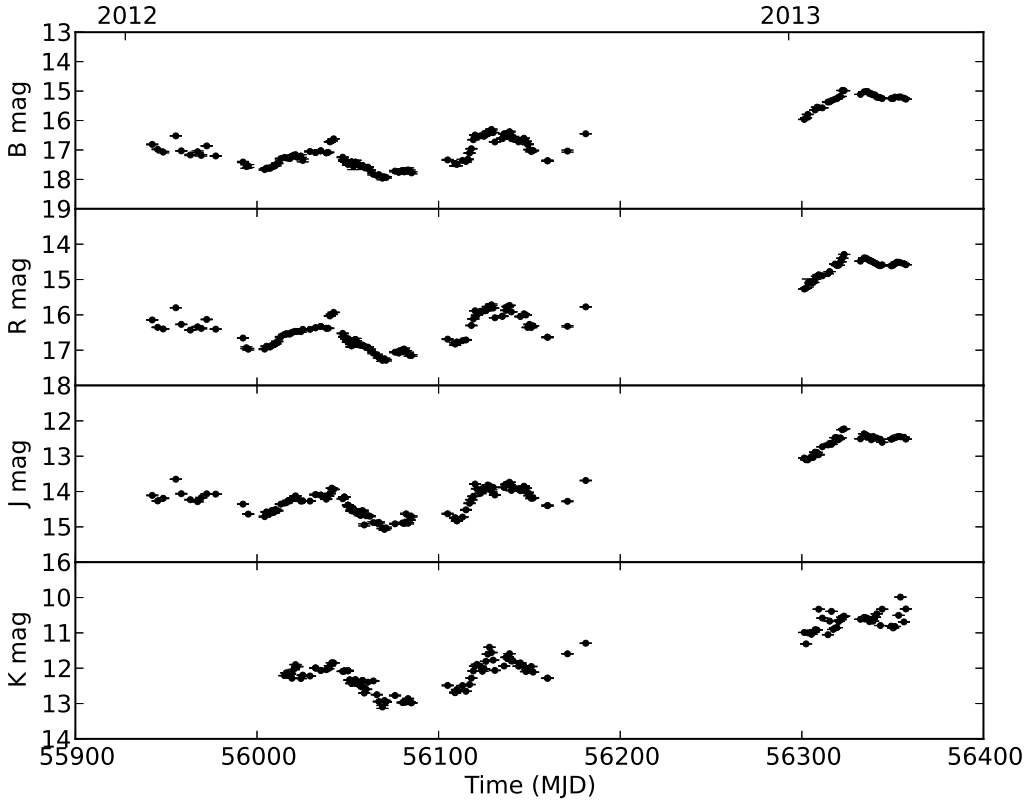

Figure 7.4 Optical monitoring of PKS 1424–418 at B, R, J and K bands using the SMARTS optical telescopes.

7.5, allowing for easier comparison of the flaring behaviours seen at different wavelengths. As can be seen, the optical data follow the gamma-ray data closely, while the radio is undergoing a gentle rise with none of the fine structure seen in both the gamma-ray and optical light curves. Unlike the prior case of PKS 0208–512, PKS 1424–418 shows a gentle, long term rise in the radio preceding the gamma-ray flaring. A gamma-ray flare without associated radio flaring is also observed at around MJD 55300 (2010-04-14).

7.1.5 Cross Correlation Analysis

The analysis outlined in Chapter 5 is then followed. Briefly, the discrete cross correlation function is calculated for all pairs of time series and the resultant lags which pass the significance test are plotted against $\Delta\frac{1}{\nu}$ (Figure 7.6). Again we assume equipartition, that is $\kappa_r = 1$, where κ_r is the ratio of the energy in protons to that in electrons. Again a correlation consistent with optical depth effects is found for the radio data alone (black points on Figure 7.6), such that $Lag = -9.23(\pm 10.3) - 1.16 \times 10^2(\pm 11.2) \times (\frac{1}{\nu_1} - \frac{1}{\nu_2})$, where $\nu_1 > \nu_2$ (positive lag means higher frequencies are leading). However the lags determined from the cross correlations between the radio and higher frequencies are not consistent with optical depth effects (red points on Figure 7.6). In fact these give a negative lag, indicating the radio flare is preceding the gamma-ray. This is consistent with some work in the field suggesting gamma-ray flares occur during the rise time of radio flares (Valtaoja and Terasranta 1995), but does not agree with the model that PKS 0208–512 appears to follow. This could be due to several reasons as follows.

During flaring periods, the optical and gamma-ray emission often shows distinct features, rapid flares over hours or days, often repeating, while the radio emission (particularly at cm wavelengths) is much smoother. In effect, the actual flares in the radio could be 'blurred out' somewhat, where multiple short flares overlap, producing an overall smooth increase in flux density over time. This would then affect the ability to cross match the individual flaring occurring with the gamma-ray/optical flares.

Different emission sites for the radio and gamma-ray/optical emission could also play a part in the lags observed. If the gamma-ray emission is generated further from the core of the AGN, a new jet feature would initially be observed at radio frequencies, requiring some time to propagate outwards along the jet to the gamma-ray emission site hence causing the time lags observed.

This can be generalised to account for both the cases observed, gamma-ray leading radio, and radio leading gamma-ray. In the case of the gamma-ray leading, the emission sites of the radio and gamma-ray radiation would be close enough that optical depth effects dominate (as seen in PKS 0208–512 for example).

The cross correlation between the gamma-ray and optical flux densities (also in red) is consistent with zero lag, as has been seen in other sources (Cook and Carini 2010; Chatterjee et al. 2013), indicating the same emission region.

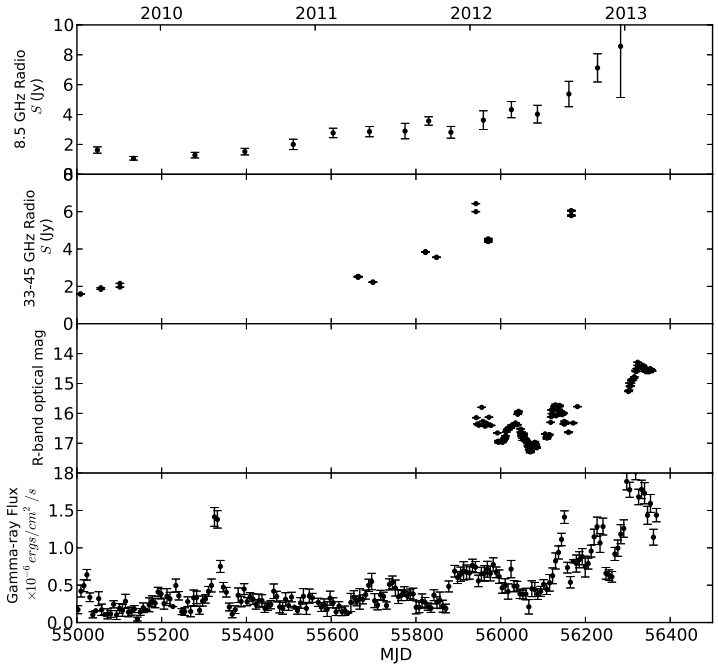

Figure 7.5 8.4 GHz IVS radio flux densities, 33-45 GHz ATCA radio flux densities, Optical R-band flux densities from SMARTS and *Fermi* gamma-ray flux densities of PKS 1424–418 for comparison.

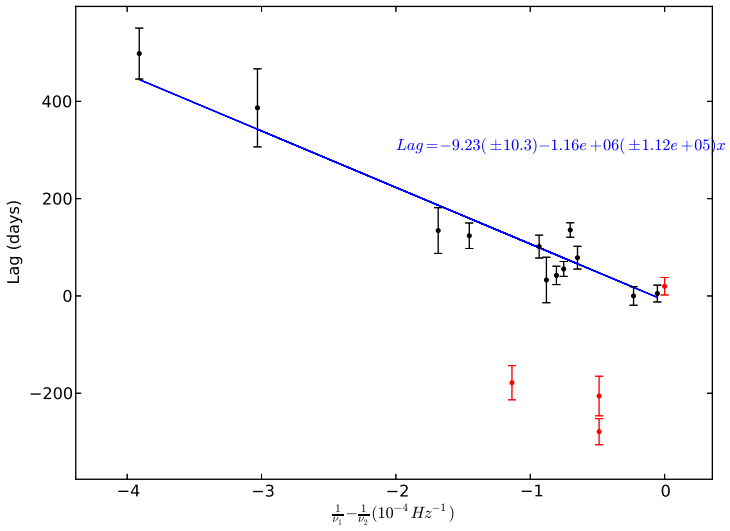

Figure 7.6 The resultant lags from discrete cross correlation analysis performed on all the possible pairs of light curves of PKS 1424–418 for which a significant cross correlation was found, plotted against the change in $\frac{1}{\nu}$. Black points are radio to radio pairs and red points are optical and gamma-ray cross correlations.

7.2 PKS 1622–253

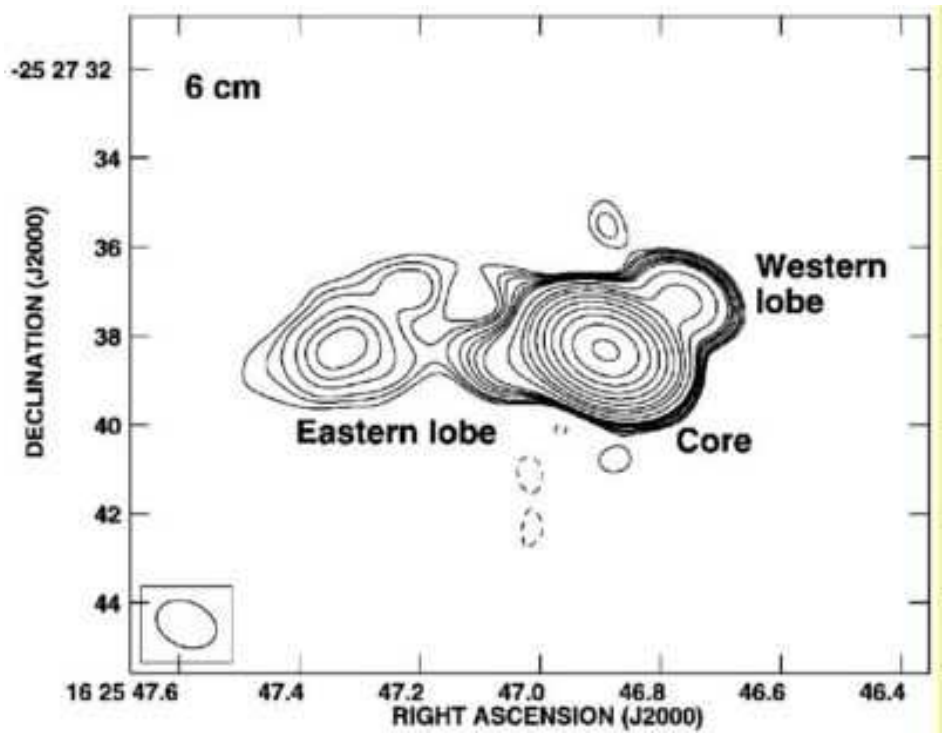

Figure 7.7 6 cm VLA image of PKS 1622–253 from Punsly et al. (2005). Contours are -4, 4, 5, 6, 8, 10, 12, 15, 30, 60, 100, 200, 400, 800, 1600, 3200, and 6400 times 0.25 mJy beam^{-1}, with a peak brightness of 1.84 Jy beam^{-1}.

PKS 1622–253 is a Quasar located at redshift 0.786 (di Serego-Alighieri et al. 1994). The source was detected by EGRET and included in all of the EGRET catalogues (Fichtel et al. 1994; Hartman et al. 1999). This is not a very well known source, due in part to its southern location, but also due to the fact that it lies behind the Ophiuchus molecular gas cloud, making optical observations extremely difficult (Hunter et al. 1994).

7.2.1 VLA Observations

Punsly et al. (2005) undertook an investigation of this source, including VLA observations at both 3.6 and 6 cm. The 6 cm image is shown in Figure 7.7, showing a strong radio core at 1.84 Jy beam^{-1} and both a western and eastern lobe, with the eastern lobe extending out at least 6 arcseconds. They classify the source as a typical triple radio galaxy, with a superluminal core and two lobes showing FRII type morphology, and find equal jet kinematic luminosity and accretion flow bolometric luminosity $\gtrsim 10^{45}$ ergs/sec.

7.2.2 Radio Monitoring

PKS 1622–253 has been part of the Ceduna monitoring project since 2003, and is also a phase calibrator on the ATCA. This makes it a member of the on-going calibration program which provides regular multi frequency flux density observations as a by-product at 1.4, 2.4, 5, 8.8, 20, 39 and 92 GHz. These data are shown in Figure 7.8, as well as both S-band (2.4 GHz) and X-band (8.4 GHz) data taken from the IVS geodetic VLBI observations. PKS 1622–253 is a compact source on VLBI baselines, showing a maximum extension of less than two mas on either side of the core. This makes it an excellent source for the IVS project and as such is a commonly observed source, providing excellent time resolution. The flux density calibration of IVS data is poor, and as such the raw data have been binned adaptively such that each time bin contains 20 points. This smoothes out some of the variability introduced by the lack of flux density calibration in the raw data, and provides a better estimate of the errors. The poor nature of the absolute flux density calibration means the IVS data have not been included in the spectral calculations, although comparing the MOJAVE VLBA core flux density with the X-band IVS data shows a fairly good agreement (see Figure 7.11).

The source is a known scintillator, being part of the Ceduna monitoring program since its inception (McCulloch et al. 2005). Carter et al. (2009) used the Ceduna monitoring to detect an annual cycle for this scintillation. The persistent scintillation may imply microarcsecond structure and high brightness temperature over long time periods.

7.2.3 VLBI

Three epochs of VLBA observations were taken by Jorstad et al. (2001a) over the course of one year. They found a flux density variation of a factor of 5, and detected a single moving component with a superluminal apparent jet speed of 14 c. Their images are shown in Figure 7.9. PKS 1622–253 was part of the MOJAVE monitoring project, before being dropped in 2012 for being too compact. The stacked VLBA image is shown in Figure 7.10, showing a very compact core, with a slight extension to the west and east consistent with the VLA image (Figure 7.7). There are thirteen MOJAVE VLBA observations showing no obvious evolution in the source morphology (Lister et al. 2009). The VLBI core flux density observed during these epochs is in good agreement with the IVS 8.4 GHz flux density presented in Figure 7.8, see Figure 7.11 for a direct comparison. This implies a compact, point-like source with the core flux dominating the emission. Tingay et al. (1996) resolve the core and calculate a brightness temperature of $3 \times 10^{10} K$. The source has been observed using CHI and a brightness temperature of 2×10^{11} K was calculated as shown in Chapter 2.

7.2.4 Radio Cross Correlations

The radio flux density monitoring data shown in Figure 7.8 reveal five flaring periods, and as such the cross correlation analysis has been performed individually for each flare. The data

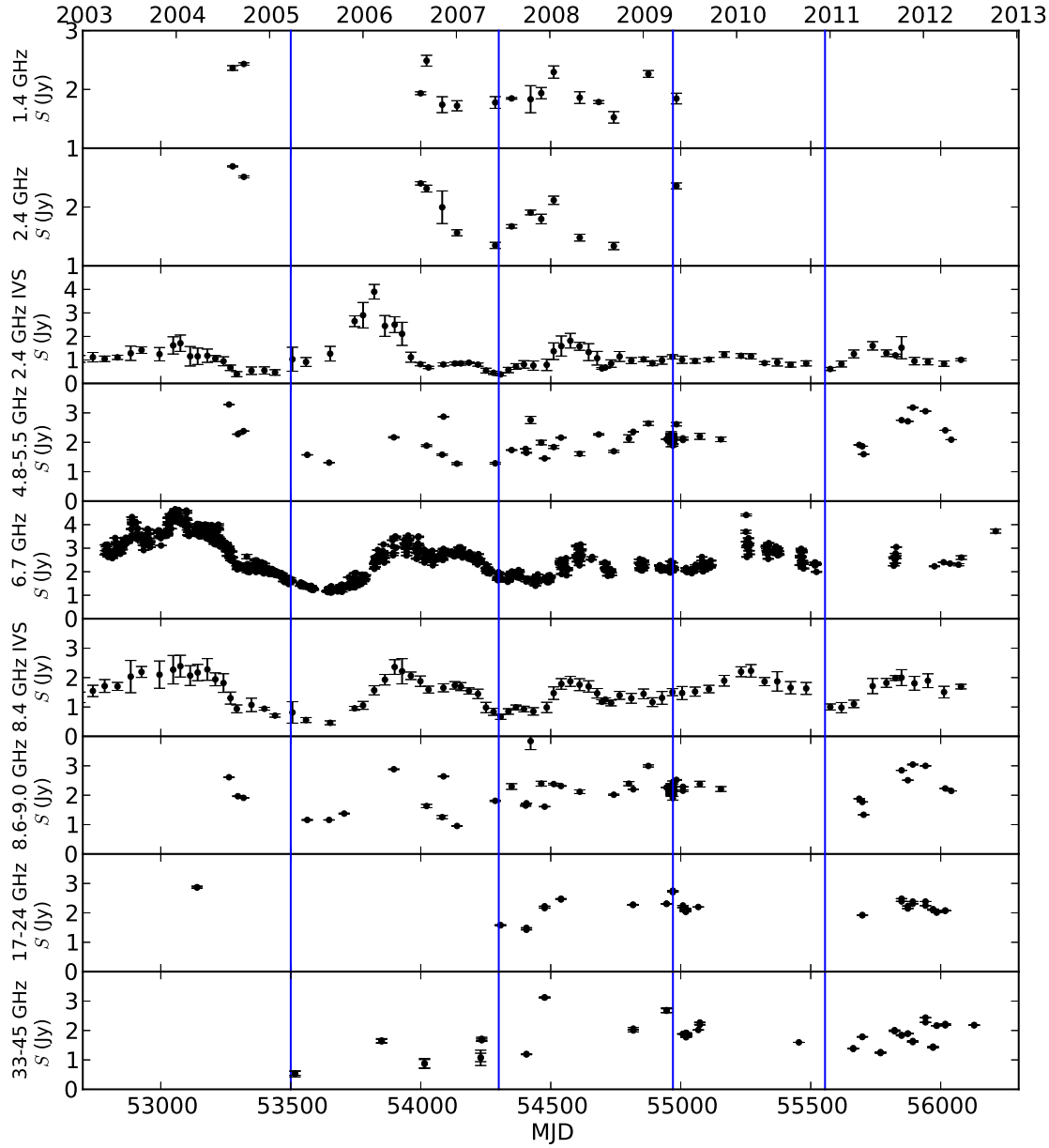

Figure 7.8 Ceduna single dish, ATCA, and IVS observations of PKS 1622–253 at 1.4, 2.4, 5, 8.4, 8.8, 20, 39 and 92 GHz. Five flares are seen during the observing span and the data have been divided into five sections (separated by the vertical lines) to allow for separate cross correlation analysis on each flare.

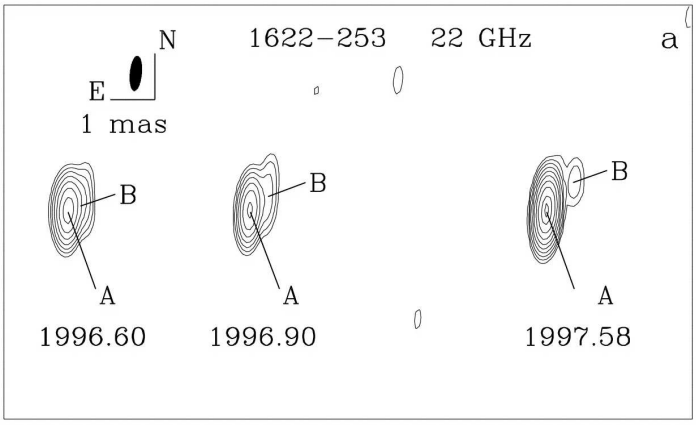

Figure 7.9 Three epochs of VLBA observation of PKS 1622–253 undertaken by Jorstad et al. (2001a), showing evolution of a northwest component (B) at superluminal apparent speed 14 c.

have thus been split into five epochs henceforth referred to as:

- **Flare 1**: all data before MJD 53500.
- **Flare 2**: all data between MJD 53500 and 54300.
- **Flare 3**: all data between MJD 54300 and 54970.
- **Flare 4**: all data between MJD 54970 and 55555.
- **Flare 5**: all data after MJD 55500.

These sections are designated by the vertical lines in Figure 7.8.

It is already evident from a visual inspection of the data that the 2.4 GHz flux density during Flare 2 peaks before the higher frequencies. This is as opposed to Flare 3 for example, during which the flares appear to occur roughly at the same time.

Each flaring period was then analysed following the methods presented in Chapter 5. The resultant lags are shown in Figure 7.12. Note the different slopes of the best fit lines for the lags in flares 2 and 5 (black points) and Flares 1, 3 and 4 (red points), which have slopes of -53.5 ± 3.09 dHz and -30 ± 3.22 dHz respectively, and are statistically different with a confidence level greater than 99.7 %.

It is worth noting that the source flares at low frequencies earlier than at high frequencies. This is inconsistent with the optical depth effect dominated lag seen in the case of PKS 0208–512 and PKS 1424–418. In the case of Flares 2 and 5 this is even more evident. A different effect must be dominating here. As can be seen in Figure 7.12, the slope is mostly caused by the 2.4 GHz (and to some extent the 1.4 GHz) light curve, forming two different 'groups' as opposed to a smooth transition, wheras the lags between flaring times at higher frequencies are consistent with zero lag. It is difficult to propose a mechanism in which the 2.4 GHz data

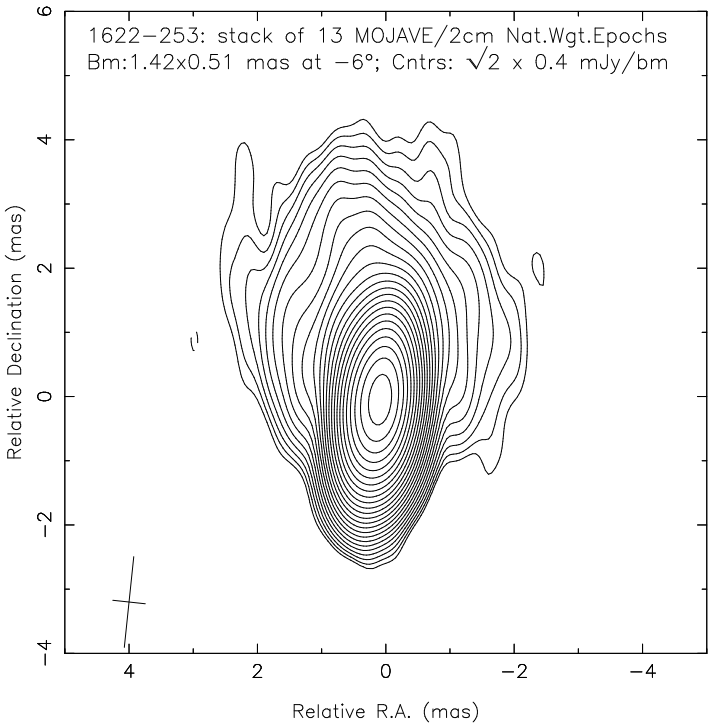

Figure 7.10 Stacked 15 GHz VLBA image of PKS 1622–253 with natural weighting from the MOJAVE monitoring program (Lister et al. 2009).

would be leading the high frequency radio emission. Instrument problems can not fully be dismissed, however no evidence for any issue with the 2.4 GHz data (apart from the poor absolute flux density calibration) has been found, and indeed the light curve (Figure 7.8) agrees well with the other radio lightcurves in the main, apart from the clear lead during Flare 2. It is possible that multiple flares are occurring within a short time period and these flares are merging at lower frequencies where flares often last longer.

7.2.5 Gamma-ray Cross Correlations

PKS 1622–253 was detected as a flaring source by *Fermi*-LAT on Oct 4 2009, with a gamma-ray flux density of $1.9 \pm 0.2 \times 10^{-6}$ photons/cm^2/s (E $>$ 100 MeV), a 17 times increase in flux density compared to its average in the first year of *Fermi* operation (Reyes 2009). This placed it on the *Fermi*-LAT bright monitored blazar list. *Fermi*-LAT again detected flaring activity of the source on June 7 2011, with a gamma-ray flux density of $1.1 \pm 0.3 \times 10^{-6}$ photons/cm^2/s (E $>$ 100 MeV), and remained bright for several days (Curran et al. 2010). A gamma-ray lightcurve for this source has been produced and is presented in Figure 7.13, along with the 2.4 and 8.4 GHz IVS light curves, and the Ceduna 6.7 GHz lightcurve for comparison. Note the possible scintillation during the peaks of the 6.7 GHz light curve. Scintillation requires a compact component and so a new compact component may be emerging from the core, producing both the scintillation and the increase in flux density. This was also noted by

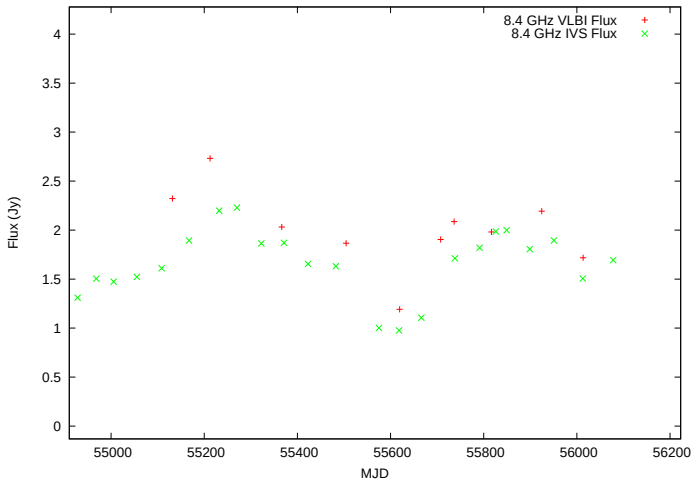

Figure 7.11 Comparison between 8.4 GHz VLBA core flux (red points) and 8.4 GHz IVS flux densities of PKS 1622–253.

Carter et al. (2009) using a shorter (3 years) Ceduna lightcurve.

The gamma-ray lightcurve covers half of flare 3, and flares 4 and 5. From Figure 7.13 it is already clear that the gamma-ray is leading the radio. This is confirmed when cross correlation analysis is performed, resulting in the lags shown in Figure 7.14. Individual flare analysis has been dropped at this point due to the length of the time series involved. The gamma-ray appears to lead the radio by a roughly constant 100 days. That is, the slope of the gamma-ray to radio cross correlations is statistically consistent with being zero. This implies optical depth alone can not account for the origin of the lag, if optical depth effects were the sole reason there would be a smooth trend from low frequency radio all the way through to the gamma-ray (as is seen in PKS 0208–512) not the offset of $\sim$ 100 days.

Although the direction of the lag is opposite to that seen in the case of PKS 1424−418, this further strengthens the premise of multiple emission sites in the jet responsible for flaring at different frequencies. In this case, the gamma-ray being produced close to the radio 'core' (the base of the jet) and the radio flaring occurring downstream.

7.3 PKS 2052–474

PKS 2052–474 is classified as a blazar with a redshift of 1.489 (Healey et al. 2008). It was detected by the TANAMI project in February 2008 at 8.4 GHz with the Australian LBA as a point source with peak flux density 1.51 Jy (Figure 7.15).

7.3.1 Radio Monitoring

The source has been monitored by the Ceduna single dish monitoring program at 6.7 GHz, being initiated in support of TANAMI. PKS 2052–474 is also used as a phase calibrator by the ATCA, as well as being part of the ATCA blazar monitoring program (Stevens et al.

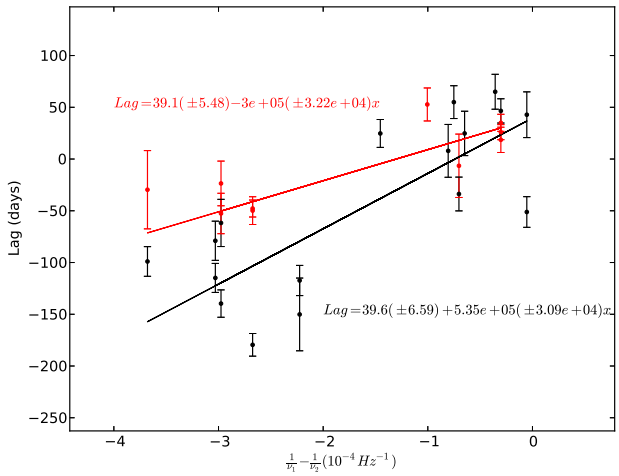

Figure 7.12 Lag vs $\frac{1}{\nu_1} - \frac{1}{\nu_2}$, for PKS 1622–512 black points are flares 2 and 5 and red points are the rest.

2012). PKS 2052–474 is regularly observed in geodetic VLBI observations by the IVS, and the data from those observations have been used in the time series analysis performed here. The IVS data have again been binned adaptively such that each bin contains 20 points, and also are not included in the spectral analysis of the source. This is due to the limited flux density calibration of these data. The absolute flux density of the IVS observations is not highly accurate, see for example the 8.4 GHz flux density shown in Figure 7.16 as compared to the 8.8 GHz data for the same source (same figure) obtained using the ATCA. Considering the flat spectrum of the source (Figure 7.17) the approximately factor of two discrepancy between the lightcurves can not be reconciled. Additionally the VLBI flux, which might be expected to be lower due to only consisting of compact structure, is actually the higher of the two. Fortunately, absolute flux density calibration is not of great importance in this analysis. Rather the errors in Figure 7.16, which are 95 % confident intervals based on the points in each bin, are small enough to easily show deviations from the average flux density. That is, although there is a large systematic error in the IVS data, the random error is small and this is all that is required for the time series analysis as there is a normalisation to average flux density performed as part of the process anyway (see Chapter 5 for a full description).

As mentioned, the radio spectrum of PKS 2052–474 is very flat (Figure 7.17) and is in fact consistent with a spectral index of 0.

7.3.2 SMARTS

This source is also a SMARTS monitored source, and the R band optical data are used here. PKS 2052–474 was seen to be flaring at optical wavelengths using the Automatic Telescope for Optical Monitoring (ATOM) in August 2009, following a gradual increase from an R band magnitude less than 18 to 17.5 in May 2009. The source then showed two minor flares

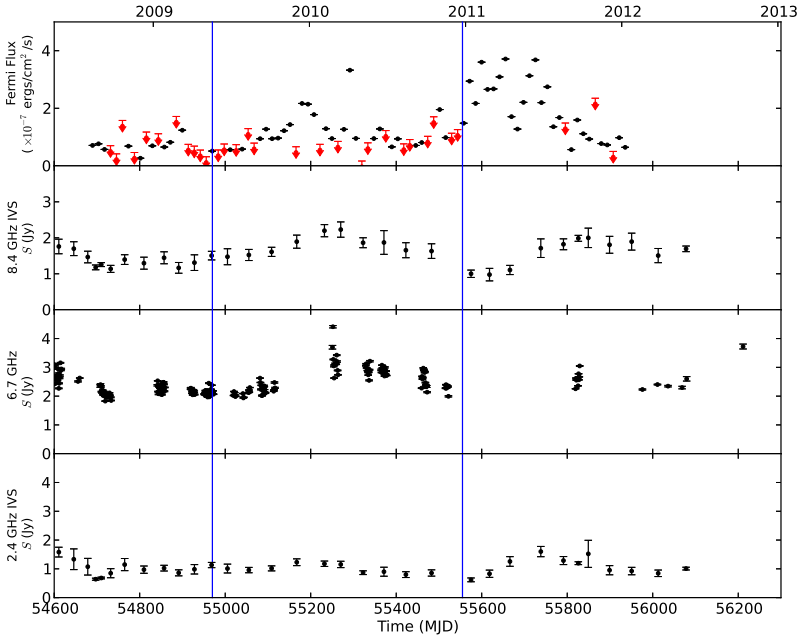

Figure 7.13 *Fermi*-LAT Gamma-ray lightcurve, 8.4 GHz IVS lightcurve, 6.7 GHz Ceduna lightcurve and 2.4 GHz IVS lightcurve of PKS 1622–253. The blue vertical lines mark the beginning of flaring periods 4 and 5. Red points indicate upper limits. Note the rapid flux variations in the 6.7 GHz monitoring data around the time of the gamma-ray flaring. This is scintillation, also evident in how the error size increases during flaring (stronger scintillation increases the error of each bin when the data is averaged).

during June/July before increasing to 15.6 magnitude on Aug 12 2009 (Hauser et al. 2009). *Fermi*-LAT then detected increased gamma-ray emission from the region on Aug 9 2009 with a gamma-ray flux density of $8.7 \pm 1.6 \times 10^{-7}$ photons/cm^2/s, four times higher than the gamma-ray flux density the preceding week (Chang 2009).

7.3.3 *Fermi*

A 7 day binned gamma-ray lightcurve has been produced and is shown in Figure 7.18, along with the SMARTS R band optical monitoring and the most complete radio lightcurves (2.4 and 8.4 GHz IVS data, and the Ceduna 6.7 GHz data). The gamma-ray lightcurve shows a strong flare around MJD 55100, with no associated radio flaring, both the radio and optical data then show a flare nearly a year later, this time with no associated gamma-ray flares.

7.3.4 Cross Correlation Analysis

The cross correlation analysis described in Chapter 5 was performed on these data, and the results are shown in Figure 7.19. The radio to radio cross correlations (black points) are consistent with a zero slope. The optical points are in good agreement with the radio fit,

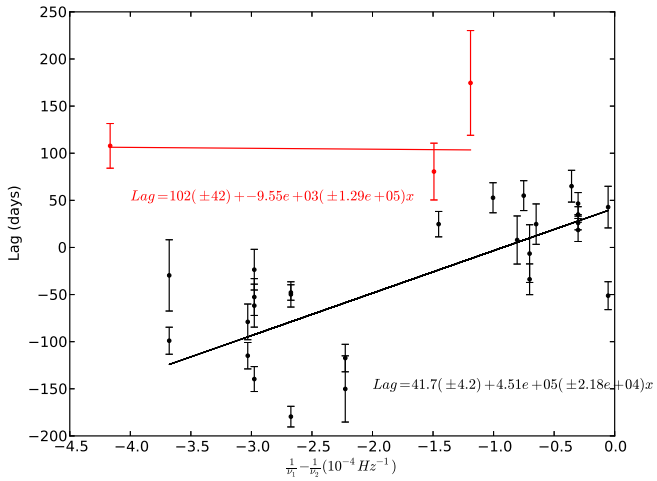

Figure 7.14 Lag vs $\frac{1}{\nu_1} - \frac{1}{\nu_2}$, for PKS 1622–254. Black points are radio to radio cross correlations and red points are gamma-ray to radio cross correlations.

suggesting an optically thin synchrotron flare at MJD $\sim$ 55400 extending from radio all the way to optical wavelengths. The gamma-ray data appear to lead the radio data by 278 $\pm$ 36 days. Gamma-ray to radio delays of this magnitude have been observed previously, for example PKS 0208–512 (see Chapter 5), however in this case it is likely that the gamma-ray flare at MJD 55100 and the radio/optical flare at MJD 55400 are unrelated. Evidence for this is in the optical flaring detected by ATOM described earlier in this chapter. The gamma-ray Flare seen at MJD 55100 was detected at the same time as the optical R band magnitude increased from 17 to 15. This means the optical flaring at MJD 55400 is likely unrelated to the prior gamma-ray flare, which suggests the MJD 55400 flare is another radio to optical flare without associated gamma-ray emission, similar to that seen for PKS 0208–512 in Chapter 5.

Assuming this to be the case leaves an interesting order of events. Initially the source has a bright gamma-ray flare, associated with increased optical emission but no radio flaring. Then, around 280 days later a radio flare is observed, with associated optical flaring but with no associated gamma-ray flaring. Two possible physical interpretations are suggested here:

First, the radio and gamma-ray emission may not be associated in this source at all. The radio/optical flare without gamma-ray emission is likely an increase in the synchrotron generated jet which might not be energetic enough to produce gamma-rays. This leaves the gamma-ray/optical flare difficult to explain however, unless perhaps the brightening seen in optical is dominated by the accretion disk and it is providing the seed photons for the gamma-ray emission.

The second interpretation again involves multiple emission sites. If the gamma-ray emission site is close to the core and the radio emission site is further down the jet, a 280 day delay is conceivable. The optical could flare twice, once during the initial event, and again

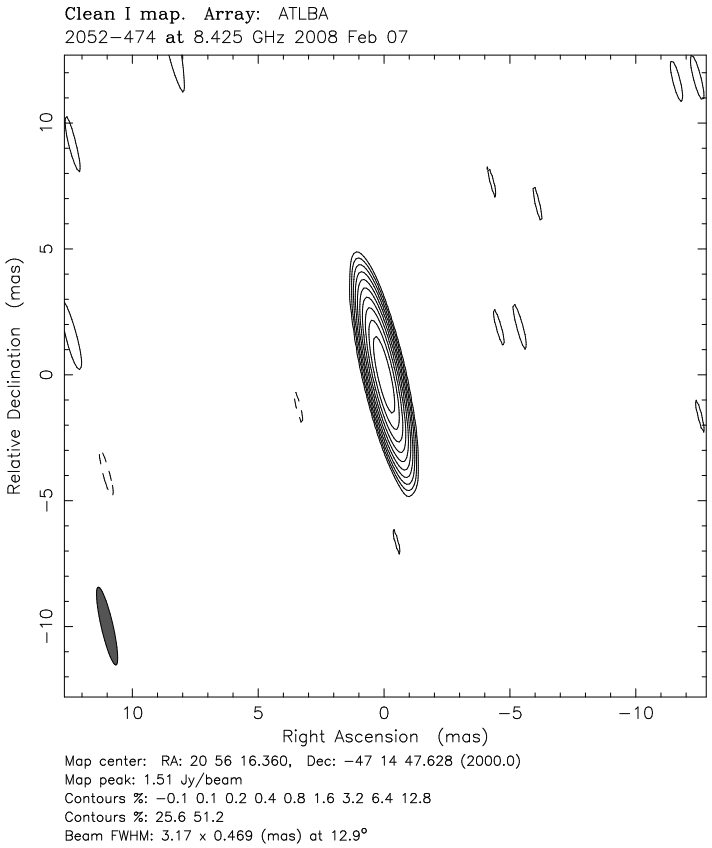

Figure 7.15 VLBI imaging of PKS 2052–474 from TANAMI observations using the Australian LBA.

as the ejected material undergoes a shock producing the radio/optical synchrotron emission.

7.4 Summary

A summary and investigation into how the analysis performed in this chapter fits together with the previous chapters with respect to the physical processes occurring is presented in the Conclusions: Chapter 8.

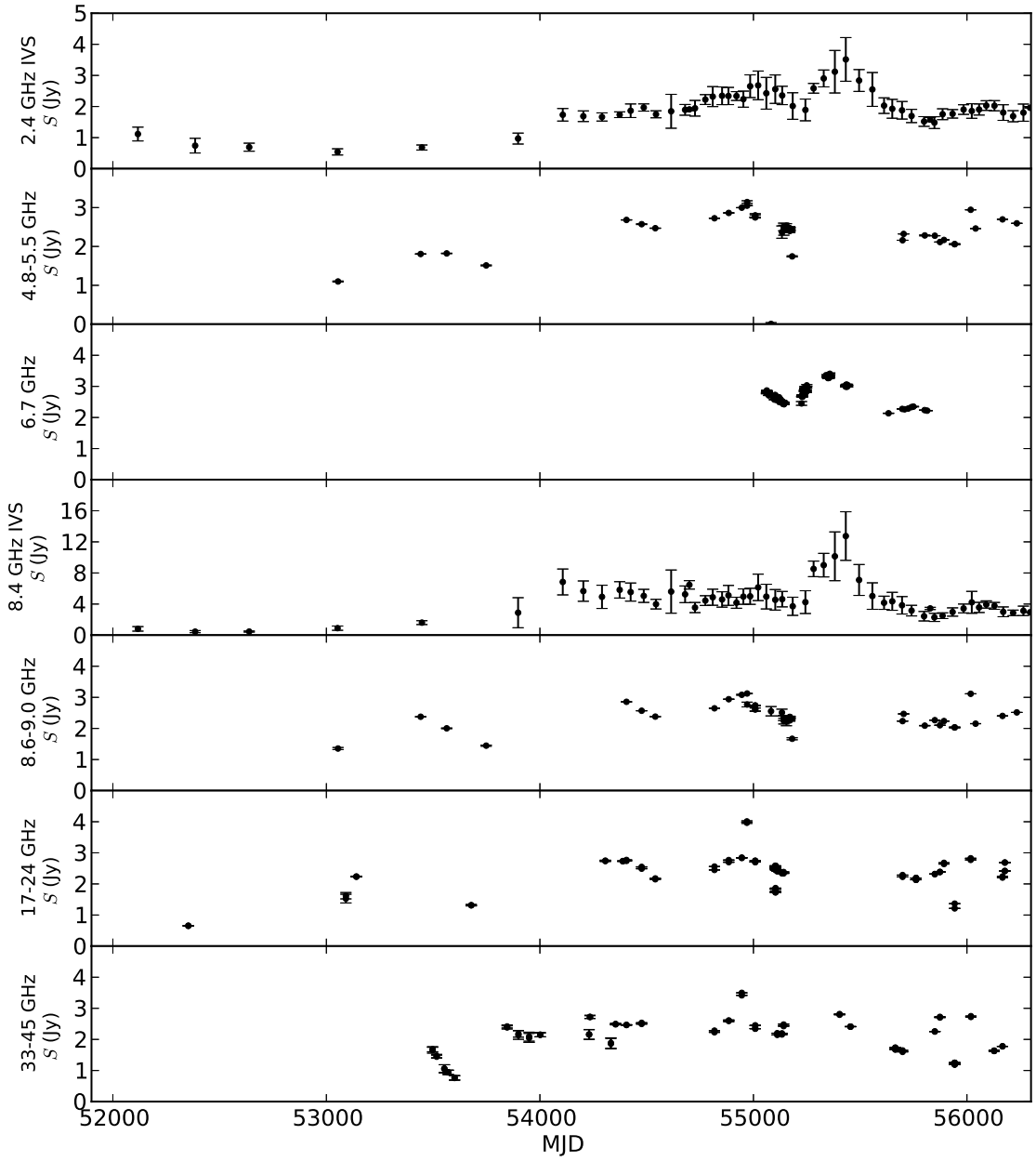

Figure 7.16 2.4, 5.1, 6.7, 8.4, 8.8, 20, and 39 GHz monitoring of PKS 2052–474 from Ceduna single dish, ATCA, and IVS data. Note the absolute flux density offset in the IVS data.

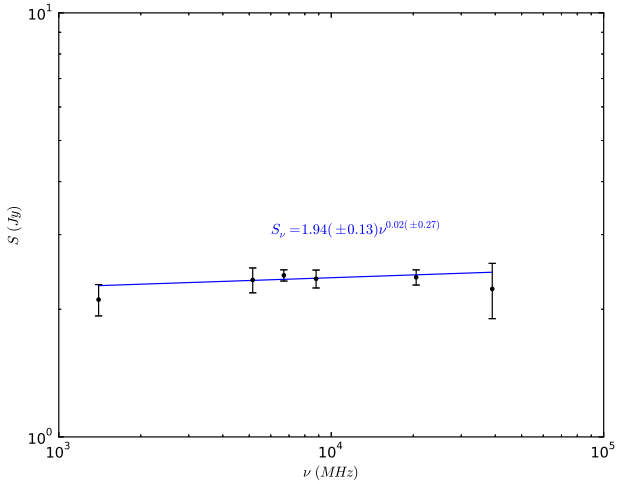

Figure 7.17 Radio Spectrum of PKS 2052–474. IVS data are excluded from these calculations due to their lack of flux density calibration.

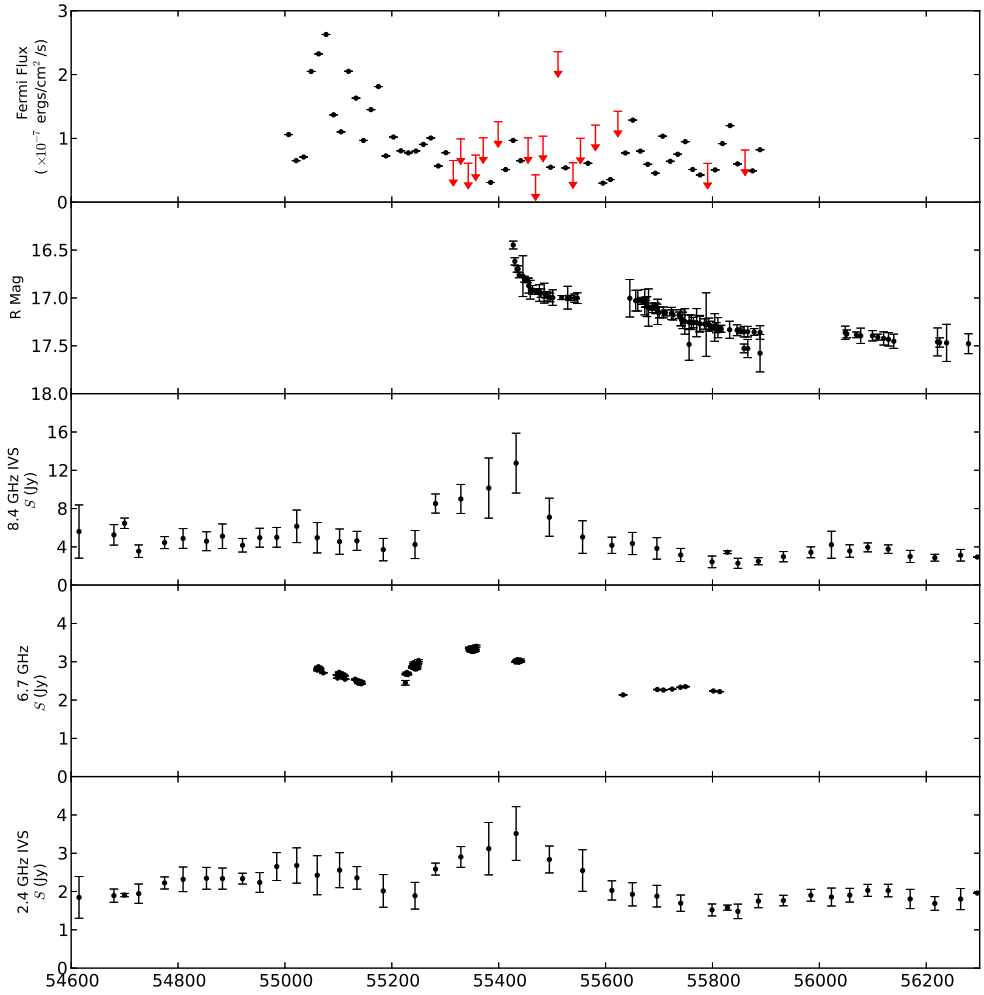

Figure 7.18 *Fermi*-LAT, R band SMARTS, 8.4 and 2.4 GHz IVS and 6.7 GHz Ceduna data of PKS 2052–474 for comparison. Red points indicate upper limits. Note the gamma-ray flare around MJD 55100 without (closely) associated radio flaring, and then the optical and radio flare without associated gamma-ray flaring.

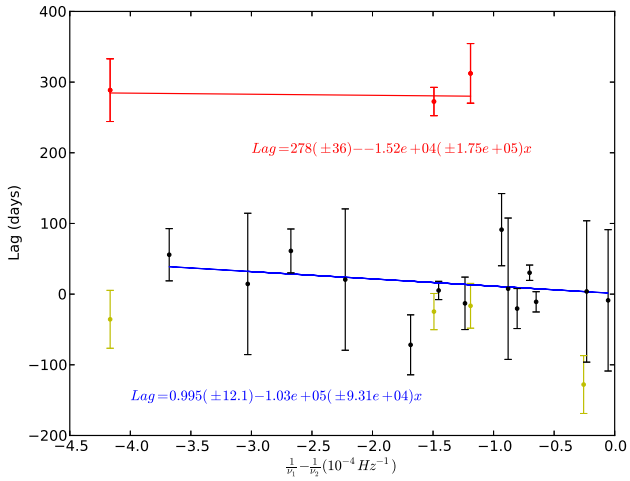

Figure 7.19 The lags vs change in $\frac{1}{\nu}$ between radio wavelengths (black points), radio and gamma-ray wavelengths (red points) and radio and optical wavelengths (yellow points) for PKS 2052–474. No significant correlations between optical and gamma-ray wavelengths were found and as such none are plotted. The blue line is a best fit to the radio to radio cross correlations only. The red line is a best fit to the gamma-ray to radio cross correlations. The radio fit is consistent with an optically thin flare, and there appears to be a 278 day systematic offset to the gamma-ray wavelengths, however the flares responsible for this are thought to not be related.

Chapter 8

Summary and Conclusions

In this thesis, multiple analyses and studies of gamma-ray detected blazars have been presented. In order to understand the physical processes occurring in these highly dynamic evolving objects, multi-frequency, high cadence data are required. It is remarkable that opposite ends of the spectrum hold the key to understanding the emission mechanisms of the AGN in the heart of blazars. The results from EGRET gave a tantalising glimpse, but it is only with the advent of *Fermi* providing all sky monitoring at gamma-ray frequencies, that it has become possible to analyse sources individually. The results of several analyses applied to a small sample of blazars are presented in this thesis, as follows:

- Chapter 1 reviewed the field, and introduced the aims of this thesis.
- Chapter 2 presented the Ceduna–Hobart Interferometer, a single baseline instrument capable of quick turn around target of opportunity flux density measurements of flaring sources in the southern hemisphere. This also detailed the analysis of data on PKS 2052–474, one of the sources included in this thesis.
- Chapter 3 details an investigation into the scintillation properties of gamma-ray detected blazars. Since gamma-ray sources share several characteristics with scintillators it might be expected that they have a similar source population. Some evidence to support this was found, although it is noted that the scintillation survey used is biased towards *Fermi* sources.
- Chapter 4 presented VLBI observations of PKS 0208–512, a southern blazar at redshift 0.999. Six epochs of 8.4 GHz VLBI images were shown and used to calculate an apparent jet speed of $9.3 \pm 0.86c$.
- Chapter 5 presented a cross correlation analysis that was applied to PKS 0208–512 to identify delays between flaring at different frequencies. For this source, the gamma-ray and optical flares were found to be strongly correlated at a lag consistent with zero. The radio emission was found to lag the optical by an amount dependent on the optical

depth of the source. An 'orphan' optical/radio flare, with no associated gamma-ray flaring was also presented and discussed.

- Chapter 6 presented multi epoch spectral energy distribution modelling, that was applied to the PKS 0208–512 data. The two major gamma-ray flares were analysed individually, with separate SEDs being constructed at subpeaks of the major flaring, and contrasted with a quiescent SED calculated for a time period during which the source did not undergo flaring behaviour.

- Chapter 7 presented the application of the same time series analysis methods detailed in Chapter 5 to three further sources, PKS 1424–418, PKS 1622–253 and PKS 2052–474. A variety of source behaviours were found and are discussed further below.

8.1 Physical Processes

In this section, the findings for each individual soure are summarised, and then the entirety are discussed with respect to a physical model of the parsec scale source structure and evolution.

8.1.1 PKS 0208–512

A smooth increase in lag, consistent with being due to optical depth effects, was found for the radio data such that lag increases with increasing difference between frequencies observed. Previous work on the source by Chatterjee et al. (2013) found a strong correlation between the gamma-ray and optical flares with zero lag, and this was confirmed in this thesis, including the addition of another optical/gamma-ray flare. The cross correlation analysis was extended to include the optical data, and both the optical to gamma-ray and radio to optical cross correlations were found to have lags consistent with the optical depth explanation suggested by the radio cross correlations alone, apart from a single flare at radio and optical wavelengths that showed no associated gamma-ray flaring. This 'orphan' flare is proposed to be due to either a change in the magnetic field strength only, or an emission located further 'down' the jet (Chapter 5).

The smooth correlation between lag and difference in frequency was used to calculate an expected delay of 121 days between a gamma-ray flare, and a radio flare at 8.4 GHz. Using the apparent jet speed calculated in Chapter 4, this delay corresponds to an apparent angular separation of 0.12 mas, beyond the current resolution limit of VLBI.

The SED modelling applied to PKS 0208–512 suggests a relatively small emission zone, with an initial drop in magnetic field strength as the flare begins, followed by an increase in size of the emission region and an increase in magnetic field strength as the flare tails off. The major emission mechanisms involved are synchrotron for the radio and optical, and inverse Compton dominated by seed photons from the dusty torus. Synchrotron self-Comptonisation

was not found to be a major contributor to the emission from PKS 0208–512. This is the subject of further work (see below).

These results point towards a source in which the gamma-ray and optical emission is originating in a compact region near the core of the AGN, which propogates outwards and expands until it is optically thin at radio wavelengths and a radio flare is seen. The orphan radio/optical flare could be a shock occurring further along the jet, producing no gamma-ray flare either due to its distance from the dusty torus seed photon population, or due to a lack of energy in the shock. It is also possible that this flare is caused by a change in magnetic field strength alone, which also would not produce gamma-ray emission. Unfortunately no SED modelling of the orphan flare was undertaken. The SED modelling was begun prior to the time series analysis, and the periods targeted for SED fitting were based on gamma-ray flaring.

8.1.2 PKS 1424–418

The same time series analysis that was applied to PKS 0208–512 was used on PKS 1424–418. Again, the radio data show a smooth correlation between lag and change in frequency, consistent with optical depth effects. The gamma-ray to optical cross correlation is again found to be consistent with zero lag. However, the lags determined from cross correlations between radio to optical and radio to gamma-ray are not consistent with optical depth being the major cause. The gamma-ray emission is actually seen to flare after the radio, as was suggested for some sources in the EGRET era (Valtaoja and Terasranta 1995).

It is possible that the flares at different frequencies have not been crossmatched correctly, as flares occurring at centimetre wavelengths can sometime merge, producing what appears to be a single, strong flare peaking at a time somewhere in between the two sub-flares.

The other explanation relies on different emission sites for the optical/gamma-ray and radio flaring. In this case the gamma-ray emission would need to be further from the core of the AGN.

8.1.3 PKS 1622–253

Again cross correlation analysis was applied to this source. PKS 1622–253 showed 5 individual radio flares during the observing period and each was analysed individually. The radio to radio cross correlations show a lag in which low frequencies are flaring first, however this is dominated by cross correlations to the 2.4 GHz radio data. While there is no known reason to be distrustful of these data, a scenario in which low radio frequencies flare (in some cases as much as 150 days) prior to higher radio frequencies is difficult to explain.

Gamma-ray flares from this source appear to lead the radio flaring by roughly 100 days but are not consistent with optical depth being the primary cause. Separate emission sites could well explain this lag with, in this case, the gamma-ray flare originating closer to the core of the AGN than the radio.

The source is a known scintillator and scintillation appears to be related to flaring activity. Since scintillation requires a compact, bright component, this could indicate a new component preceding flaring events. A thorough analysis of the scintillation of this source is the subject of further work.

8.1.4 PKS 2052–474

The last source for which cross correlation analysis was applied is PKS 2052-474. The radio to radio cross correlations are consistent with zero lag, suggesting the radio flare is occurring at an optically thin part of the jet. The radio to optical cross correlations are in good agreement with this model, also showing zero lag to the radio. The gamma-ray flaring appears to precede that at other wavelengths by roughly 280 days, however previous optical studies during the gamma-ray flare showed correlated optical emission at zero lag (as is the case for flares in other sources in this thesis). As such it is unlikely that the radio and gamma-ray flares are associated in this case.

This leaves a radio/optical flare without associated gamma-ray emission, similar to the case seen in PKS 0208–512. It is possible that the radio and gamma-ray flaring seen in this source is not associated at all, with the radio/optical emission being generated by a change in the magnetic field strength only, not enough to produce gamma-ray emission, or so far down the jet that no suitable seed photons for the gamma-ray emission exist. The other explanation requires multiple emission sites. The gamma-ray flaring could be generated closer to the core of the AGN and the radio/optical in a shock further along the jet. The optical could flare twice, once during the inital event (the gamma-ray flare), and again as the ejected material reaches the shocked region.

8.1.5 Overall Model

Although a relatively small number of blazars were studied, a large variety of behaviour was observed. Clearly optical depth plays a large role in the time lags between radio and gamma-ray emission, however it is not the only effect taking place. It appears likely that multiple emission sites are required to fully explain the behaviour seen in these objects. This can be generalised as follows:

An initial ejection of new material from the core of the AGN produces either a radio/optical synchrotron flare, or a gamma-ray/optical flare. In the first case, no gamma-ray flaring might be observed at all, or a gamma-ray flare might be observed as the material propogates down the jet, perhaps in a shocked region (PKS 1424–418). In the latter case, a strong gamma-ray flare is immediately observed, either with optical and radio flares appearing as dictated by optical depth effects, or occurring later, further along the jet.

It is clear that there is no single mechanism dominating the time delay between radio and gamma-ray flares in all sources.

8.2 Further Work

Work on modelling the SEDs of PKS 1424–418, PKS 1622–253 and PKS 2052–474 may provide further insight into the physical processes occurring, as will modelling of the 'orphan' radio/optical flare in PKS 0208–512.

Additionally, a thorough investigation into the relationship between scintillation and gamma-ray flaring for individual sources is planned. This will be a targeted analysis on sources like PKS 1622–253, which show regular flaring and scintillating behaviour. It is hoped that the scintillation will provide evidence of micro arcsecond scale changes in the cores of blazars, prior to, or in association with flaring.

Further sources will be analysed using the methods detailed in this thesis as their lightcurves become long enough for sufficient flaring to be observed at multiple frequencies. The monitoring using the Ceduna 30 m telescope and CHI is in the process of being expanded to include more frequencies, which will provide greater coverage of radio flares at multiple frequencies.

Clearly the emission processes occurring in blazars are complicated in nature, showing a wide range of behaviour. Millimetre and sub millimetre radio monitoring tends to be more closely correlated with gamma-ray flaring and so the work being done by APEX is of high importance. Modelling of SEDs while taking into account the lag between flaring events could also allow for the inclusion of the centimetre wavelength radio data in the model. This should provide a more cohesive picture of the changing spectral energy distribution of these sources.

Bibliography

A. A. Abdo, M. Ackermann, M. Ajello, E. Antolini, L. Baldini, J. Ballet, G. Barbiellini, D. Bastieri, K. Bechtol, R. Bellazzini, B. Berenji, R. D. Blandford, E. D. Bloom, E. Bonamente, A. W. Borgland, A. Bouvier, J. Bregeon, A. Brez, M. Brigida, P. Bruel, R. Buehler, T. H. Burnett, S. Buson, G. A. Caliandro, R. A. Cameron, P. A. Caraveo, S. Carrigan, J. M. Casandjian, E. Cavazzuti, C. Cecchi, Ö. Çelik, A. Chekhtman, C. C. Cheung, J. Chiang, S. Ciprini, R. Claus, J. Cohen-Tanugi, L. R. Cominsky, J. Conrad, L. Costamante, S. Cutini, C. D. Dermer, A. de Angelis, F. de Palma, E. d. C. e. Silva, P. S. Drell, R. Dubois, D. Dumora, C. Farnier, C. Favuzzi, S. J. Fegan, W. B. Focke, P. Fortin, M. Frailis, Y. Fukazawa, S. Funk, P. Fusco, F. Gargano, D. Gasparrini, N. Gehrels, S. Germani, B. Giebels, N. Giglietto, P. Giommi, F. Giordano, T. Glanzman, G. Godfrey, I. A. Grenier, M.-H. Grondin, J. E. Grove, S. Guiriec, D. Hadasch, M. Hayashida, E. Hays, S. E. Healey, D. Horan, R. E. Hughes, R. Itoh, G. Jóhannesson, A. S. Johnson, W. N. Johnson, T. Kamae, H. Katagiri, J. Kataoka, N. Kawai, J. Knödlseder, M. Kuss, J. Lande, S. Larsson, L. Latronico, M. Lemoine-Goumard, F. Longo, F. Loparco, B. Lott, M. N. Lovellette, P. Lubrano, G. M. Madejski, A. Makeev, E. Massaro, M. N. Mazziotta, J. E. McEnery, P. F. Michelson, W. Mitthumsiri, T. Mizuno, A. A. Moiseev, C. Monte, M. E. Monzani, A. Morselli, I. V. Moskalenko, M. Mueller, S. Murgia, P. L. Nolan, J. P. Norris, E. Nuss, M. Ohno, T. Ohsugi, N. Omodei, E. Orlando, J. F. Ormes, M. Ozaki, J. H. Panetta, D. Parent, V. Pelassa, M. Pepe, M. Pesce-Rollins, F. Piron, T. A. Porter, S. Rainò, R. Rando, M. Razzano, A. Reimer, O. Reimer, S. Ritz, A. Y. Rodriguez, R. W. Romani, M. Roth, F. Ryde, H. F.-W. Sadrozinski, A. Sander, J. D. Scargle, C. Sgrò, M. S. Shaw, P. D. Smith, G. Spandre, P. Spinelli, J.-L. Starck, M. S. Strickman, D. J. Suson, H. Takahashi, T. Takahashi, T. Tanaka, J. B. Thayer, J. G. Thayer, D. J. Thompson, L. Tibaldo, D. F. Torres, G. Tosti, A. Tramacere, Y. Uchiyama, T. L. Usher, V. Vasileiou, N. Vilchez, V. Vitale, A. P. Waite, E. Wallace, P. Wang, B. L. Winer, K. S. Wood, Z. Yang, T. Ylinen, and M. Ziegler. Gamma-ray Light Curves and Variability of Bright Fermi-detected Blazars. *Astrophys. Journal*, 722:520–542, October 2010. doi: 10.1088/0004-637X/722/1/520.

K.D. Abhyankar. *Astrophysics: Stars and Galaxies*. Universities Press (India) Pvt. Limited, 2002. ISBN 9788173713811. URL `http://books.google.com.au/books?id=fJMwrULu2E0C`.

M. A. Abramowicz and P. C. Fragile. Foundations of Black Hole Accretion Disk Theory. *Living Reviews in Relativity*, 16:1, January 2013.

I. Agudo, S. G. Jorstad, A. P. Marscher, V. M. Larionov, J. L. Gómez, A. Lähteenmäki, M. Gurwell, P. S. Smith, H. Wiesemeyer, C. Thum, J. Heidt, D. A. Blinov, F. D. D'Arcangelo, V. A. Hagen-Thorn, D. A. Morozova, E. Nieppola, M. Roca-Sogorb, G. D. Schmidt, B. Taylor, M. Tornikoski, and I. S. Troitsky. Location of γ-ray Flare Emission in the Jet of the BL Lacertae Object OJ287 More than 14 pc from the Central Engine. *Astrophys. Journal Letters*, 726:L13+, January 2011. doi: 10.1088/2041-8205/726/1/L13.

R. Antonucci. Unified models for active galactic nuclei and quasars. *Ann. Rev. Astron. and Astrophys.*, 31:473–521, 1993. doi: 10.1146/annurev.aa.31.090193.002353.

A. L. Argon, L. J. Greenhill, M. J. Reid, J. M. Moran, and E. M. L. Humphreys. Toward a New Geometric Distance to the Active Galaxy NGC 4258. I. VLBI Monitoring of Water Maser Emission. *Astrophys. Journal*, 659:1040–1062, April 2007. doi: 10.1086/512718.

H. Arp. Additional members of the Local Group of galaxies and quantized redshifts within the two nearest groups. *Journal of Astrophysics and Astronomy*, 8:241–255, September 1987. doi: 10.1007/BF02715046.

W. B. Atwood, A. A. Abdo, M. Ackermann, W. Althouse, B. Anderson, M. Axelsson, L. Baldini, J. Ballet, D. L. Band, G. Barbiellini, J. Bartelt, D. Bastieri, B. M. Baughman, K. Bechtol, D. Bédérède, F. Bellardi, R. Bellazzini, B. Berenji, G. F. Bignami, D. Bisello, E. Bissaldi, R. D. Blandford, E. D. Bloom, J. R. Bogart, E. Bonamente, J. Bonnell, A. W. Borgland, A. Bouvier, J. Bregeon, A. Brez, M. Brigida, P. Bruel, T. H. Burnett, G. Busetto, G. A. Caliandro, R. A. Cameron, P. A. Caraveo, S. Carius, P. Carlson, J. M. Casandjian, E. Cavazzuti, M. Ceccanti, C. Cecchi, E. Charles, A. Chekhtman, C. C. Cheung, J. Chiang, R. Chipaux, A. N. Cillis, S. Ciprini, R. Claus, J. Cohen-Tanugi, S. Condamoor, J. Conrad, R. Corbet, L. Corucci, L. Costamante, S. Cutini, D. S. Davis, D. Decotigny, M. DeKlotz, C. D. Dermer, A. de Angelis, S. W. Digel, E. do Couto e Silva, P. S. Drell, R. Dubois, D. Dumora, Y. Edmonds, D. Fabiani, C. Farnier, C. Favuzzi, D. L. Flath, P. Fleury, W. B. Focke, S. Funk, P. Fusco, F. Gargano, D. Gasparrini, N. Gehrels, F.-X. Gentit, S. Germani, B. Giebels, N. Giglietto, P. Giommi, F. Giordano, T. Glanzman, G. Godfrey, I. A. Grenier, M.-H. Grondin, J. E. Grove, L. Guillemot, S. Guiriec, G. Haller, A. K. Harding, P. A. Hart, E. Hays, S. E. Healey, M. Hirayama, L. Hjalmarsdotter, R. Horn, R. E. Hughes, G. Jóhannesson, G. Johansson, A. S. Johnson, R. P. Johnson, T. J. Johnson, W. N. Johnson, T. Kamae, H. Katagiri, J. Kataoka, A. Kavelaars, N. Kawai, H. Kelly, M. Kerr, W. Klamra, J. Knödlseder, M. L. Kocian, N. Komin, F. Kuehn, M. Kuss, D. Landriu, L. Latronico, B. Lee, S.-H. Lee, M. Lemoine-Goumard, A. M. Lionetto, F. Longo, F. Loparco, B. Lott, M. N. Lovellette, P. Lubrano, G. M. Madejski, A. Makeev, B. Marangelli, M. M. Massai, M. N. Mazziotta, J. E. McEnery, N. Menon,

C. Meurer, P. F. Michelson, M. Minuti, N. Mirizzi, W. Mitthumsiri, T. Mizuno, A. A. Moiseev, C. Monte, M. E. Monzani, E. Moretti, A. Morselli, I. V. Moskalenko, S. Murgia, T. Nakamori, S. Nishino, P. L. Nolan, J. P. Norris, E. Nuss, M. Ohno, T. Ohsugi, N. Omodei, E. Orlando, J. F. Ormes, A. Paccagnella, D. Paneque, J. H. Panetta, D. Parent, M. Pearce, M. Pepe, A. Perazzo, M. Pesce-Rollins, P. Picozza, L. Pieri, M. Pinchera, F. Piron, T. A. Porter, L. Poupard, S. Rainò, R. Rando, E. Rapposelli, M. Razzano, A. Reimer, O. Reimer, T. Reposeur, L. C. Reyes, S. Ritz, L. S. Rochester, A. Y. Rodriguez, R. W. Romani, M. Roth, J. J. Russell, F. Ryde, S. Sabatini, H. F.-W. Sadrozinski, D. Sanchez, A. Sander, L. Sapozhnikov, P. M. S. Parkinson, J. D. Scargle, T. L. Schalk, G. Scolieri, C. Sgrò, G. H. Share, M. Shaw, T. Shimokawabe, C. Shrader, A. Sierpowska-Bartosik, E. J. Siskind, D. A. Smith, P. D. Smith, G. Spandre, P. Spinelli, J.-L. Starck, T. E. Stephens, M. S. Strickman, A. W. Strong, D. J. Suson, H. Tajima, H. Takahashi, T. Takahashi, T. Tanaka, A. Tenze, S. Tether, J. B. Thayer, J. G. Thayer, D. J. Thompson, L. Tibaldo, O. Tibolla, D. F. Torres, G. Tosti, A. Tramacere, M. Turri, T. L. Usher, N. Vilchez, V. Vitale, P. Wang, K. Watters, B. L. Winer, K. S. Wood, T. Ylinen, and M. Ziegler. The Large Area Telescope on the Fermi Gamma-Ray Space Telescope Mission. *Astrophys. Journal*, 697:1071–1102, June 2009. doi: 10.1088/0004-637X/697/2/1071.

W. Baade and R. Minkowski. Identification of the Radio Sources in Cassiopeia, Cygnus a, and Puppis a. *Astrophys. Journal*, 119:206, January 1954. doi: 10.1086/145812.

S. A. Balbus and J. F. Hawley. A powerful local shear instability in weakly magnetized disks. I - Linear analysis. II - Nonlinear evolution. *Astrophys. Journal*, 376:214–233, July 1991. doi: 10.1086/170270.

H. E. Bignall, D. L. Jauncey, J. E. J. Lovell, A. K. Tzioumis, L. Kedziora-Chudczer, J.-P. Macquart, S. J. Tingay, D. P. Rayner, and R. W. Clay. Rapid Variability and Annual Cycles in the Characteristic Timescale of the Scintillating Source PKS 1257-326. *Astrophys. Journal*, 585:653–664, March 2003. doi: 10.1086/346180.

J. M. Blanchard, J. E. J. Lovell, R. Ojha, M. Kadler, J. M. Dickey, and P. G. Edwards. High resolution rapid response observations of compact radio sources with the Ceduna Hobart Interferometer (CHI). *Astron. and Astrophys.*, 538:A150, February 2012. doi: 10.1051/0004-6361/201117593.

R. D. Blandford and A. Königl. Relativistic jets as compact radio sources. *Astrophys. Journal*, 232:34–48, August 1979. doi: 10.1086/157262.

S. D. Bloom and A. P. Marscher. An Analysis of the Synchrotron Self-Compton Model for the Multi–Wave Band Spectra of Blazars. *Astrophys. Journal*, 461:657–+, April 1996. doi: 10.1086/177092.

M. Boettcher. Models for the Spectral Energy Distributions and Variability of Blazars. *ArXiv e-prints*, June 2010.

J. G. Bolton. The Fortieth Anniversary of Extragalactic Radio Astronomy - Radiophysics in Exile. *Proceedings of the Astronomical Society of Australia*, 8:381, 1990.

E. Bonning, C. M. Urry, C. Bailyn, M. Buxton, R. Chatterjee, P. Coppi, G. Fossati, J. Isler, and L. Maraschi. SMARTS Optical and Infrared Monitoring of 12 Gamma-Ray Bright Blazars. *Astrophys. Journal*, 756:13, September 2012. doi: 10.1088/0004-637X/756/1/13.

E. W. Bonning, L. Cheng, G. A. Shields, S. Salviander, and K. Gebhardt. Accretion Disk Temperatures and Continuum Colors in QSOs. *Astrophys. Journal*, 659:211–217, April 2007. doi: 10.1086/510712.

M. Böttcher. Modeling the emission processes in blazars. *Astrophys. and Space Science*, 309: 95–104, June 2007. doi: 10.1007/s10509-007-9404-0.

F. H. Briggs. Coherence time for 430-MHz VLBI. *Astron. Journal*, 88:239–242, February 1983. doi: 10.1086/113312.

J. H. Buckley, C. W. Akerlof, S. Biller, D. A. Carter-Lewis, M. Catanese, M. F. Cawley, V. Connaughton, D. J. Fegan, J. P. Finley, J. Gaidos, A. M. Hillas, J. F. Kartje, A. Koenigl, F. Krennrich, R. C. Lamb, R. Lessard, D. J. Macomb, J. R. Mattox, J. E. McEnery, G. Mohanty, J. Quinn, A. J. Rodgers, H. J. Rose, M. S. Schubnel, G. Sembroski, P. S. Smith, T. C. Weekes, C. Wilson, and J. Zweerink. Gamma-Ray Variability of the BL Lacertae Object Markarian 421. *Astrophys. Journal Letters*, 472:L9+, November 1996. doi: 10.1086/310352.

A. M. Burgess and R. W. Hunstead. The Molonglo Southern 4 Jy Sample (MS4). II. ATCA Imaging and Optical Identification. *Astron. Journal*, 131:114–132, January 2006. doi: 10.1086/498679.

S. J. B. Carter, S. P. Ellingsen, J.-P. Macquart, and J. E. J. Lovell. Annual cycles in the interstellar scintillation time-scales of PKSB1519-273 and PKSB1622-253. *Mon. Not. R. Atron. Soc.*, 396:1222–1230, July 2009. doi: 10.1111/j.1365-2966.2009.14824.x.

C. S. Chang. Fermi LAT detection of increasing gamma-ray activity of blazar PKS 2052-474. *The Astronomer's Telegram*, 2160:1, August 2009.

C. S. Chang, E. Ros, M. Kadler, R. Ojha, the Fermi Lat Collaboration, the Tanami Team, and the F-Gamma Team. Multiwavelength campaign of the gamma-ray flaring source PKS 2052-47. *ArXiv e-prints 1001.1563*, January 2010.

R. Chatterjee, S. G. Jorstad, A. P. Marscher, H. Oh, I. M. McHardy, M. F. Aller, H. D. Aller, T. J. Balonek, H. R. Miller, W. T. Ryle, G. Tosti, O. Kurtanidze, M. Nikolashvili, V. M. Larionov, and V. A. Hagen-Thorn. Correlated Multi-Wave Band Variability in the Blazar 3C 279 from 1996 to 2007. *Astrophys. Journal*, 689:79–94, December 2008. doi: 10.1086/592598.

R. Chatterjee, G. Fossati, C. M. Urry, C. D. Bailyn, L. Maraschi, M. Buxton, E. W. Bonning, J. Isler, and P. Coppi. An Optical-Near-infrared Outburst with no Accompanying γ-Rays in the Blazar PKS 0208-512. *Astrophys. Journal Letters*, 763:L11, January 2013. doi: 10.1088/2041-8205/763/1/L11.

G. Chincarini, F. Zerbi, A. Antonelli, P. Conconi, G. Cutispoto, S. Covino, F. D'Alessio, A. de Ugarte Postigo, E. Molinari, L. Nicastro, G. Tosti, F. Vitali, R. Mazzoleni, G. Sciuto, M. Stefanon, B. Jordan, L. Burderi, S. Campana, J. Danziger, A. di Paola, A. Fernandez-Soto, F. Fiore, G. Ghisellini, P. Goldoni, G. L. Israel, D. Lorenzetti, B. McBreen, N. Masetti, S. Messina, E. Meurs, A. Monfardini, E. Palazzi, J. Paul, E. Pian, M. Rodono, L. Stella, G. Tagliaferri, V. Testa, and S. D. Vergani. The last born at La Silla: REM, The Rapid Eye Mount. *The Messenger*, 113:40–44, September 2003.

E. Clausen-Brown, T. Savolainen, A. B. Pushkarev, Y. Y. Kovalev, and M. L. Lister. AGN jet physics and apparent opening angles. *ArXiv e-prints*, January 2013.

M. H. Cohen, M. L. Lister, D. C. Homan, M. Kadler, K. I. Kellermann, Y. Y. Kovalev, and R. C. Vermeulen. Relativistic Beaming and the Intrinsic Properties of Extragalactic Radio Jets. *Astrophys. Journal*, 658:232–244, March 2007. doi: 10.1086/511063.

M. Colless, G. Dalton, S. Maddox, W. Sutherland, P. Norberg, S. Cole, J. Bland-Hawthorn, T. Bridges, R. Cannon, C. Collins, W. Couch, N. Cross, K. Deeley, R. De Propris, S. P. Driver, G. Efstathiou, R. S. Ellis, C. S. Frenk, K. Glazebrook, C. Jackson, O. Lahav, I. Lewis, S. Lumsden, D. Madgwick, J. A. Peacock, B. A. Peterson, I. Price, M. Seaborne, and K. Taylor. The 2dF Galaxy Redshift Survey: spectra and redshifts. *Mon. Not. R. Atron. Soc.*, 328:1039–1063, December 2001. doi: 10.1046/j.1365-8711.2001.04902.x.

K. Cook and M. T. Carini. Exploring Blazar Jet Dynamics with Optical and Gamma Ray Cross-Correlations Using the Fermi Gamma Ray Space Telescope Public Data. In *American Astronomical Society Meeting Abstracts #215*, volume 42 of *Bulletin of the American Astronomical Society*, page 434.07, January 2010.

P. A. Curran, P. A. Evans, M. Still, C. Brocksopp, and C. Done. Swift Pointed Observations of XTE J1752-223. *The Astronomer's Telegram*, 2424:1, February 2010.

A. G. de Bruyn and J. Dennett-Thorpe. The Microarcsecond Quasar J1819+3845: Polarization Observations and Detailed Lightcurve Analysis. *Astrophys. and Space Science*, 278: 139–142, October 2001. doi: 10.1023/A:1013134123695.

A. T. Deller, S. J. Tingay, M. Bailes, and C. West. DiFX: A Software Correlator for Very Long Baseline Interferometry Using Multiprocessor Computing Environments. *Pub. Astron. Soc. Pacific*, 119:318–336, March 2007. doi: 10.1086/513572.

W. A. Dent. Quasi-Stellar Sources: Variation in the Radio Emission of 3C 273. *Science*, 148: 1458–1460, June 1965. doi: 10.1126/science.148.3676.1458.

S. di Serego-Alighieri, I. J. Danziger, R. Morganti, and C. N. Tadhunter. New Identifications and Redshifts for Southern 2-JANSKY Radio Sources. *Mon. Not. R. Atron. Soc.*, 269:998, August 1994.

D. Donato. Fermi LAT detection of a GeV flare from blazar PKS 1424-41. *The Astronomer's Telegram*, 2583:1, April 2010.

A. Eckart and R. Genzel. Stellar proper motions in the central 0.1 PC of the Galaxy. *Mon. Not. R. Atron. Soc.*, 284:576–598, January 1997.

R. A. Edelson and J. H. Krolik. The discrete correlation function - A new method for analyzing unevenly sampled variability data. *Astrophys. Journal*, 333:646–659, October 1988. doi: 10.1086/166773.

M. Elvis, B. J. Wilkes, J. C. McDowell, R. F. Green, J. Bechtold, S. P. Willner, M. S. Oey, E. Polomski, and R. Cutri. Atlas of quasar energy distributions. *Astrophys. Journal Sup. Series*, 95:1–68, November 1994. doi: 10.1086/192093.

C. E. Fichtel, D. L. Bertsch, J. Chiang, B. L. Dingus, J. A. Esposito, J. M. Fierro, R. C. Hartman, S. D. Hunter, G. Kanbach, D. A. Kniffen, P. W. Kwok, Y. C. Lin, J. R. Mattox, H. A. Mayer-Hasselwander, L. McDonald, P. F. Michelson, C. von Montigny, P. L. Nolan, K. Pinkau, H.-D. Radecke, H. Rothermel, P. Sreekumar, M. Sommer, E. J. Schneid, D. J. Thompson, and T. Willis. The first energetic gamma-ray experiment telescope (EGRET) source catalog. *Astrophys. Journal Sup. Series*, 94:551–581, October 1994. doi: 10.1086/192082.

E. L. Fitzpatrick. Correcting for the Effects of Interstellar Extinction. *Pub. Astron. Soc. Pacific*, 111:63–75, January 1999. doi: 10.1086/316293.

G. Fossati, L. Maraschi, A. Celotti, A. Comastri, and G. Ghisellini. A unifying view of the spectral energy distributions of blazars. *Mon. Not. R. Atron. Soc.*, 299:433–448, September 1998. doi: 10.1046/j.1365-8711.1998.01828.x.

A. Gal-Yam, P. Nugent, Y. Cao, D. Levitan, G. Hallinan, G. Kyne, J. Silverman, K. Clubb, A. Miller, O. Fox, N. Suzuki, and R. Quimby. PTF SN discovery report, October 9, 2012. *The Astronomer's Telegram*, 4470:1, October 2012.

K. Gebhardt and J. Thomas. The Black Hole Mass, Stellar Mass-to-Light Ratio, and Dark Halo in M87. *Astrophys. Journal*, 700:1690–1701, August 2009. doi: 10.1088/0004-637X/700/2/1690.

A. M. Ghez, M. Morris, E. E. Becklin, A. Tanner, and T. Kremenek. The accelerations of stars orbiting the Milky Way's central black hole. *Nature*, 407:349–351, September 2000. doi: 10.1038/35030032.

G. Ghisellini, G. Tagliaferri, L. Foschini, G. Ghirlanda, F. Tavecchio, R. Della Ceca, F. Haardt, M. Volonteri, and N. Gehrels. High-redshift Fermi blazars. *Mon. Not. R. Atron. Soc.*, 411:901–914, February 2011. doi: 10.1111/j.1365-2966.2010.17723.x.

J. L. Greenstein. Red-Shift of the Unusual Radio Source: 3C 48. *Nature*, 197:1041–1042, March 1963. doi: 10.1038/1971041a0.

J. L. Greenstein and M. Schmidt. The Quasi-Stellar Radio Sources 3c 48 and 3c 273. *Astrophys. Journal*, 140:1, July 1964. doi: 10.1086/147889.

E. W. Greisen. Recent Developments in Experimental AIPS. In R. Albrecht, R. N. Hook, and H. A. Bushouse, editors, *Astronomical Data Analysis Software and Systems VII*, volume 145 of *Astronomical Society of the Pacific Conference Series*, pages 204–+, 1998.

S. Gulyaev, T. Natusch, S. Weston, N. Palmer, and D. Collett. Warkworth 12-m VLBI Station: WARK12M. *ArXiv e-prints 1103.2830*, March 2011.

R. Güsten, L. Å. Nyman, P. Schilke, K. Menten, C. Cesarsky, and R. Booth. The Atacama Pathfinder EXperiment (APEX) - a new submillimeter facility for southern skies -. *Astron. and Astrophys.*, 454:L13–L16, August 2006. doi: 10.1051/0004-6361:20065420.

R. C. Hartman, D. L. Bertsch, C. E. Fichtel, S. D. Hunter, G. Kanbach, D. A. Kniffen, P. W. Kwok, Y. C. Lin, J. R. Mattox, H. A. Mayer-Hasselwander, P. F. Michelson, C. von Montigny, H. I. Nel, P. L. Nolan, K. Pinkau, H. Rothermel, E. Schneid, M. Sommer, P. Sreekumar, and D. J. Thompson. Detection of high-energy gamma radiation from quasar 3C 279 by the EGRET telescope on the Compton Gamma Ray Observatory. *Astrophys. Journal Letters*, 385:L1–L4, January 1992. doi: 10.1086/186263.

R. C. Hartman, D. L. Bertsch, B. L. Dingus, C. E. Fichtel, S. D. Hunter, G. Kanbach, D. A. Kniffen, Y. C. Lin, J. R. Mattox, H. A. Mayer-Hasselwander, P. F. Michelson, C. von Montigny, P. L. Nolan, B. G. Piner, E. Schneid, P. Sreekumar, and D. J. Thompson. EGRET detection of high-energy gamma radiation from the OVV quasar 3C 454.3. *Astrophys. Journal Letters*, 407:L41–L44, April 1993. doi: 10.1086/186801.

R. C. Hartman, D. L. Bertsch, S. D. Bloom, A. W. Chen, P. Deines-Jones, J. A. Esposito, C. E. Fichtel, D. P. Friedlander, S. D. Hunter, L. M. McDonald, P. Sreekumar, D. J. Thompson, B. B. Jones, Y. C. Lin, P. F. Michelson, P. L. Nolan, W. F. Tompkins, G. Kanbach, H. A. Mayer-Hasselwander, A. Mücke, M. Pohl, O. Reimer, D. A. Kniffen, E. J. Schneid, C. von Montigny, R. Mukherjee, and B. L. Dingus. The Third EGRET Catalog of High-Energy Gamma-Ray Sources. *Astrophys. Journal Sup. Series*, 123:79–202, July 1999. doi: 10.1086/313231.

M. Hauser, B. Behera, H. Hagen, and S. Wagner. Detection of an optical flare from PKS 2052-474. *The Astronomer's Telegram*, 2158:1, August 2009.

C. Hazard, M. B. Mackey, and A. J. Shimmins. Investigation of the Radio Source 3C 273 By The Method of Lunar Occultations. *Nature*, 197:1037–1039, March 1963. doi: 10.1038/1971037a0.

S. E. Healey, R. W. Romani, G. Cotter, P. F. Michelson, E. F. Schlafly, A. C. S. Readhead, P. Giommi, S. Chaty, I. A. Grenier, and L. C. Weintraub. CGRaBS: An All-Sky Survey of Gamma-Ray Blazar Candidates. *Astrophys. Journal Sup. Series*, 175:97–104, March 2008. doi: 10.1086/523302.

D. S. Heeschen. Flickering of extragalactic radio sources. *Astron. Journal*, 89:1111–1123, August 1984. doi: 10.1086/113608.

P. C. Hewett, C. B. Foltz, and F. H. Chaffee. The large bright quasar survey. 6: Quasar catalog and survey parameters. *Astron. Journal*, 109:1498–1521, April 1995. doi: 10.1086/117380.

C. Hoffmeister. 354 neue Veränderliche. *Astronomische Nachrichten*, 236:233–+, September 1929.

P. J. Humphrey, D. A. Buote, F. Brighenti, K. Gebhardt, and W. G. Mathews. Weighing the Quiescent Central Black Hole in an Elliptical Galaxy with X-Ray-Emitting Gas. *Astrophys. Journal*, 683:161–171, August 2008. doi: 10.1086/589709.

R. W. Hunstead. Four variable radio sources at 408 MHz. , 12:193–200, December 1972.

S. D. Hunter, D. L. Bertsch, B. L. Dingus, C. E. Fichtel, R. C. Hartman, G. Kanbach, D. A. Kniffen, P. W. Kwok, Y. C. Lin, J. R. Mattox, H. A. Mayer-Hasselwander, P. F. Michelson, P. Moller, C. von Montigny, P. L. Nolan, K. Pinkau, H.-D. Radecke, H. Rothermel, P. Shaver, E. Schneid, M. Sommer, P. Sreekumar, and D. J. Thompson. Detection of high-energy gamma rays from quasar PKS 0528 + 134 by EGRET on the Compton Gamma Ray Observatory. *Astrophys. Journal*, 409:134–138, May 1993. doi: 10.1086/172648.

S. D. Hunter, S. W. Digel, E. J. de Geus, and G. Kanbach. Gamma-ray observations of Ophiuchus with EGRET: The diffuse emission and point sources. *Astrophys. Journal*, 436: 216–228, November 1994. doi: 10.1086/174894.

C. D. Impey and S. Tapia. New blazars discovered by polarimetry. *Astrophys. Journal*, 333: 666–672, October 1988. doi: 10.1086/166775.

K. G. Jansky. Directional Studies of Atmospherics at High Frequencies. *Proceedings of the Institute of Radio Engineering*, 20:1920+, 1932. doi: 10.1109/JRPROC.1932.227477. URL `http://dx.doi.org/10.1109/JRPROC.1932.227477`.

K. G. Jansky. *1933, Electrical Disturbances Apparently of Extraterrestrial Origin*, page 23. 1933.

S. G. Jorstad, A. P. Marscher, J. R. Mattox, M. F. Aller, H. D. Aller, A. E. Wehrle, and S. D. Bloom. Multiepoch Very Long Baseline Array Observations of EGRET-detected Quasars and BL Lacertae Objects: Connection between Superluminal Ejections and Gamma-Ray Flares in Blazars. *Astrophys. Journal*, 556:738–748, August 2001a. doi: 10.1086/321605.

S. G. Jorstad, A. P. Marscher, J. R. Mattox, A. E. Wehrle, S. D. Bloom, and A. V. Yurchenko. Multiepoch Very Long Baseline Array Observations of EGRET-detected Quasars and BL Lacertae Objects: Superluminal Motion of Gamma-Ray Bright Blazars. *Astrophys. Journal Sup. Series*, 134:181–240, June 2001b. doi: 10.1086/320858.

J. Kataoka, T. Takahashi, S. J. Wagner, N. Iyomoto, P. G. Edwards, K. Hayashida, S. Inoue, G. M. Madejski, F. Takahara, C. Tanihata, and N. Kawai. Characteristic X-Ray Variability of TeV Blazars: Probing the Link between the Jet and the Central Engine. *Astrophys. Journal*, 560:659–674, October 2001. doi: 10.1086/322442.

L. Kedziora-Chudczer, D. L. Jauncey, M. A. Wieringa, A. K. Tzioumis, and H. E. Bignall. Examples of extreme intraday variability. *Astrophys. and Space Science*, 278:113–117, October 2001. doi: 10.1023/A:1013173805039.

K. I. Kellermann and F. N. Owen. *Radio galaxies and quasars*, pages 563–602. 1988.

K. I. Kellermann and I. I. K. Pauliny-Toth. The Spectra of Opaque Radio Sources. *Astrophys. Journal Letters*, 155:L71, February 1969. doi: 10.1086/180305.

K. I. Kellermann, M. L. Lister, D. C. Homan, R. C. Vermeulen, M. H. Cohen, E. Ros, M. Kadler, J. A. Zensus, and Y. Y. Kovalev. Sub-Milliarcsecond Imaging of Quasars and Active Galactic Nuclei. III. Kinematics of Parsec-scale Radio Jets. *Astrophys. Journal*, 609:539–563, July 2004. doi: 10.1086/421289.

S. Komossa, W. Voges, D. Xu, S. Mathur, H.-M. Adorf, G. Lemson, W. J. Duschl, and D. Grupe. Radio-loud Narrow-Line Type 1 Quasars. *Astron. Journal*, 132:531–545, August 2006. doi: 10.1086/505043.

Y. Y. Kovalev, K. I. Kellermann, M. L. Lister, D. C. Homan, R. C. Vermeulen, M. H. Cohen, E. Ros, M. Kadler, A. P. Lobanov, J. A. Zensus, N. S. Kardashev, L. I. Gurvits, M. F. Aller, and H. D. Aller. Sub-Milliarcsecond Imaging of Quasars and Active Galactic Nuclei. IV. Fine-Scale Structure. *Astron. Journal*, 130:2473–2505, December 2005. doi: 10.1086/497430.

Y. Y. Kovalev, H. D. Aller, M. F. Aller, D. C. Homan, M. Kadler, K. I. Kellermann, Y. A. Kovalev, M. L. Lister, M. J. McCormick, A. B. Pushkarev, E. Ros, and J. A. Zensus. The Relation Between AGN Gamma-Ray Emission and Parsec-Scale Radio Jets. *Astrophys. Journal Letters*, 696:L17–L21, May 2009. doi: 10.1088/0004-637X/696/1/L17.

A. Lähteenmäki and E. Valtaoja. Total Flux Density Variations in Extragalactic Radio Sources. III. Doppler Boosting Factors, Lorentz Factors, and Viewing Angles for Active Galactic Nuclei. *Astrophys. Journal*, 521:493–501, August 1999. doi: 10.1086/307587.

A. Lähteenmäki and E. Valtaoja. Testing of Inverse Compton Models for Active Galactic Nuclei with Gamma-Ray and Radio Observations. *Astrophys. Journal*, 590:95–108, June 2003. doi: 10.1086/374883.

H. Landt, P. Padovani, P. Giommi, M. Perri, and C. C. Cheung. A Search for Synchrotron X-Ray Emission in Radio Quasars. *Astrophys. Journal*, 676:87–100, March 2008. doi: 10.1086/527531.

S. Larsson. Statistical Analysis of Multiwavelength Light curves. *ArXiv e-prints*, July 2012.

J. D. Linford, G. B. Taylor, R. W. Romani, S. E. Healey, J. F. Helmboldt, A. C. S. Readhead, R. Reeves, J. L. Richards, and G. Cotter. Characteristics of gamma-ray loud blazars in the vlba imaging and polarimetry survey. *The Astrophysical Journal*, 726(1):16, 2011. URL `http://stacks.iop.org/0004-637X/726/i=1/a=16`.

J. D. Linford, G. B. Taylor, R. W. Romani, J. F. Helmboldt, A. C. S. Readhead, R. Reeves, and J. L. Richards. Parsec-Scale Radio Properties of Gamma-Ray Emitting Blazars. *ArXiv e-prints*, May 2012.

M. L. Lister, S. J. Tingay, D. W. Murphy, B. G. Piner, D. L. Jones, and R. A. Preston. The Pearson-Readhead Survey of Compact Extragalactic Radio Sources from Space. I. The Images. *Astrophys. Journal*, 554:948–963, June 2001. doi: 10.1086/321429.

M. L. Lister, D. C. Homan, M. Kadler, K. I. Kellermann, Y. Y. Kovalev, E. Ros, T. Savolainen, and J. A. Zensus. A Connection Between Apparent VLBA Jet Speeds and Initial Active Galactic Nucleus Detections Made by the Fermi Gamma-Ray Observatory. *Astrophys. Journal Letters*, 696:L22–L26, May 2009. doi: 10.1088/0004-637X/696/1/L22.

F. Longo, G. Iafrate, E. Hays, and M. Marelli. Fermi LAT detection of increasing gamma-ray activity of blazar PKS 1424-418. *The Astronomer's Telegram*, 2104:1, June 2009.

J. Lovell. Difwrap: A Graphical User Interface for Error Analysis in Difmap. In H. Hirabayashi, P. G. Edwards, and D. W. Murphy, editors, *Astrophysical Phenomena Revealed by Space VLBI*, pages 301–304, April 2000.

J. E. J. Lovell, D. L. Jauncey, H. E. Bignall, L. Kedziora-Chudczer, J.-P. Macquart, B. J. Rickett, and A. K. Tzioumis. First Results from MASIV: The Microarcsecond Scintillation-induced Variability Survey. *Astron. Journal*, 126:1699–1706, October 2003. doi: 10.1086/378053.

J. E. J. Lovell, B. J. Rickett, J.-P. Macquart, D. L. Jauncey, H. E. Bignall, L. Kedziora-Chudczer, R. Ojha, T. Pursimo, M. Dutka, C. Senkbeil, and S. Shabala. The Micro-Arcsecond Scintillation-Induced Variability (MASIV) Survey. II. The First Four Epochs. *Astrophys. Journal*, 689:108–126, December 2008. doi: 10.1086/592485.

J.-P. Macquart and A. G. de Bruyn. Emergence and disappearance of microarcsecond structure in the scintillating quasar J1819+3845. *Mon. Not. R. Atron. Soc.*, 380:L20–L24, September 2007. doi: 10.1111/j.1745-3933.2007.00341.x.

L. Maraschi, G. Ghisellini, and A. Celotti. A jet model for the gamma-ray emitting blazar 3C 279. *Astrophys. Journal Letters*, 397:L5–L9, September 1992. doi: 10.1086/186531.

H. L. Marshall, D. A. Schwartz, J. E. J. Lovell, D. W. Murphy, D. M. Worrall, M. Birkinshaw, J. M. Gelbord, E. S. Perlman, and D. L. Jauncey. A Chandra Survey of Quasar Jets: First Results. *Astrophys. Journal Sup. Series*, 156:13–33, January 2005. doi: 10.1086/425578.

J. R. Mattox, D. L. Bertsch, J. Chiang, B. L. Dingus, S. W. Digel, J. A. Esposito, J. M. Fierro, R. C. Hartman, S. D. Hunter, G. Kanbach, D. A. Kniffen, Y. C. Lin, D. J. Macomb, H. A. Mayer-Hasselwander, P. F. Michelson, C. von Montigny, R. Mukherjee, P. L. Nolan, P. V. Ramanamurthy, E. Schneid, P. Sreekumar, D. J. Thompson, and T. D. Willis. The Likelihood Analysis of EGRET Data. *Astrophys. Journal*, 461:396, April 1996. doi: 10.1086/177068.

P. M. McCulloch, S. P. Ellingsen, D. L. Jauncey, S. J. B. Carter, G. Cimò, J. E. J. Lovell, and R. G. Dodson. COSMIC: Microarcsecond Resolution with a 30 Meter Radio Telescope. *Astron. Journal*, 129:2034–2040, April 2005. doi: 10.1086/428374.

J. S. Miller, H. B. French, and S. A. Hawley. Optical spectra of BL Lacertae objects. In A. M. Wolfe, editor, *BL Lac Objects*, pages 176–187, 1978.

R. Minkowski. A New Distant Cluster of Galaxies. *Astrophys. Journal*, 132:908–910, November 1960. doi: 10.1086/146994.

M. Miyoshi, J. Moran, J. Herrnstein, L. Greenhill, N. Nakai, P. Diamond, and M. Inoue. Evidence for a black hole from high rotation velocities in a sub-parsec region of NGC4258. *Nature*, 373:127–129, January 1995. doi: 10.1038/373127a0.

R. Mukherjee, D. L. Bertsch, S. D. Bloom, B. L. Dingus, J. A. Esposito, C. E. Fichtel, R. C. Hartman, S. D. Hunter, G. Kanbach, D. A. Kniffen, Y. C. Lin, H. A. Mayer-Hasselwander, L. M. McDonald, P. F. Michelson, C. von Montigny, A. Muecke, P. L. Nolan, M. Pohl, O. Reimer, E. Schneid, P. Sreekumar, and D. J. Thompson. EGRET Observations of High-energy Gamma-Ray Emission from Blazars: an Update. *Astrophys. Journal*, 490: 116, November 1997. doi: 10.1086/304851.

C. Müller, M. Kadler, R. Ojha, J. Wilms, M. Böck, P. G. Edwards, C. M. Fromm, H. Hase, S. Horiuchi, U. Katz, J. E. J. Lovell, C. Plötz, T. Pursimo, S. Richers, E. Ros, R. E. Rothschild, G. B. Taylor, S. J. Tingay, and J. A. Zensus. Dual-frequency VLBI study of Centaurus A on sub-parsec scales. The highest-resolution view of an extragalactic jet. *Astron. and Astrophys.*, 530:L11+, June 2011. doi: 10.1051/0004-6361/201116605.

R. Nesci, G. Tosti, T. Pursimo, R. Ojha, and M. Kadler. Near-infrared and gamma-ray monitoring of TANAMI gamma-ray bright sources. *Astron. and Astrophys.*, 555:A2, July 2013. doi: 10.1051/0004-6361/201321094.

P. L. Nolan, A. A. Abdo, M. Ackermann, M. Ajello, A. Allafort, E. Antolini, W. B. Atwood, M. Axelsson, L. Baldini, J. Ballet, G. Barbiellini, D. Bastieri, K. Bechtol, A. Belfiore, R. Bellazzini, B. Berenji, G. F. Bignami, R. D. Blandford, E. D. Bloom, E. Bonamente, J. Bonnell, A. W. Borgland, E. Bottacini, A. Bouvier, T. J. Brandt, J. Bregeon, M. Brigida, P. Bruel, R. Buehler, T. H. Burnett, S. Buson, G. A. Caliandro, R. A. Cameron, R. Campana, B. Caadas, A. Cannon, P. A. Caraveo, J. M. Casandjian, E. Cavazzuti, M. Ceccanti, C. Cecchi, . elik, E. Charles, A. Chekhtman, C. C. Cheung, J. Chiang, R. Chipaux, S. Ciprini, R. Claus, J. Cohen-Tanugi, L. R. Cominsky, J. Conrad, R. Corbet, S. Cutini, F. D'Ammando, D. S. Davis, A. de Angelis, M. E. DeCesar, M. DeKlotz, A. De Luca, P. R. den Hartog, F. de Palma, C. D. Dermer, S. W. Digel, E. do Couto e Silva, P. S. Drell, A. Drlica-Wagner, R. Dubois, D. Dumora, T. Enoto, L. Escande, D. Fabiani, L. Falletti, C. Favuzzi, S. J. Fegan, E. C. Ferrara, W. B. Focke, P. Fortin, M. Frailis, Y. Fukazawa, S. Funk, P. Fusco, F. Gargano, D. Gasparrini, N. Gehrels, S. Germani, B. Giebels, N. Giglietto, P. Giommi, F. Giordano, M. Giroletti, T. Glanzman, G. Godfrey, I. A. Grenier, M.-H. Grondin, J. E. Grove, L. Guillemot, S. Guiriec, M. Gustafsson, D. Hadasch, Y. Hanabata, A. K. Harding, M. Hayashida, E. Hays, A. B. Hill, D. Horan, X. Hou, R. E. Hughes, G. Iafrate, R. Itoh, G. Jhannesson, R. P. Johnson, T. E. Johnson, A. S. Johnson, T. J. Johnson, T. Kamae, H. Katagiri, J. Kataoka, J. Katsuta, N. Kawai, M. Kerr, J. Kndlseder, D. Kocevski, M. Kuss, J. Lande, D. Landriu, L. Latronico, M. Lemoine-Goumard, A. M. Lionetto, M. Llena Garde, F. Longo, F. Loparco, B. Lott, M. N. Lovellette, P. Lubrano, G. M. Madejski, M. Marelli, E. Massaro, M. N. Mazziotta, W. McConville, J. E. McEnery, J. Mehault, P. F. Michelson, M. Minuti, W. Mitthumsiri, T. Mizuno, A. A. Moiseev, M. Mongelli, C. Monte, M. E. Monzani, A. Morselli, I. V. Moskalenko, S. Murgia, T. Nakamori, M. Naumann-Godo, J. P. Norris, E. Nuss, T. Nymark, M. Ohno, T. Ohsugi, A. Okumura, N. Omodei, E. Orlando, J. F. Ormes, M. Ozaki, D. Paneque, J. H. Panetta, D. Parent, J. S. Perkins, M. Pesce-Rollins, M. Pierbattista, M. Pinchera, F. Piron, G. Pivato, T. A. Porter, J. L. Racusin, S. Rain, R. Rando, M. Razzano, S. Razzaque, A. Reimer, O. Reimer, T. Reposeur, S. Ritz, L. S. Rochester, R. W. Romani, M. Roth, R. Rousseau, F. Ryde, H. F.-W. Sadrozinski, D. Salvetti, D. A. Sanchez, P. M. Saz Parkinson, C. Sbarra, J. D. Scargle, T. L. Schalk, C. Sgr, M. S. Shaw, C. Shrader, E. J. Siskind, D. A. Smith, G. Spandre, P. Spinelli, T. E. Stephens, M. S. Strickman, D. J.

Suson, H. Tajima, H. Takahashi, T. Takahashi, T. Tanaka, J. G. Thayer, J. B. Thayer, D. J. Thompson, L. Tibaldo, O. Tibolla, F. Tinebra, M. Tinivella, D. F. Torres, G. Tosti, E. Troja, Y. Uchiyama, J. Vandenbroucke, A. Van Etten, B. Van Klaveren, V. Vasileiou, G. Vianello, V. Vitale, A. P. Waite, E. Wallace, P. Wang, M. Werner, B. L. Winer, D. L. Wood, K. S. Wood, M. Wood, Z. Yang, and S. Zimmer. Fermi large area telescope second source catalog. *The Astrophysical Journal Supplement Series*, 199(2):31, 2012. URL `http://stacks.iop.org/0067-0049/199/i=2/a=31`.

P. L. Nolan, A. A. Abdo, M. Ackermann, M. Ajello, A. Allafort, E. Antolini, W. B. Atwood, M. Axelsson, L. Baldini, J. Ballet, and et al. Fermi Large Area Telescope Second Source Catalog. *Astrophys. Journal Sup. Series*, 199:31, April 2012. doi: 10.1088/0067-0049/199/2/31.

R. Ojha, A. L. Fey, K. J. Johnston, D. L. Jauncey, J. E. Reynolds, A. K. Tzioumis, J. F. H. Quick, G. D. Nicolson, S. P. Ellingsen, R. G. Dodson, and P. M. McCulloch. VLBI Observations of Southern Hemisphere ICRF Sources. I. *Astron. Journal*, 127:3609–3621, June 2004. doi: 10.1086/421001.

R. Ojha, M. Kadler, M. Böck, R. Booth, M. S. Dutka, P. G. Edwards, A. L. Fey, L. Fuhrmann, R. A. Gaume, H. Hase, S. Horiuchi, D. L. Jauncey, K. J. Johnston, U. Katz, M. Lister, J. E. J. Lovell, C. Müller, C. Plötz, J. F. H. Quick, E. Ros, G. B. Taylor, D. J. Thompson, S. J. Tingay, G. Tosti, A. K. Tzioumis, J. Wilms, and J. A. Zensus. TANAMI: tracking active galactic nuclei with austral milliarcsecond interferometry . I. First-epoch 8.4 GHz images. *Astron. and Astrophys.*, 519:A45, September 2010. doi: 10.1051/0004-6361/200912724.

S. P. O'Sullivan and D. C. Gabuzda. Magnetic field strength and spectral distribution of six parsec-scale active galactic nuclei jets. *Mon. Not. R. Atron. Soc.*, 400:26–42, November 2009. doi: 10.1111/j.1365-2966.2009.15428.x.

P. Padovani and P. Giommi. The connection between x-ray- and radio-selected BL Lacertae objects. *Astrophys. Journal*, 444:567–581, May 1995. doi: 10.1086/175631.

J.A. Peacock. *Cosmological Physics*. Cambridge Astrophysics Series. Cambridge University Press, 1999. ISBN 9780521422703. URL `http://books.google.com.au/books?id=t8O-yylU0j0C`.

T. J. Pearson and A. C. S. Readhead. Image Formation by Self-Calibration in Radio Astronomy. *Ann. Rev. Astron. and Astrophys.*, 22:97–130, 1984. doi: 10.1146/annurev.aa.22.090184.000525.

B. M. Peterson. Reverberation mapping of active galactic nuclei. *Pub. Astron. Soc. Pacific*, 105:247–268, March 1993. doi: 10.1086/133140.

C. Phillips, T. Tzioumis, S. Tingay, J. Stevens, J. Lovell, S. Amy, C. West, and R. Dodson. LBADR: The LBA Data Recorder. In *8th International e-VLBI Workshop*, 2009.

B. G. Piner, M. Mahmud, A. L. Fey, and K. Gospodinova. Relativistic Jets in the Radio Reference Frame Image Database. I. Apparent Speeds from the First 5 Years of Data. *Astron. Journal*, 133:2357–2388, May 2007. doi: 10.1086/514812.

R. A. Preston, D. L. Jauncey, D. L. Meier, A. K. Tzioumis, J. Ables, R. Batchelor, J. Faulkner, J. Gates, B. Greene, P. A. Hamilton, B. R. Harvey, R. F. Haynes, B. Johnson, K. Lambeck, A. P. Louie, P. McCulloch, G. Moorey, D. D. Morabito, G. D. Nicolson, A. E. Niell, J. G. Robertson, G. R. Royle, L. Skjerve, M. A. Slade, O. B. Slee, A. Stolz, A. Watkinson, A. E. Wehrle, and A. E. Wright. The Southern Hemisphere VLBI experiment. *Astron. Journal*, 98:1–26, July 1989. doi: 10.1086/115122.

B. Punsly, L. F. Rodríguez, S. J. Tingay, and S. A. Cellone. PKS 1622-253: A Weakly Accreting, Powerful Gamma-Ray Source. *Astrophys. Journal Letters*, 633:L93–L96, November 2005. doi: 10.1086/498307.

A. B. Pushkarev, Y. Y. Kovalev, M. L. Lister, and T. Savolainen. Jet opening angles and gamma-ray brightness of AGN. *Astron. and Astrophys.*, 507:L33–L36, November 2009. doi: 10.1051/0004-6361/200913422.

A. B. Pushkarev, Y. Y. Kovalev, and M. L. Lister. Radio/Gamma-ray Time Delay in the Parsec-scale Cores of Active Galactic Nuclei. *Astrophys. Journal Letters*, 722:L7–L11, October 2010. doi: 10.1088/2041-8205/722/1/L7.

A. C. S. Readhead. Equipartition brightness temperature and the inverse Compton catastrophe. *Astrophys. Journal*, 426:51–59, May 1994. doi: 10.1086/174038.

A. C. S. Readhead, R. C. Walker, T. J. Pearson, and M. H. Cohen. Mapping radio sources with uncalibrated visibility data. *Nature*, 285:137–140, May 1980. doi: 10.1038/285137a0.

G. Reber. Cosmic Static. *Astrophys. Journal*, 100:279, November 1944. doi: 10.1086/144668.

M. J. Rees. Black Hole Models for Active Galactic Nuclei. *Ann. Rev. Astron. and Astrophys.*, 22:471–506, 1984. doi: 10.1146/annurev.aa.22.090184.002351.

W. Reich, H. Steppe, R. Schlickeiser, P. Reich, M. Pohl, H. P. Reuter, G. Kanbach, and V. Schonfelder. The Radio State of Extragalactic Gamma-Ray Sources Detected by CGRO. *Astron. and Astrophys.*, 273:65, June 1993.

L. Reyes, C. Fermi LAT detection of a GeV flare from blazar PKS 1622-253. *The Astronomer's Telegram*, 2231:1, October 2009.

J. E. Reynolds. A revised flux scale for the at compact array. ATNF Memo AT/39.3/040, 1994.

B. Rickett. The Role of Interstellar Scintillation in Intraday Variations at Centimetre Wavelengths. , 19:100–105, 2002. doi: 10.1071/AS01120.

B. J. Rickett. Refractive interstellar scintillation of radio sources. *Astrophys. Journal*, 307: 564–574, August 1986. doi: 10.1086/164444.

L. Rudnick and T. W. Jones. Compact radio sources - The dependence of variability and polarization on spectral shape. *Astrophys. Journal*, 255:39–47, April 1982. doi: 10.1086/159800.

G. B. Rybicki and A. P. Lightman. *Radiative processes in astrophysics*. Wiley-Interscience, 1979.

T. Savolainen, D. C. Homan, T. Hovatta, M. Kadler, Y. Y. Kovalev, M. L. Lister, E. Ros, and J. A. Zensus. Relativistic beaming and gamma-ray brightness of blazars. *Astron. and Astrophys.*, 512:A24, March 2010. doi: 10.1051/0004-6361/200913740.

W. Schlüter and D. Behrend. The International VLBI Service for Geodesy and Astrometry (IVS): current capabilities and future prospects. *Journal of Geodesy*, 81:379–387, June 2007a. doi: 10.1007/s00190-006-0131-z.

W. Schlüter and D. Behrend. The International VLBI Service for Geodesy and Astrometry (IVS): current capabilities and future prospects. *Journal of Geodesy*, 81:379–387, June 2007b. doi: 10.1007/s00190-006-0131-z.

M. Schmidt. 3C 273 : A Star-Like Object with Large Red-Shift. *Nature*, 197:1040–+, March 1963. doi: 10.1038/1971040a0.

M. Schmidt and R. F. Green. Quasar evolution derived from the Palomar bright quasar survey and other complete quasar surveys. *Astrophys. Journal*, 269:352–374, June 1983. doi: 10.1086/161048.

J. L. Schmitt. BL Lac identified as a Radio Source. *Nature*, 218:663, May 1968. doi: 10.1038/218663a0.

G. A. Seielstad, T. J. Pearson, and A. C. S. Readhead. 10.8-GHz flux density variations among a complete sample of sources from the NRAO-Bonn 84 survey. *Pub. Astron. Soc. Pacific*, 95:842–872, November 1983. doi: 10.1086/131261.

C. E. Senkbeil, S. P. Ellingsen, J. E. J. Lovell, J.-P. Macquart, G. Cimò, and D. L. Jauncey. A Compact Extreme Scattering Event Cloud toward AO 0235+164. *Astrophys. Journal Letters*, 672:L95–L98, January 2008. doi: 10.1086/527300.

N. I. Shakura and R. A. Sunyaev. Black Holes in Binary Systems: Observational Appearances. In H. Bradt and R. Giacconi, editors, *X- and Gamma-Ray Astronomy*, volume 55 of *IAU Symposium*, page 155, 1973.

M. C. Shepherd, T. J. Pearson, and G. B. Taylor. DIFMAP: an interactive program for synthesis imaging. In B. J. Butler & D. O. Muhleman, editor, *Bulletin of the American Astronomical Society*, volume 27 of *Bulletin of the American Astronomical Society*, pages 903–+, March 1995.

G. A. Shields. Thermal continuum from acretion disks in quasars. *Nature*, 272:706–708, April 1978. doi: 10.1038/272706a0.

G. B. Sholomitskii. Fluctuations in the 32.5-cm Flux of CTA 102. , 9:516, December 1965.

F. G. Smith. An Accurate Determination of the Positions of Four Radio Stars. *Nature*, 168: 555, September 1951. doi: 10.1038/168555a0.

J. Stevens, P. G. Edwards, R. Ojha, M. Kadler, F. Hungwe, M. Dutka, S. Tingay, J. P. Macquart, A. Moin, J. Lovell, and J. Blanchard. ATCA monitoring of gamma-ray loud AGN. *ArXiv e-prints*, May 2012.

A. Szostek. Fermi LAT detection of a new GeV flare from blazar PKS 1424-41. *The Astronomer's Telegram*, 3329:1, May 2011.

A.R. Thompson, J.M. Moran, and G.W. Swenson. *Interferometry and synthesis in radio astronomy.* Wiley, 2001. ISBN 9780471254928. URL `http://books.google.com.au/books?id=AwBN5bpuEU0C`.

J. Timmer and M. Koenig. On generating power law noise. *Astron. and Astrophys.*, 300:707, August 1995.

S. J. Tingay, P. G. Edwards, M. E. Costa, J. E. J. Lovell, P. M. McCulloch, D. L. Jauncey, J. E. Reynolds, A. K. Tzioumis, V. Migenes, R. Gough, E. A. King, D. L. Jones, R. A. Preston, D. W. Murphy, D. L. Meier, T. D. van Ommen, M. St. John, D. W. Hoard, G. D. Nicolson, T.-S. Wan, and Z.-Q. Shen. VLBI Observations of Southern EGRET Identifications. I. PKS 0208-512, PKS 0521-365, and PKS 0537-441. *Astrophys. Journal*, 464:170, June 1996. doi: 10.1086/177309.

S. J. Tingay, J. E. Reynolds, A. K. Tzioumis, D. L. Jauncey, J. E. J. Lovell, R. Dodson, M. E. Costa, P. M. McCulloch, P. G. Edwards, H. Hirabayashi, D. W. Murphy, R. A. Preston, B. G. Piner, G. D. Nicolson, J. F. H. Quick, H. Kobayashi, and K. M. Shibata. VSOP Space VLBI and Geodetic VLBI Investigations of Southern Hemisphere Radio Sources. *Astrophys. Journal Sup. Series*, 141:311–335, August 2002. doi: 10.1086/340783.

M.-H. Ulrich, L. Maraschi, and C. M. Urry. Variability of Active Galactic Nuclei. *Ann. Rev. Astron. and Astrophys.*, 35:445–502, 1997. doi: 10.1146/annurev.astro.35.1.445.

C. M. Urry and P. Padovani. Unified Schemes for Radio-Loud Active Galactic Nuclei. *Pub. Astron. Soc. Pacific*, 107:803, September 1995. doi: 10.1086/133630.

P. Uttley, I. M. McHardy, and I. E. Papadakis. Measuring the broad-band power spectra of active galactic nuclei with RXTE. *Mon. Not. R. Atron. Soc.*, 332:231–250, May 2002. doi: 10.1046/j.1365-8711.2002.05298.x.

E. Valtaoja and H. Terasranta. Gamma radiation from radio shocks in AGN jets. *Astron. and Astrophys.*, 297:L13–L16, May 1995.

N. Visvanathan and B. J. Wills. Optical Polarization of 52 Radio-loud QSOS and BL Lacertae Objects. *Astron. Journal*, 116:2119–2122, November 1998. doi: 10.1086/300610.

S. J. Wagner and A. Witzel. Intraday Variability In Quasars and BL Lac Objects. *Ann. Rev. Astron. and Astrophys.*, 33:163–198, 1995. doi: 10.1146/annurev.aa.33.090195.001115.

R. C. Walker. What the VLBA Can Do For You. In J. A. Zensus, P. J. Diamond, & P. J. Napier, editor, *Very Long Baseline Interferometry and the VLBA*, volume 82 of *Astronomical Society of the Pacific Conference Series*, pages 133–+, 1995.

I. Wanders, B. M. Peterson, D. Alloin, T. R. Ayres, J. Clavel, D. M. Crenshaw, K. Horne, G. A. Kriss, J. H. Krolik, M. A. Malkan, H. Netzer, P. T. O'Brien, G. A. Reichert, P. M. Rodriguez-Pascual, W. Wamsteker, T. Alexander, K. S. J. Anderson, E. Benitez, N. G. Bochkarev, A. N. Burenkov, F.-Z. Cheng, S. J. Collier, A. Comastri, M. Dietrich, D. Dultzin-Hacyan, B. R. Espey, A. V. Filippenko, C. M. Gaskell, I. M. George, M. R. Goad, L. C. Ho, S. Kaspi, W. Kollatschny, K. T. Korista, A. Laor, G. M. MacAlpine, M. Mignoli, S. L. Morris, K. Nandra, S. Penton, R. W. Pogge, R. L. Ptak, J. M. Rodriguez-Espinoza, M. Santos-Lleo, A. I. Shapovalova, J. M. Shull, S. A. Snedden, L. S. Sparke, G. M. Stirpe, W.-H. Sun, T. J. Turner, M.-H. Ulrich, T.-G. Wang, C. Wei, W. F. Welsh, S.-J. Xue, and Z.-L. Zou. Steps toward Determination of the Size and Structure of the Broad-Line Region in Active Galactic Nuclei. XI. Intensive Monitoring of the Ultraviolet Spectrum of NGC 7469. *Astrophys. Journal Sup. Series*, 113:69–+, November 1997. doi: 10.1086/313054.

A. E. Wehrle, B. G. Piner, S. C. Unwin, A. C. Zook, W. Xu, A. P. Marscher, H. Teräsranta, and E. Valtaoja. Kinematics of the Parsec-Scale Relativistic Jet in Quasar 3C 279: 1991-1997. *Astrophys. Journal Sup. Series*, 133:297–320, April 2001. doi: 10.1086/320353.

R. J. White and B. M. Peterson. Comments on cross-correlation methodology in variability studies of active galactic nuclei. *Pub. Astron. Soc. Pacific*, 106:879–889, August 1994. doi: 10.1086/133456.

L. Wisotzki, N. Christlieb, N. Bade, V. Beckmann, T. Köhler, C. Vanelle, and D. Reimers. The Hamburg/ESO survey for bright QSOs. III. A large flux-limited sample of QSOs. *Astron. and Astrophys.*, 358:77–87, June 2000.

A. Witzel, D. S. Heeschen, C. Schalinski, and T. Krichbaum. Kurzzeit-Variabilität extragalaktischer Radioquellen. *Mitteilungen der Astronomischen Gesellschaft Hamburg*, 65: 239, 1986.

Yale-Fermi/Smarts. Smarts monitoring of lat blazars www.astro.yale.edu/smarts/glast/home.php, 2013.